# MULTI-SCALE MATERIALS

# DESIGN, FABRICATION, AND CHARACTERIZATION OF MULTI-SCALE MATERIALS FOR INTEGRATION ON LAB-ON-A-CHIP DEVICES

By CHRISTINE GABARDO, B.Eng

A Thesis Submitted to the School of Graduate Studies in Partial Fulfilment of the Requirements for the Degree Doctor of Philosophy in Biomedical Engineering

McMaster University

McMaster University DOCTOR OF PHILOSOPHY (2016) Hamilton, Ontario
(Biomedical Engineering)

TITLE: Design, Fabrication, and Characterization of Multi-Scale Materials for Integration on Lab-On-A-Chip Devices

AUTHOR: Christine Gabardo, B. Eng (McMaster University)

SUPERVISOR: Professor Leyla Soleymani

NUMBER OF PAGES: xx, 212

## LAY ABSTRACT

The incorporation of multi-scale materials, with features that span the nanoscale and microscale, has been found to be beneficial for a variety of applications, including lab-on-a-chip (LOC) devices. Rapid prototyping is advantageous over large volume manufacturing in the LOC research and development phase. However, it is challenging to create complex three-dimensional and multi-length-scale materials, critical components for optimizing LOC performance, with current rapid prototyping methods. In this thesis, we seek to develop robust, affordable, and high-speed fabrication techniques to rapidly prototype tunable, hierarchically structured, three-dimensional electrodes on the benchtop. We explore methods to structurally tune these electrodes and study the structural evolution of the electrodes with thorough characterization of the features at the nanoscale, microscale, and macroscale. We translate the electrode structural tuning into functional tuning of application-driven properties, and employ them in optimized LOC electrode devices and sensors. Finally, we combine these multi-scale electrodes with microfluidic chips to produce fully integrated LOC devices.

## ABSTRACT

Currently, molecular diagnosis is conducted by professionals in centralized laboratories, which can be time consuming, expensive, and not readily available in remote locations. This motivates the efforts to develop highly accurate, highly sensitive, and high speed lab-on-a-chip (LOC) platforms for inexpensive point-of-care (POC) diagnostics. Multi-scale materials – with tunable features from the nanometer to millimeter length-scales – have shown to enhance performance of electrodes in LOC biosensing and bioprocessing applications. The controlled fabrication of three-dimensional metallic hierarchical electrodes using standard lithographic, machining, printing, etc. techniques is complex and not suitable for rapid, dynamic, and inexpensive prototyping. The work presented herein addresses the need to develop a benchtop rapid prototyping approach to create tunable multi-scale electrodes for integration in LOC devices.

In this work, rapid benchtop fabrication is carried out through a combination of xurography, to create electrodes with specific configurations, and controlled thin film wrinkling using pre-stressed polymer substrates, to structure sputtered electrodes on the nanoscale and microscale. This method creates wrinkled structures with sufficient adhesion (no peeling) and conductance (<1 Ω/□ sheet resistance) for electrical applications. Further development of this method allows fabrication to be carried out completely on the benchtop using all-solution processing methods to deposit high quality thin films, with similar adhesion (no peeling) and conductance (<1 Ω/□ sheet resistance) as sputtered films, on the polymer substrates. Moreover, this fabrication technique is extended to create wrinkled nanoparticle films presenting sub-100 nm wavelengths and a dual degree of tunability, as the nanoparticles tune both the thickness and mechanical properties of the films. Structural tuning of the nanoscale and microscale architectures of wrinkled electrodes is studied with scanning electron microscopy (SEM), transmission electron microscopy (TEM), atomic force microscopy (AFM), and white light interferometry, and then related to functional tuning via four-point probe measurements and electrochemical measurements. As the structure is shown to determine key functional parameters, such as resistance and surface area, various electrodes structures are designed and applied to important LOC bioprocessing and sensing applications. For example, structurally optimized electrodes are applied to low voltage cell lysis and are able to lyse bacteria at only 4 V. Furthermore, the problem of integrating three-dimensional, multi-scale wrinkled electrodes into microfluidic devices is investigated. New approaches combining surface treatment and partial curing of microchannels are developed to solve these issues and create fully contained, functional electro-fluidic devices that can withstand flow rates greater than 25 mL/min and pressures of greater than 125 kPa.

Ultimately, we are able to create and integrate high quality, tunable, functional, multi-scale electrodes on the laboratory benchtop at low cost and high speed. Thus, this research enables the expedited development of LOC electrode devices that are functionally optimized through structural tuning.

## ACKNOWLEDGEMENTS

I would like to express my sincerest gratitude and appreciation to my supervisor, Dr. Leyla Soleymani for her continued guidance, patience, and support throughout this research project. Dr. Soleymani has been a remarkable academic supervisor for the past 5 years, always making time to meet and provide insightful advice, as well as going above and beyond to support her students' scientific and career goals. She has created a positive working environment that inspires innovation and scientific advancement. I would like to thank my supervisory committee members, Dr. Ponnambalam Ravi Selvaganapathy and Dr. Chang-qing Xu, for their advice and guidance throughout this research work.

I am grateful to have been among the first generation of researchers in the Soleymani Research Group. I have had the privilege to work alongside and become friends with many inspiring graduate students, including Joey Pavlovski, Stephen Woo, Amin Hosseini, Jie Yang, Barnabas Fung, and Roqibul Hasan. I would like to especially thank Aaron Kwong and Robert Chris Adams-McGavin for their hard work and devotion to our collaborative projects during their undergraduate studies.

I would like to thank my family for their constant support throughout my graduate studies. To my parents, thank you for encouraging me and supporting me to reach my goals. Thank you to my brother Phil for always being my friend and adding comedy to any situation. Lastly, thank you to my fiancé, Byron. Thank you for your patience and for always believing in me.

Finally, I wish to acknowledge the Ontario Graduate Scholarship Program, the Natural Sciences and Engineering Research Council of Canada (NSERC), and McMaster University for their financial support.

**TABLE OF CONTENTS**

## LIST OF FIGURES

# LIST OF TABLES

## LIST OF ABBREVIATIONS AND SYMBOLS

| | |
|---|---|
| AFM | Atomic force microscopy |
| APTES | (3-Aminopropyl)triethoxysilane |
| AS | After shrinking |
| Au NPs | Gold nanoparticles |
| BS | Before shrinking |
| BSA | Bovine serum albumin |
| CAD | Computer aided design |
| CE | Counter electrode |
| CFU | Colony forming unit |
| CNTs | Carbon nanotubes |
| CSE | Crumple structured electrode |
| CV | Cyclic voltammetry |
| DNA | Deoxyribonucleic acid |
| FFT | Fast Fourier transform |
| GFP | Green fluorescent protein |
| LOC | Lab-on-a-chip |

| | |
|---|---|
| Ox | Oxidation |
| PCR | Polymerase chain reaction |
| PDMS | Polydimethylsiloxane |
| PI | Propidium iodide |
| PO | Polyolefin |
| POC | Point-of-care |
| PS | Polystyrene |
| PV | Peak-to-valley |
| RE | Reference electrode |
| Red | Reduction |
| RMS | Root mean square |
| RNA | Ribonucleic acids |
| SEM | Scanning electron microscopy |
| SERS | Surface enhanced Raman spectroscopy |
| TEM | Transmission electron microscopy |
| WE | Working electrode |
| μTAS | Micro-total-analysis-systems |

## DECLARATION OF ACADEMIC ACHIEVEMENT

The majority of the written work described within the written thesis was conceived, conducted, analyzed, and written by the author of the thesis, in consultation from Dr. Leyla Soleymani, with the exception to the following:

*Chapter 2*: Yujie Zhu performed the processing of the white light interferometry data. Laura Dodge performed the contact angle measurements. Dr. Jose Moran-Mirabal contributed to the writing of the manuscript.

*Chapter 3*: Aaron Kwong aided with conducting the lysis experiments and performed the PCR experiment.

*Chapter 4*: Robert Chris Adams-McGavin aided with the development of PDMS to PS bonding techniques, as well as the flow rate and burst pressure testing of these methods.

*Chapter 5*: Robert Chris Adams-McGavin aided with electroless deposition and wrinkled electrode fabrication, as well as the AFM measurements and sheet resistance measurements. Barnabas Fung and Rashmi Rajendran assisted with the electrochemical characterization, Eric Mahoney assisted with the Raman measurements, and Jie Yang performed the TEM analysis.

*Chapter 6*: Jie Yang performed the TEM work. Nathaniel Smith assisted with the fabrication of the multilayer samples, Robert Chris Adams-McGavin performed AFM measurements, and Eric Mahoney assisted with the Raman measurements.

# Chapter 1 Introduction

This chapter will discuss the motivation of this thesis work to develop multi-scale materials for lab-on-a-chip (LOC) technologies. It will review the different components that LOC molecular sensors are comprised of for point-of-care (POC) diagnosis and explain how they benefit from multi-scale materials. Furthermore, it will review fabrication techniques to produce multi-scale materials conventionally, as well as through rapid prototyping methods. Finally, this chapter will conclude with the motivation, objectives, and organization of this thesis.

## 1.1 Background

Some of the background information provided here is reproduced or adapted from the following review articles: Ref. [1] with permission from C. Gabardo and L. Soleymani, Deposition, patterning, and utility of conductive materials for the rapid prototyping of chemical and bioanalytical devices, Analyst , The Royal Society of Chemistry © The Royal Society of Chemistry 2016 and Ref. [2] with permission from C. Gabardo, A. Hosseini, and L. Soleymani, A New Wrinkle in Biosensors, IEEE Nanotechnology Magazine © 2016 IEEE.

### 1.1.1 Lab-on-a-chip Devices for Point-of -Care Diagnostics & Their Fabrication Requirements

Diseases caused by bacterial infections are categorized within the broader group of infectious diseases or communicable diseases, which can spread directly or indirectly from one person to another. Along with bacteria, viruses, parasites, and fungi are considered pathogenic microorganisms since their infection, presence, and growth in the host eventually leads to disease. According to the World Health Organization, infectious diseases account as the cause for almost 20% of deaths worldwide, disproportionately afflicting the developing world.[3] For example, tuberculosis (TB), caused by the bacteria *Mycobacterium tuberculosis*, was classified as being second greatest cause of death due to a single infectious agent, leading to 1.5 million deaths in 2014.[4] Over 95% of these deaths occurred in low-income or middle-income nations.[5] Although there are many factors that contribute to these statistics, the inadequate and/or less accessible diagnosis techniques in these regions, as well as inappropriate subsequent antibiotic treatment are major contributors to the continued spread and mortality of this disease. Current bacterial detection methods, based on bacterial culture and drug susceptibility testing, are conducted in centralized laboratories, are expensive, are time consuming, and are unavailable to many resource-poor and remote communities. The lack of sufficient diagnosis of bacterial infections in these countries, ultimately leads to the further spread of disease due to the absence of treatment and of other disease management activities. Most bacterial infections have treatment available in the form of antibiotics; however, a growing number bacteria strains have developed genetic resistance to certain first-line or all antibiotics. Specific pathogen identification, along with the identification of genes related to virulence and antibiotic resistance, can play a crucial role in selecting the best drug treatment and in extending the useful therapeutic lifetime of an antibiotic.[6] Therefore, rapid and accurate diagnosis is the first step in preventing and, subsequently, eradicating infectious bacterial diseases, especially in impoverished areas.

There is an urgent need to create portable, fully automated, and integrated chip-based platforms for inexpensive species-specific detection of bacterial pathogens. Recently, there has been great interest in developing ‘lab-on-a-chip’ (LOC) or ‘micro-total-analysis-systems’ (μTAS) platforms for point-of-care (POC) diagnostics in resource-limited settings. These integrated devices seek to create microsystems incorporating several steps of a conventional assay into a single chip-based system, where microfluidic channels transport the sample from one assay step to the next. POC chips are designed to analyze small volumes of samples, while remaining i) highly specific, ii) highly sensitive, iii) rapid, iv) disposable, v) portable, vi) cost-effective, and vii) simple to operate, even by untrained personnel.[7] These platforms offer the ability to screen for multiple targets of interest through the integration of arrays of sensing elements on one chip device, with minimal off-chip sample preparation and reagents. LOC devices not only have applications in POC infectious disease diagnostics, but also in health monitoring and disease management of non-communicable and communicable diseases, as well as food, water, biological warfare, and environmental sensing.[8]

In addition to external or integrated devices for signal readout and processing, LOC devices for POC diagnostics are typically composed of two main sections: the biosensor and the bioprocessing/sample preparation (shown in Figure 1.1). Biosensors are analytical devices that sense specific biologically-relevant analytes (proteins, nucleic acids, metabolites, polysaccharides, lipids, etc.), many contained intracellularly, using a sensing element and a transducer. In these devices, bioaffinity detection is typically performed by immobilizing biomolecule capture probe layer onto the surface of a transducer, where it can selectively capture their target biomolecules of interest selectively.[9] This binding event will be transformed into a detectable signal using an optical,[10] electrical/ electrochemical,[11] or piezoelectric/ mechanical[12] transducer.

Conventional sample preparation for molecular assays involves several critical tasks, such as sample centrifugation or other separation methods, heating and cooling, mixing with large volume of reagents, filtration, concentration, purification, and amplification.[13] The steps involved in extraction, purification, and enrichment of specific biomolecules for detection require several reagents, complex and expensive equipment, and need to be performed by skilled laboratory technicians. These sample preparation tasks are critical components of diagnosis, however they are extremely difficult to perform in resource-limited laboratories, and nearly impossible to perform outside of the laboratory.[6]

For LOC devices, sample preparation for intracellular biomolecular assays can be divided into the following steps: cell concentration/ sorting, cell lysis, and molecular enrichment. Cell concentration and/ or sorting are required when the sample is complex and the target cell concentration is low. This step allows for target cells to be isolated from samples with many different cell types or other contamination so that accurate information can be obtained in the downstream analytical steps.[14] Methods for cell separation include microfiltration, dielectrophoresis (DEP), hydrodynamic flow and electroosmotic flow, magnetic methods, and fluorescence-activated cell sorting.[13] Since many target molecules, such as nucleic acids, are contained within the cell, the cells must be broken down to release the intracellular contents in a process referred to as cell lysis.

Many different methods of lysing cells in microfluidic LOC devices exist, and they can be divided into four main categories: physical/mechanical, chemical, thermal, and electrical.[15] Once the intracellular contents have been released from the cells, the molecules of interest may be extracted from the lysate and re-suspended in pure buffer to minimize background contamination of the detection/biosensing portion of the chip. Methods to separate the analytes of interest from other organelles and biological matter include silica based affinity techniques, electrostatic interactions, physical filtration, and magnetic particles.[15]

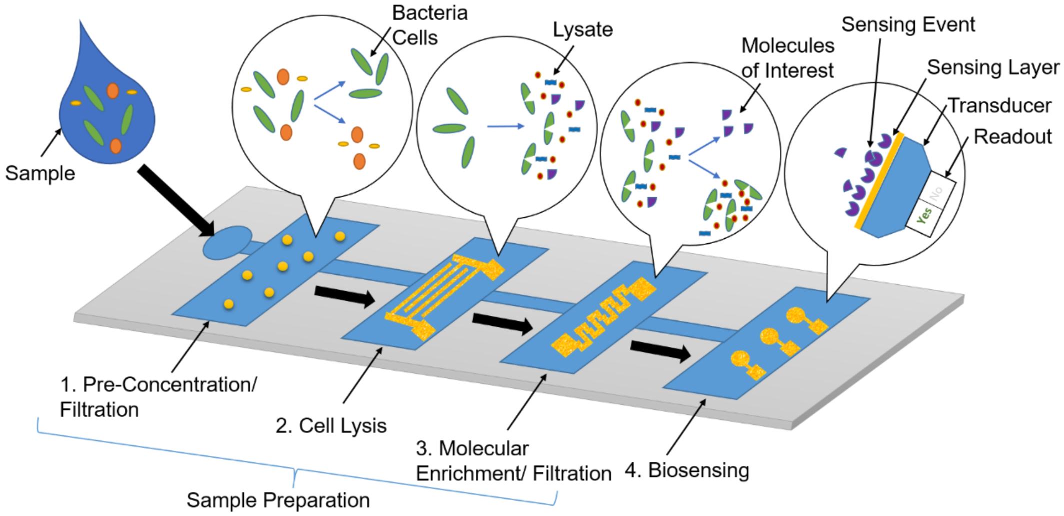

Figure 1.1 LOC process flow for diagnostics including sample preparation and biosensing.

Nature has become one of the biggest source of inspiration for engineering tunable multi-length-scale or hierarchical materials. There are countless examples of naturally occurring hierarchical materials, such as the wings of dragonflies,[16] adhesive structures of geckos,[17] or the self-cleaning structures of the lotus leaf.[18] Materials that have features that span the nanoscale and microscale, and even up to the macroscale, possess properties that are not seen in the bulk material or even in individual microscale or nanoscale materials.[19], [20] Hierarchical materials have been found to be advantageous to incorporate into many important applications including photovoltaics and photoelectrochemistry,[21], [22] tissue engineering,[23]–[25] drug delivery,[26], [27], and energy storage[28], [29], as well as they have been crucial in designing the next generation of LOC biosensor devices.[30]–[32]

Three distinct length-scales have been outlined as being important to the design of LOC biosensors: the dimensions of biological analytes on the nanoscale; the length-scale of biomolecular diffusion and the cellular length-scale on the microscale; and the volume of fluid in the processed clinical biological samples and chip dimensions on the macroscale.[33] All three length-scales must be considered to effectively engineer, not only for the biosensing portion of the LOC devices, but also the bioprocessing portion.

Considering the biosensing portion of LOC devices, the length-scales of the biomolecular analytes of interest, like DNA (2 nm in diameter and length of >6 nm for greater than 20 base pairs), and of biomolecular recognition between probe and target (1-10 nm) lie within the nanoscale range due to the Debye lengths.[33] Nanomaterials display unique properties, arising from the increased percentage of surface atoms compared to bulk materials, which lead to increasing surface area to volume ratios with decreasing dimensions.[34] The increased surface area to volume ratio of these materials increases the excess surface energy compared to bulk materials;[35] consequently, altering the size of the material varies the overall properties of the nanomaterial. The small size of nanoparticles leads to significant differences in their chemical properties. The higher curvature of nanoparticles causes increased strain within the crystal lattice, which can lead to higher reactivity.[36] Moreover, the greater surface area of nanomaterials leads to more potential interaction sites on the surface of the particle.[37] For instance, electrochemical DNA sensors produced from modified gold macroelectrodes or microelectrodes through surface area enhancing nanotexturing of the metallic surface on the length-scale of 1- 30 nm, has shown to improve the display of the probe strands of nucleic acids and the accessibility of target strands into the monolayer because of the increased deflection angle between probes.[31], [38] Also, electric fields have been shown to concentrate locally around certain high aspect ratio nanomaterials.[39] For example, Shahini et al [39], [40] modified stainless steel electrodes with randomly oriented carbon nanotubes (CNTs) and incorporated them into flow-through electroporation devices to obtain lower voltage requirements[39] and higher efficiencies[40] compared to unmodified bulk macroelectrodes for the lysis of bacterial and mammalian Chinese hamster ovary (CHO) cells, respectively. They concluded that the strong electric field enhancement at the CNTs was the cause of the enhanced performance of their devices and was a result of the “lightning rod effect”, a well-known effect that occurs due to the accumulation of charges over the sharpest feature of an object. Likewise, nanoscale features are advantageous in biofiltration devices where magnetic beads are selectively trapped for cell sorting or biomolecule filtration applications.[41], [42] Through the addition of sharp nanoscale features on micropatterned strips, large magnetic field gradients will form close to high-aspect ratio and narrow regions, allowing for more efficient capture of beads for passively operated devices.[43] Moreover, the depletion or accumulation of charge carriers at the surface of nanomaterials can affect the entire cross-sectional conduction pathway of these nanostructures for semiconductor field effect devices. This allows for ultrasensitive electrical DNA detection (tens of femtomolars) using two terminal silicon nanowire devices that selectively bind DNA targets with peptide nucleic probes on the nanowire surfaces, ultimately leading detectable changes in the conductance of the nanowires.[44] Furthermore, the alteration of optical properties of materials, such as localized surface plasmon resonance (LSPR)[45] and light scattering, can be observed at the nanoscale. Raman spectroscopy, an optical sensing technique, has shown dramatic increases in signal intensity (enhancements $\geq 10^4$) with the use of nanotextured substrates or tags, leading to creation of the surface enhanced Raman spectroscopy (SERS) method.[46] SERS enhancements are thought to be mainly the result of the electromagnetic field enhancement caused by the excitation of local surface plasmons on the substrate. Smaller contributions to this enhancement also occur through the chemical effect, due to the charge transfer between the chemisorbed species and the substrate.[47] SERS has been employed for femtomolar detection of DNA,[48] as well as single molecule detection.[49] In summary, nanoscale features predominantly affect the sensitivity of biosensors and power requirements/efficiency of bioprocessing devices.

On the microscale, materials tend to be more chemically and physically stable,[28] are an appropriate size to interact with cells which have dimensions in the same regime, and can easily bridge the gap between the nanoscale and the macroscale. Microscale features of electrode-based biosensors are important because they are on the same length-scale as the diffusion of biomolecules. Diffusional mass transport of biomolecules of interest take place on the 10 μm to 100 μm length-scale in solution for molecules, such as proteins and nucleic acids, with diffusion coefficients of sub-ten to hundreds of $\mu m^2/s$. Computational analysis shows that having nanoscale dimension sensors may produce devices capable of detecting analytes at sub-picomolar concentrations; however, the time to accumulate sufficient biomolecule quantities on the sensor at femtomolar or lower concentrations through diffusion may be too long for practical applications (hours to days).[50], [51] However, the number of molecules accumulated at the sensor is significantly greater when larger sensor dimensions and flow conditions are used in the system, for sensors greater than 10 μm in size.[50], [52] Moreover, the geometry of the sensor greatly affects the accumulation time of biomolecules, where two-dimensional and three-dimensional geometries capture analytes more rapidly and with a higher sensitivity than planar sensors.[51] Therefore, microscale, non-planar sensors are necessary to shorten response times for these systems, as well as improve sample/ electrode interaction.

Hierarchical materials, with features on multiple length-scales, have shown to overcome some of the limitations of biosensor and bioprocessing devices that are fabricated with materials featuring only one length-scale. For example, electrodeposited metallic nanostructured microelectrodes were employed to electrochemically sense trace levels of bacteria in under 30 minutes.[30] The microscale footprint of the sensor allowed for the target bacteria mRNA accumulation time to be short, while the nanoscale features (10-50 nm) aided in the probe display for the efficient capture of the target mRNA molecules. Other electrochemical biosensors have benefitted from millimeter scale interdigitated electrode arrays consisting of microscale electrodes with nanoscale gaps.[53]  In this case, the wide microscale electrodes allow for a large surface area for redox reactions to take place, the large number of finger electrode pairs allows for an increase in the number of redox reactions occurring, and the nanoscale gaps between the working electrodes decrease the diffusion length of the reduced or oxidized molecules at each working electrode. Another electrochemical biosensor has used hierarchically structured nanotextured microelectrode arrays to produce a superhydrophobic surfaces engineered to provide stable non-faradaic electrochemical impedance spectroscopy measurements of the sample as it evaporates and, consequently, the concentration of DNA in the sample increases.[54] While the microelectrode array with microscale height is necessary to effectively elongate the droplet and deliver the sample between adjacent electrodes, the nanotexture of the electrodes provides the localization of the sample drop to cause it to evaporate evenly over time, resulting in reproducible and stable measurements over time. Moreover, electrodeposited metallic nanostructured microelectrodes have exploited the lightening rod effect to lyse bacterial cells at relatively low voltages for RNA extraction.[55] While the nanoscale structures provide an enhancement in the electric field generated, the microelectrodes are closely spaced together so that they are operated at relatively low voltages, but spaced far enough apart so that cells can flow between them and the interaction volume with the high electric field remains large. Furthermore, DNA bio-barcode assays rely on nanoparticles with high surface- to-volume ratios to bind reporter groups for biomolecular detection and microscale particles with lower surface-to-volume ratios and large magnetic cores to allow them to be captured easily using an external magnetic field.[56] It is evident that having materials with features on multiple length-scales are essential for the design of functional biosensing and bioprocessing devices.

Finally, features on the macroscale, dimensions covering the millimeter and centimeter range, are necessary for interfacing with macroscale systems that users will interact with. These macroscale systems provide power and readout from the micro/nanoscale electrical sensors and transducers on LOC platforms, as well as are necessary to contain the entire volume of liquid biological samples (typically mL) being processed.

The nanoscale, microscale, and macroscale of LOC devices must all be engineered to efficiently interact with clinical or other samples. A summary of length-scale engineered LOC devices, with the rationale for materials engineering at every length-scale is presented in Table 1.1. It is clear that on the nanoscale, features of less than 100 nm have a significant effect on the device performance in terms of sensitivity or power requirements. For microscale features, footprints of electrodes that are larger than 10 μm aid in decreasing the time for mass transport to the component and a faster response time of devices. Engineering devices that meet these defined feature sizes is critical for optimizing LOC device performance.

| Length-scale | Device Purpose | Device Composition | Characteristic Lengths | Mechanism of Enhancement |
|---|---|---|---|---|
| Nanoscale | Electrical cell lysis | Modified stainless steel electrodes with randomly oriented carbon nanotubes (CNTs) [39], [40] | CNTs 2–6 nm diameter and 6 mm length | Lightening rod effect |
|  | DNA electrochemical biosensor | Dendritic gold structures on macroelectrodes[38] | Sub-100 nm radius of curvature | Probe display/ accessibility/ hybridization efficiency, Surface area |
|  | DNA electrical biosensor | p-type silicon nanowire two terminal devices[57] | 20 nm diameter | Sensitivity to surface conductance changes in the bulk |
|  | DNA SERS biosensor | Gold nanoparticles enlarged with silver electroless deposition[48] | 13 nm initial gold particle size | Electromagnetic enhancement (SERS) |
| Microscale | Surface Based Biosensors | N/A, simulations [50]–[52] | >10 µm footprint of sensor, 3D sensors | Mass transport enhancement |
| Hierarchical | Electrical cell lysis | Electrodeposited gold nanostructured microelectrodes [55] | Microelectrodes spanned 20–40 µm, sub-100 nm radius of curvature for nanostructures | Lightening rod effect, large volume of sample interacting with electric field |
|  | DNA electrochemical biosensor | Electrodeposited nickel nanostructured microelectrodes[54] | 30 microelectrodes (10 µm width, 8–9µm, and 4 mm length, nanoscale roughness of 300±70 nm | Super-hydrophobicity, Volume of sample interacting with electrodes, elongation of sample drop |
|  | mRNA electrochemical biosensor | Electrodeposited gold and palladium nanostructured microelectrodes[30] | 100 µm footprint of microelectrode, 10 to 50 nm nanoscale features | Probe display/ accessibility/ hybridization efficiency, Surface area, Mass transport enhancement |
|  | Poly-aminophenol electrochemical biosensor | Millimeter interdigitated electrode array, with microelectrodes and nanogaps [53] | 2 mm x 1 mm array, 10 µm x 2mm microelectrode , 250 nm-800 nm nanogap | Large surface area, Mass transport enhancement |
|  | DNA-bio barcode assay for protein detection | Gold nanoparticles and magnetic polyamine microparticles with magnetic iron oxide cores [56] | 1 µm diameter magnetic microparticles | High surface-to-volume ratio, easily capture magnetic beads |

Table 1.1 Summary of LOC device components and critical length-scales for enhancing performance.

### 1.1.2 Conventional Fabrication Methods

Conductive electrodes are critical components of electrochemical and electrical sensors and transducers, as well as sensors relying on the surface plasmon enhancement process. In conventional microfabrication, there are four basic steps (outlined in Figure 1.2): deposition, patterning, doping, and etching.[58] The electrode material deposition for LOC is carried out using physical vapour deposition (PVD) (sputtering and evaporation), electroplating, or chemical vapour deposition (CVD) techniques borrowed from the semiconductor industry. Moreover, the methods of the semiconductor industry have also been used for patterning micro/nanoscale electrodes for LOC devices, the most commonly used being photolithography.[59] Photolithography involves covering a substrate with a photo-sensitive polymer (photoresist), then exposing it to a UV sensitive light source through a photomask with the defined pattern. The pattern on the photomask will be transferred to the photoresist, then the patterned photoresist will be used as a mask for subsequent substrate etching (removal of material) or deposition of materials for liftoff patterning of materials that are difficult to etch.

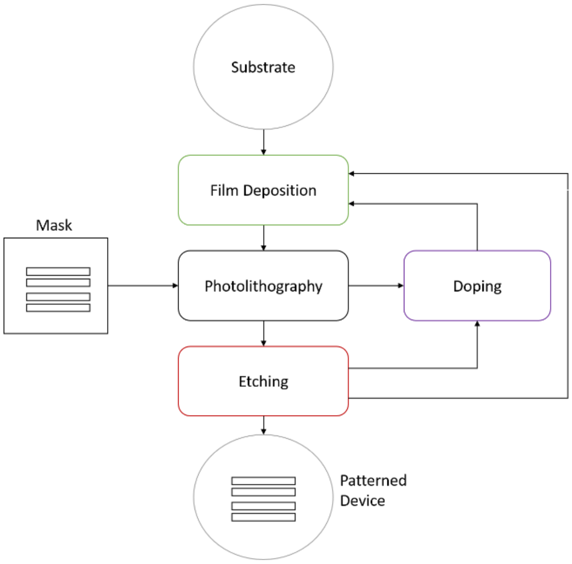

Figure 1.2 Flow diagram of conventional fabrication of patterned devices. Adapted from Ref. [58].

Due to its widespread use in the semiconductor industry, silicon was the initial substrate of choice for LOC system fabrication, with the first such silicon-based device reported in 1979.[60] It was initially thought that silicon chips patterned using the methods of the semiconductor industry would be the ideal platform for fabricating LOC devices. However, it was later realized that several sensing technologies relied on optical readout in the visible and UV range, for which silicon was not an appropriate material due to its strong absorption in these wavelengths. Furthermore, many of the electrical and electrochemical sensing techniques did not rely on the semiconductive properties of silicon and required the surface of the silicon wafer to be passivated by a thick oxide layer. As a result, it became difficult to justify the high cost of high quality silicon wafers used in the microelectronics industry for these applications.[61] In the early 1990s, glass became a predominant substrate material for LOC devices.[62], [63] Similar processing techniques as silicon – photolithography, etching, film deposition, and bonding – can be applied to glass. Glass has high temperature, chemical, and electrical resistance, as well as optical transparency. While less expensive than silicon, glass is still more expensive than polymer substrates, the substrate choice for this work and discussed in the following section, and lacks flexibility and compatibility with roll-to-roll manufacturing processes.

While fabrication methods and materials from the semiconductor industry are ideal for high precision and large volume production, they are high-cost technologies and the investment to maintain photolithographic facilities limits the accessibility for LOC developers. These methods are complex (in terms of the number of masks and processing steps needed) or non-ideal for creating three-dimensional, high aspect ratio, and hierarchically-organized materials, which are optimized over multiple length-scales for use in biosensing. Furthermore, they are not well-suited for rapid prototyping and low- to mid-volume production that is necessary in product development, testing, and performance characterization.

### 1.1.3 Rapid Prototyping

Over the past decade, there has been a growing interest in rapid prototyping methods that allow a functional device to be realized from a concept in a matter of a few hours. Rapid prototyping is a critical step to reduce the time-to-market in the product development cycle of miniaturized chemical and bioanalytical devices. While high throughput manufacturing methods are often preferred for large-volume production, rapid prototyping is necessary for demonstrating and predicting the performance of a device, as well as performing field testing and validation before translating a product from research and development to large-volume production. The device development process is iterative in nature, meaning that it is designed, tested, and optimized repeatedly until it performs as expected. Therefore, device cost and fabrication time must be minimized through rapid prototyping to expedite this process.

In an effort to reduce cost and produce single-use devices, polymer substrates became an intense area of study for LOC devices in the late 1990s and early 2000s, and remain one of the leading substrate choices today.[64]–[67] Furthermore, the flexibility of many polymer substrates enables the fabrication of devices with new form factors and makes it possible to manufacture devices using high throughput and low cost roll-to-roll processes. Polymers can be categorized according to their physical properties into the following groups: thermoplastics, elastomers, and thermosets.[68] Thermoplastics are not cross-linked, meaning that the polymer chains have the ability to move inside the bulk material, especially at temperatures above the glass transition temperature of the polymer. Commonly used thermoplastics in the area of LOC include poly(methyl methacrylate) (PMMA), polycarbonate (PC), polystyrene (PS), polyethylene (PE), polyethylene terephthalate (PET), and cyclic olefin copolymer (COC).[69] Elastomers are weakly cross-linked and can be easily stretched, then return to their original state when the stress is released. By far, the most commonly used elastomer in the area of LOC is polydimethylsiloxane (PDMS) due to its compatibility with soft lithography, gas permeability, optical transparency, non-toxicity, controllable surface chemistry, reversible deformability, and ability to be bonded to itself or other materials reversibly or irreversibly.[70]–[72] Finally, thermosets are polymers that are highly cross-linked, and therefore, are more stiff and temperature stable after curing. Thermoset polyesters are examples of thermoset polymers used in LOC devices as substrates.[73], [74] Polymer substrates are often selected according to their physical and materials properties to address specifications, such as biocompatibility, optical transparency, mechanical stability, thermal stability, and electrical conductivity imposed by the device application and the manufacturing processes used.[75]–[78] Polymers are ideal as device substrates for rapid prototyping techniques since they are compatible with a variety of rapid fabrication techniques and are low cost compared to alternative substrates.[79]

For conductor deposition, high purity materials can be deposited with precise thickness and high degree of uniformity using PVD and CVD techniques; however, these methods rely on expensive vacuum-based instrumentation placed in cleanroom environments, which add to the complexity, cost, duration of these processes. Therefore, alternative methods of conductive material deposition, applicable to rapid prototyping, have been developed or borrowed from other fields for fabricating miniaturized chemical and bioanalytical devices. These methods include electrochemical techniques (electrodeposition,[80] electroless deposition,[81] electropolymerization[82]), inks or liquid metal deposition (inkjet printing,[83] painting/writing,[84] 3D printing[85], screen printing,[86] stamping,[87] flexography/gravure,[88] electrophoretic deposition,[89] spray coating,[90] spin coating,[91] and drop casting[92]), electrospinning[93]/ electrospraying[94], and powders (abrasion, [95] embedding[96]). The majority of these methods are considered all-solution processed, where liquid phase conductors or conductor precursors are coated onto the substrate more rapidly and at a much lower cost than conventional deposition techniques. However, these methods often suffer from adhesion and conductivity issues without high temperature post-printing steps, like sintering, which are incompatible with many polymer substrates.[97]

Patterning is a necessary step for creating electrodes that have specific configurations, morphology, and structure. This can be accomplished using masks to define the electrode pattern or without the use of a mask. While photoresist is employed as the masking material in conventional photolithography, several rapid and less expensive alternatives have been developed for masked-based rapid prototyping. For example, xurography, or razor writing, uses cutting plotters to define electrode patterns into a mask material.[98] These instruments have been used to create lines as narrow as 6 µm with separations of ~20 µm to be created onto masking materials.[98] Adhesive polymer films can be patterned into masks that can be applied directly to the substrate prior to conductor deposition. Similarly, laser engraving/cutters can be used to pattern masks, such as patterned adhesive polyvinyl chloride tape for through mask electrodeposition,[99] or they can be used to pattern the electrode layout directly into the substrate.[100] In addition, etch masks have been rapidly produced using permanent markers[101], [102] or toner mediated lithographic transfer,[103], [104] which can have resolutions as small as 60 µm[101] and 100 µm[105], respectively. Moreover, masks can also be self-assembled/ self-organized, such as those formed using colloidal lithography[106] or anodized aluminum oxide.[107]

Alternatively, conductors can be patterned without masks using direct write or stamping techniques. Direct write/stamping methods are processes that precisely deposit or remove the conductive materials onto/from a substrate in pre-defined locations, typically in a pixel-by-pixel manner, such as pen-on-paper[84]/ pencil-on-paper[108], 3D printing[85], micro-contact printing[109]/nano-contact printing[110], inkjet printing,[111] and laser direct write[91], [112],[113]. Because direct write is typically a serial process, it can take longer to pattern the entire electrode device compared to other printing techniques where the entire electrode pattern is transferred at once. Lastly, conductor nano-/micro-patterning can be realized through directed-assembly/structuring methods where external forces are used to control complex three-dimensional nano- and microscale patterning, such as electrophoretic deposition[114], electrodeposition[115], and wrinkling[116]. Wrinkling is discussed in further detail in Chapter 2. The discussed rapid prototyping patterning methods are summarized in Table 1.2.

Many rapid prototyping methods have been developed or adapted from other industries in recent years to expedite LOC device and sensor development in laboratory settings. However, few methods are able to create robust electrode devices with controllable features that span the nanoscale to the macroscale, as well as with high conductivity and adhesion. Therefore, there exists an opportunity to develop rapid fabrication techniques to create multi-scale electrodes that meet the functional and application-driven demands of LOC devices.

| **Patterning Category** | | **Examples of methods** | **Advantages** | **Disadvantages** |
|---|---|---|---|---|
| | Methods to make masks | | | |
| **Masked patterning** | *Self-Assembly/ self-organized* | Colloidal lithography[106], anodized aluminum oxide[107] | High throughput for repeating patterns, nanoscale to microscale patterning (typically 2D structures) | Defects often present and/or suffer from lack of reproducibility, precise and reproducible structural control difficult to achieve, sometimes need external equipment for processing |
| | *Printing* | Marker drawn[101], [102], toner mediated lithographic transfer[103], [104] | Pattern layout can be easily and rapidly changed, simple equipment | Direct write is a serial process (can take long to pattern device), limited to microscale 2D patterning |
| | *Cut Masks* | Xurography[98], laser engraving[99],[100] | Pattern layout can be easily and rapidly changed | Limited to microscale 2D patterning, more specialized equipment needed |
| **Mask-free Patterning** | *Direct Write/ Stamping* | Pen-on-paper[84]/ pencil-on-paper[108], 3D printing[85], micro-contact printing[109]/nano-contact printing[110], inkjet printing[111], laser direct write[91], [112].[113] | Pattern layout can be easily and rapidly changed, simple equipment | Direct write is a serial process (can take long to pattern device), limited to microscale 2D patterning (but 3D printing allows for 3D microstructures) |
| | *Directed-Assembly/ Structuring* | Electrophoretic deposition[114], electrodeposition[115], wrinkling[116] | Complex 3D architecture can be produced, patterning from nanoscale to macroscale | Poor reproducibility, need external forces/equipment to drive assembly, additional mask for electrode patterning |

Table 1.2 Summary of various rapid prototyping patterning techniques for LOC devices.

## 1.2 Motivation

LOC devices for use in POC diagnostics have attracted tremendous research and commercial interest over the past two decades. The ability to miniaturize the manual and labour-intensive processing and analytical tasks that are typically performed using large volumes of reagents, into integrated and microscale LOC devices is a very attractive and inexpensive alternative to traditional diagnosis systems. Though many LOC systems have been developed, the expense and time associated with translating them from a concept to a mass-producible device has slowed and limited their commercialization. Rapid prototyping offers a less expensive and expedited route to optimize LOC structures and electrodes in the development cycle. However, no such method is robust enough to controllably pattern three-dimensional and multi-length-scale materials, critical components for optimizing LOC performance, on its own without the need for expensive equipment. Moreover, all-solution processed electrodes often suffer from low quality deposition and substrate compatibility issues, leading to electrodes with insufficient conductivity and adhesion.

The motivation of this thesis is to overcome the shortcomings of the current multi-scale engineering technologies, which includes the requirement of expensive equipment and facilities, the time consuming and labour intensive fabrication steps, the long design-to-device turnaround times and, consequently, long delays in the iterative prototyping process for specific applications. Ultimately, we aim to develop robust, affordable, and high-speed benchtop fabrication techniques to rapidly prototype tunable, multi-scale, three-dimensional materials for integration and application to LOC devices. This involves developing new fabrication methods that combine xurography, wrinkling, and all-solution processed conductor deposition to create structurally tunable hierarchical electrodes for performing functional experiments. While these rapid prototyping techniques have been utilized individually by others to fabricate devices, what makes this research unique is the combination of techniques to overcome the shortcomings of each method. Using these techniques, we look to understand the structural evolution of the electrodes through the fabrication process and varying processing parameters, as well as thorough characterization of the features at the nanoscale, microscale, and macroscale. We seek to advance our understanding of the effect of the structure on the function of the electrode, then to link the function to the application driven function. Moreover, we look to apply these fabrication methods to create structurally optimized LOC electrode devices and sensors. Finally, we aim to integrate these electrode devices with microfluidics to create contained LOC devices.

### 1.3 Objectives

The objectives of this research are summarized below:

A. <u>Enhancing speed and decreasing expense of rapid multi-scale prototyping</u>

Engineering multi-length-scale materials, that span nanometer to millimeter dimensions, typically involves many time consuming and expensive processing steps, rendering them unsuitable for the rapid prototyping of LOC devices. In order to take advantage of the unique nano-/microstructures that result from the wrinkling process, and to enable device miniaturization, we explore the possibility of creating multi-scale, high surface area metallic electrodes using wrinkling, in combination with other robust benchtop technologies, like xurography for electrode patterning. Furthermore, we answer the question: can these multi-scale electrodes be produced, from design to device, in only a few hours and at <$1 per device?

B. Developing all-solution processed conductor deposition methods compatible with new prototyping technique

Sophisticated vacuum-based instrumentation and facilities, such as clean rooms, contributes to the cost and time associated with PVD or CVD methods for high quality conductor deposition and limit their use for rapid prototyping device development on the benchtop. Electrode materials to be used in LOC devices must display sufficient conductivity, chemical stability, and physical compatibility with substrate for good adhesion; however, many all-solution processed methods do not meet these requirements. We explore all-solution processed benchtop techniques to deposit conductive materials on pre-stressed polymer substrates, like electroless deposition and layer-by-layer deposition, to create electrodes for integration in LOC devices and substrates for surface enhanced Raman spectroscopy (SERS), respectively. Since these are among the first examples of all-solution processed and self-assembled wrinkled materials, we perform a thorough characterization of the structural properties; like minimum feature size, surface roughness, and porosity; and functional parameters, such as surface area and resistance. We search the synthesis parameter space to structural tune for functional LOC devices. We demonstrate their compatibilities with the xurography and wrinkling patterning techniques to produce high quality functional devices, ultimately to eliminate the reliance of vacuum-based technologies for device fabrication.

### C. Tuning and understanding structural evolution of electrodes

The versatility of electrodes to different applications is highly dependant on their ability to be structurally tuned for various functions. We explore ways to structurally tune the electrodes on the microscale and the nanoscale, using sputtering, electrodeposition, electroless deposition, and/or layer-by-layer assembly. Through the variation of the conductor deposition parameters for each technique we demonstrate structural tunability for the resulting electrode. We characterize the development of each structure in terms of morphology and topography using scanning electron microscopy(SEM)/transmission electron microscopy (TEM) and white light interferometry/ atomic force microscopy (AFM). We ask: how can we alter the multi-scale structure or add additional structural hierarchy?

### D. Correlating electrode structure to functional characteristics and application- driven function

The nano/micro-architecture of sensors and transducers has been shown to directly impact their functional characteristics and performance. We characterize the functional parameters that are critical for sensors and transducer performance, such as resistance and electroactive surface area, while varying the structures of these devices. We seek to correlate the structure to device performance for LOC applications. Specifically, we study the effect of the electrode structure on the voltage requirements of electrical cell lysis to overcome the high power consumption of existing cell lysis devices. We look to understand the mechanism of the structural enhancement on the application-driven function through numerical simulations and additional experiments. Moreover, we study the effect of structural tuning of the metallic surfaces when applied as SERS substrates. We ask: How and why does the structure of the electrodes impact their function in a variety of specific sensing and bioprocessing applications?

### E. Integrating three-dimensional textured electrodes with microfluidics

The integration of sensing and bioprocessing elements within fluidic channels of microscale dimensions is required for LOC platforms for POC diagnostics and many other applications, in order to contain the samples and aid in mass transport. However, microfluidic systems bonded over high topography electrodes suffer performance issues related to leakage, and we study the cause of these issues in order to gain a better understanding of these systems and to engineer a solution to this problem. We determine that encapsulating three-dimensional electrodes with substantial height becomes particularly difficult to achieve in such devices due to microscale voids that form at the interface between the substrate, electrode, and microfluidics, leading to leaks. Moreover, bonding microfluidics to unconventional substrates, like shape memory polymers, is not well-established. We explore different bonding techniques to circumvent the bonding over tall electrodes and to unconventional substrates issues to create integrated electro-fluidic devices easily, inexpensively, and on the benchtop.

## 1.4 Overview

The remainder of this thesis is arranged as follows:

Chapter 2 provides background information on the wrinkling process used throughout this thesis work, including wrinkling theory and wrinkling fabrication process.

Chapter 3 focuses on the development of the rapid prototyping process to create hierarchically structured wrinkled miniaturized metallic electrodes using xurography (vinyl craft cutting), sputtered thin film deposition, and shape memory polystyrene substrates in a few hours. The thickness of the deposited thin metallic layer is varied to tune the high surface area wrinkled electrode structure and functional properties. These electrodes are applied as electrochemical sensors to demonstrate the high device-to-device reproducibility and the advantage of the greater surface area of these devices. Additional nanostructuring and surface area enhancement of the electrodes is achieved through the electrodeposition of gold structures on the wrinkled gold film.

Chapter 4 concentrates on the application of the rapid wrinkling fabrication process, discussed in Chapter 3, to create interdigitated microelectrodes for a LOC bioprocessing application of electrical bacterial cell lysis. Flat, wrinkled, and electrodeposited wrinkled electrodes are tested to study the effect of electrode structure on voltage requirements and cell lysis efficiency. Cell lysis is assessed in terms of cell viability, membrane permeability, and nucleic acid release and the mechanism of lysis is explored through numerical modelling of Joule heating and electric field strengths.

Chapter 5 focuses on the integration of the wrinkled electrodes on PS substrates, fabricated using the technique discussed in Chapter 3, with PDMS microfluidics to create contained electro-fluidic devices. Various bonding methods between PS substrates with tall wrinkled electrodes and the PDMS microchannels are assessed through flow rate and burst pressure testing, in combination with electron microscopy to study the interface between the substrate and the microfluidic system at the micro/nanoscale. The bonding technique that can withstand the highest flow rates and burst pressure is applied to create an electrochemical flow cell, which is subsequently tested under flow and no flow conditions with a standard redox agent.

Chapter 6 expands on the rapid prototyping method described in Chapter 3, concentrating on the development of an all-solution processing based approach to create wrinkled electrodes and eliminate the need to use sputtering to deposit the metallic layer. Electroless deposition is employed to create tunable wrinkled porous and non-porous electrodes. The structural and functional properties of the electrodes are assessed for various electroless deposition times using SEM, TEM, AFM, white light interferometry, four-point probe measurements, and electrochemical characterization; then, these wrinkled films are applied as substrates for chemical sensing using SERS as a proof-of-concept sensor.

Chapter 7 expands on all-solution processing based methods to engineer multi-length-scale wrinkled metallic surfaces, through the self-assembly of gold nanoparticles to form the film layer on shape memory polymers. Wrinkle sizes are tuned by varying the nanoparticle diameter and the number of nanoparticle layers. The effect of the gold nanoparticle density and wrinkling of these films on the intensity of the obtained spectra when they are employed as SERS substrates for the chemical sensing of analytes is studied.

Chapter 8 focuses on the conclusions of this research, providing a summary of the key findings, contributions to the field, and potential future work.

# Chapter 2 Background on Wrinkling Theory and Fabrication

This chapter discusses the background on the wrinkling structuring technique that is used throughout this thesis work. The theory and implementation of this rapid prototyping structuring method is described, as well as applications that have employed this technique in functional devices are discussed. Some of the information provided here is reproduced or adapted from the following review article: Ref. [2] with permission from C.Gabardo, A. Hosseini, and L. Soleymani, A New Wrinkle in Biosensors, IEEE Nanotechnology Magazine © 2016 IEEE.

## 2.1 Wrinkling as a Method of Structuring

Wrinkling, the process where films form creases or folds as they experience forces that compress them into a smaller geometric region, is a phenomenon that is familiar to most people and seen in many places in nature. The flesh of fruit as it dries out and the human skin as we age are examples of wrinkling observed in everyday life. The wrinkling process discussed here will focus on systems with stiff films/ skins bound to elastic /viscoelastic substrates. When compressive strains are experienced by the films in such systems, the stress is relieved through periodic buckling of the film in the direction perpendicular to the experienced force.[2] The buckles that are formed produce wrinkles with amplitudes much greater than the original film thickness and the footprint of the film can be reduced significantly. Ordered micro- and nanoscale wrinkles on metallized polydimethylsiloxane (PDMS) substrates, a commonly used elastomer in microfluidics, was first reported by Martin et al in 1981,[117] and was studied by Bowden et al almost two decades later in 1998.[118] Since the latter work, much theoretical[119] and experimental[116], [120] research has been devoted towards understanding, predicting, and controlling the resulting micro-/nanoscale wrinkled topography of film/ substrate systems to be used for a variety of applications in micro- and nanotechnology.

## 2.2 Wrinkling Theory

Many studies on wrinkle formation have developed mathematical models for the buckled topography.[119]–[124] A simple uniaxial model of the compressive force ($F$) experienced by a film ($f$) strongly coupled to an infinitely thick elastic substrate ($s$), neglecting any shear stress between the film and substrate, can be given by[121], [125], [126]:

$$F = E_f \left[ \left(\frac{\pi}{\lambda}\right)^2 \frac{w_f h_f^3}{3\left(1-v_f^2\right)} + \frac{\lambda}{\pi} \frac{E_s w_f}{\left(4\left(1-v_s^2\right)\right)E_f} \right] \qquad \text{(Equation 2.1)}$$

Where $E_f$ and $E_s$ are the elastic moduli of the thin film and the substrate, respectively, and $v_f$ and $v_s$ are the Poisson's ratio of the film and the substrate, respectively. The film has a width ($w_f$) and a thickness ($h_f$), and $\lambda$ denotes the wavelength of the sinusoidal profile that results as the film buckles under the compressive force. The compressive force ($F$)/ strain ($\epsilon$) must exceed critical value ($F_c$ /$\epsilon_c$) in order for wrinkling of the film to occur. The critical strain is given by Equation 2.2[127]:

$$\epsilon_c = \frac{1}{4} \left( \frac{3\left(1-v_f^2\right)E_s}{\left(1-v_s^2\right)E_f} \right)^{2/3} \qquad \text{(Equation 2.2)}$$

Figure 2.1 depicts a schematic of the wrinkling process of a film firmly attached to a substrate under compression. The critical wavelength ($\lambda_c$) of the wrinkles from a film undergoing this process can be obtained from $(dF/d\lambda) = 0$:

$$\lambda_c = 2\pi h_f \left(\frac{(1-v_s^2)E_f}{3(1-v_f^2)E_s}\right)^{1/3} \qquad \text{(Equation 2.3)}$$

It is evident that the wavelength scales with the cubic root of the material parameters of the film and substrates, as well as it scales linearly with the film thickness. Therefore, thicker and stiffer film layers are expected to result in larger wrinkles. The amplitude of the wrinkles ($A$) is given by Equation 2.4 [116]:

$$A = h_f \left[\frac{\epsilon}{\epsilon_c} - 1\right]^{\frac{1}{2}} \qquad \text{(Equation 2.4)}$$

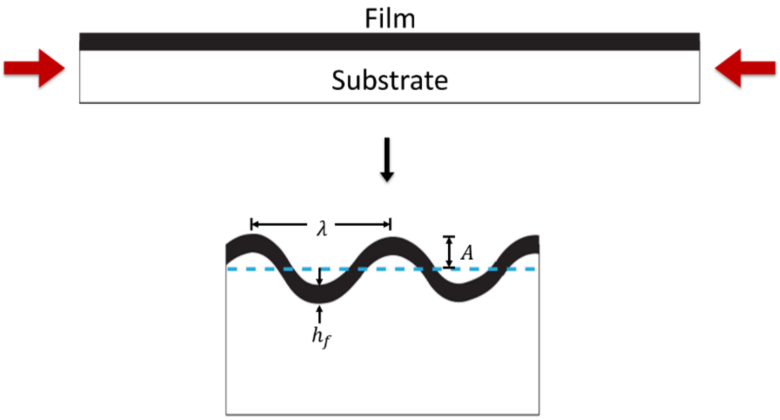

Figure 2.1 A schematic representation of the uniaxial wrinkling process. Where $h_f$ is the film thickness, $A$ is the amplitude of the wrinkles, and $\lambda$ is the wavelength of the wrinkles. Figure reproduced from reference [2] with permission from C. Gabardo, A. Hosseini, and L. Soleymani, A New Wrinkle in Biosensors, IEEE Nanotechnology Magazine © 2016 IEEE.

When films experience large strains, multi-generation or hierarchical wrinkling can occur. The compressed film will buckle and wrinkle to release some of the strain, according to Equation 2.3, and subsequently, the first generation of wrinkles in the film can effectively act as a thicker and stiffer film. This new effective film ($f_{eff}$) is able to undergo future generations of wrinkling if the remaining strain still remains larger than the critical strain value.[122] The wavelengths of the subsequent generation of wrinkles can also be predicted according to Equation 2.3; however, the film and substrate parameters will be the effective parameters of the previous generation of wrinkled films and substrates ($E_{f_{eff}}, E_{s_{eff}}, v_{f_{eff}}, v_{s_{eff}}, h_{f_{eff}}$). This wrinkling behaviour can be scaled for many generations of wrinkles and over many length-scales, until the strain has reached value that is below the critical strain value.

The wrinkling behaviour described thus far has been for the uniaxial strain cases, where compression is applied in only one lateral dimension. However, compressive strains can be applied in both lateral directions, which results in biaxial wrinkling. In this case, the interference of wrinkles in perpendicular directions resulting in defects and less ordered structures.[119] The distance over which wrinkles in the biaxial case lose their orientation coherence ($\xi$) has the following relationship: $\xi \propto h \left( E_f / E_s \right)^{\frac{2}{3}}$.[128]

These mathematical models have allowed researchers to predict the wrinkled film topography in systems with various material systems and boundary conditions. Research in this field has progressed towards controllably wrinkling materials as a method of surface patterning and exploiting these interesting structures for functional applications.

## 2.3 Fabrication of Wrinkled Devices

Several techniques have been employed to controllably create ordered wrinkles in film/ substrate systems; however, the majority of these methods encompass three basic steps: 1) the extension/ expansion of the substrate, 2) the deposition/formation of the thin film, and 3) the compression/release of the substrate.[2] Alternatively, the film layer can be forced to wrinkle through swelling, which can be induced through subjection to plasma,[129] lasers,[130] solvents,[131] etc., without modifying the substrate layer. However, the film layer in these cases is typically polymeric and these treatments may not be suitable for fabricating wrinkled surfaces with metallic film layers. As mentioned previously, metallized PDMS substrates were the initial material systems studied for microscale wrinkle formation, and since then they have been highly utilized for other studies and device applications. [116]–[118], [132]–[134] In order to induce volume expansion or lateral extension in this system, the PDMS substrates can be heated[135] or stretched[132], [136]. The surface of this pre-stressed substrate can be coated with a metallic film layer through conventional sputtering or evaporation methods. Finally, the substrate can be cooled, released, or compressed to exert the compressive force on the film and induce wrinkling of this layer. While PDMS has been used extensively in these systems, its limited deformation and lack of compatibility with high-throughput manufacturing techniques impede its potential scale-up for device fabrication.[137]

Shape memory pre-stressed polymers – semi-crystalline materials that have been heated over their glass transition temperature (the temperature at which polymers turn from hard and brittle to soft and flexible), stretched, and then cooled rapidly to remain in that stretched orientation – have also been used extensively as substrates for fabricating wrinkled thin films.[137] They present as attractive alternatives to PDMS substrates, as they can withstand high draw ratios and are compatible with roll-to-roll processing and other high-throughput techniques. In this case, the pre-stressed polymer substrate (polyethylene,[23] polyolefin,[138] polystyrene,[128] etc.) is coated with a thin film, then is heated over its glass transition temperature. This allows the polymer chains to relax and releases the stored elastic stress, resulting in the shrinking of the substrate to its initial size and the compression of the thin film into wrinkled structures. The number of axes being strained, the magnitude of the applied stress on the substrate, and the film properties/ material systems, can be used to control the resulting wrinkles in all the fabrication methods discussed.

## 2.4 Application of Wrinkled Devices

With the ability to tune the resulting structured surfaces, wrinkling has been applied as a fabrication method to create many lab-on-a-chip (LOC) and other miniaturized devices where structural tuning is critical to the device performance. For example, wrinkled metallic surfaces, gold and nickel/gold composites, have been applied to fluorescence-based sensing,[139], [140] In these cases, an enhancement in the fluorescence intensity is observed due to the metal enhanced fluorescence from the wrinkled surfaces. Additionally, nanoporous films, fabricated through the dissolution of silver from gold/silver alloys, have been wrinkled using pre-stressed thermoplastic sheets to produce substrates for surface enhanced Raman spectroscopy (SERS) sensing [49], [141]. The wrinkling produced sharp features and nanogaps in the metal layer, which aided in the electromagnetic enhancement of the devices, leading to single molecule detection of a chemical analyte. More recently, a mechanical strain sensor based on the piezoresistive effect was fabricated through the deposition of CNTs on a pre-stressed thermoplastic substrate and the transferring of the wrinkled CNTs sensors to a flexible substrate after the wrinkling process[142]. In this case, the wrinkled structures allowed for flexibility and stretchability of the sensor. Clearly, wrinkled surfaces have been beneficial for a variety of sensing applications.

In addition to the sensing applications, wrinkled surfaces produced from non-metallic materials (oxides, polymers, etc.) have been used for a variety of other applications that benefit from the multi-scale surfaces. These applications include employing them as surfaces for cell culture and tissue engineering,[23], [143], [144] as well as studying cell mechanical properties.[145] Because of the naturally occurring hierarchical topography observed in the body, wrinkled surfaces offer structuring that supports the alignment, adhesion, and growth of cells on these surfaces. Moreover, superhydrophobic surfaces have been created using wrinkled surfaces directly [146] or employing wrinkled surface as a mold for soft lithography to create the structures[147]. The roughness of these surfaces that support Cassie or partial Cassie wetting is due to the wrinkle-induced texture of the structures. The unique structures produced through wrinkling have found applications in a variety of areas of research, and as this structuring method is applied to new materials the possible applications will increase.

Finally, the application of wrinkling has also been extended to using it as a tool to measure thin film properties.[127] With the knowledge of the substrate mechanical properties, films can be wrinkled and the wavelength of the wrinkles extracted to determine the Young’s modulus of the film through the rearrangement of Equation 2.3. Moreover, wrinkling has been used to determine the stresses induced within a system through the wrinkle orientation and amplitude.[148] Therefore, surface wrinkling is both a versatile measurement and fabrication tool.

## 2.5 Summary

Wrinkling, a phenomenon seen in countless places in natures, can be employed as a novel method for creating topographically structured surfaces at the nanoscale and microscale. Using bilayer systems of stiff thin films on compliant substrates, the film layer can be induced to wrinkle by an applied compressional strain. The amplitude and wavelength of the resulting periodic structures can be predicted using theoretical models based on the applied strain, thickness of the film, and mechanical properties of the film and substrate layers. Bilayer systems consisting of shape memory polymers coated with thin metallic layers have been utilized to produce wrinkled surfaces that have been applied many LOC and other miniaturized devices. Although several applications of wrinkling have been demonstrated with this system, there exists opportunity to create unique three-dimensional multi-scale electrodes using this technique and explore new materials systems to develop electrodes with enhanced functionality.

# Chapter 3 Bench-Top Fabrication of Hierarchically Structured High-Surface-Area Electrodes

## Chapter Introduction (Objectives A, C, and D):

In order to create multi-scale electrodes for LOC applications, precise electrode layouts need to be defined and the micro/nanoscale features of the electrodes must be tuned. Moreover, the electrodes must demonstrate good adhesion and conductivity for practical applications. This chapter focuses on the development of a rapid patterning process to create miniaturized hierarchically structured high-surface-area electrodes on the laboratory benchtop from planar metallic thin films vacuum-deposited on pre-stressed polymer substrates. The patterning method combined three benchtop techniques: 1) the wrinkling technique discussed in Chapter 2, through heat-induced shrinking of the polymer substrates, with 2) xurography, vinyl mask production through craft cutting, and 3) electrodeposition of nanostructured gold, for the first time to create gold electrodes with features spanning the nanoscale to the millimeter scale (50 nm to 1 mm) in only a few hours and at less than $1 per device. While the wrinkling technique was critical in patterning and structuring of the electrode on the nanoscale to the microscale, the xurography-produced masks patterned these structures into a variety of microscale to macroscale layouts. The impact of fabrication parameters, such as gold film thickness and shrinking temperature, was investigated to determine the effects on the tuning of the structural parameters, such as topography, morphology, and roughness. It was found that, these structural parameters were related to the functional parameters of the wrinkled electrodes, such as hydrophobicity, sheet resistance, and electroactive surface area. The application of these multi-length-scale electrodes as highly reproducible electrochemical sensors was investigated using cyclic voltammetry with standard redox agents. Finally, electrodeposition, a benchtop patterning technique, was utilized to deposit additional structural hierarchy of nanostructured gold on the wrinkled electrodes and planar electrodes, and the role of the electrode structure on the resulting nanostructuring was investigated.

**Authors:** Christine Gabardo, Yujie Zhu, Leyla Soleymani, and Jose Moran-Mirabal

**Publication:** Advanced Functional Materials, 23, 24, 3030-3039

**Publication Date:** January 2013

### 3.1 Abstract

Fabrication of hierarchical materials, with highly optimized features from the millimeter to the nanometer scale, is crucial for applications in diverse areas including biosensing, energy storage, photovoltaics, and tissue engineering. In the past, complex material architectures have been achieved using a combination of top-down and bottom-up fabrication approaches. A remaining challenge, however, is the rapid, inexpensive, and simple fabrication of such materials systems using bench-top prototyping methods. To address this challenge, the properties of hierarchically structured electrodes are developed and investigated by combining three bench-top techniques: top-down electrode patterning using vinyl masks created by a computer-aided design (CAD)-driven cutter, thin film micro/nanostructuring using a shrinkable polymer substrate, and tunable electrodeposition of conductive materials. By combining these methods, controllable electrode arrays are created with features in three distinct length-scales: 40 µm to 1 mm, 50 nm to 10 µm, and 20 nm to 2 µm. The electrical and electrochemical properties of these electrodes are analyzed and it is demonstrated that they are excellent candidates for next generation low-cost electrochemical and electronic devices.

**Keywords:** microstructures, electrodes, nanostructures, thin films, electrochemistry

## 3.2 Introduction

Recently, there has been increased interest in fabricating hierarchical materials with morphologies tunable in the micron to nanometer scale. Natural hierarchical materials – optimized over multiple length-scales through evolution to answer specific functional demands – have inspired the synthesis of hierarchical materials with unique characteristics unparalleled by bulk materials.[19], [20] The properties of such materials can be tuned for specific applications by adjusting the material composition, geometry, and size of the structured features. In photovoltaic and photo-electrochemical energy conversion devices, hierarchically branched nanowires enable considerable improvement in the light absorption efficiency due to enhanced surface area and light scattering properties.[21], [22] Hierarchical structures have also found wide application as tissue engineering scaffolds because they mimic the multi-scale features found in biological niches, which not only offer structural support but also provide the microenvironment needed for cell proliferation.[23]–[25] In drug delivery, hierarchically-structured dendrimers are tuned to provide the required geometry, size, and surface chemical functionality to entrap or transport small drug molecules.[26], [27] Similarly, the integration of high surface area hierarchical structures on sensing electrodes dramatically improves the speed and sensitivity of electrochemical biosensors[30]–[32], [149] These applications highlight the potential that hierarchically structured materials present in the development of functional devices.

Various methods for the fabrication of hierarchical materials have been developed, such as multilayer photolithography,[150] electron-beam lithography,[151] templated self-assembly,[152] and soft lithography.[153] While these methods have been used to create nature-inspired hierarchical materials, they often need to be combined in order to span the entire millimeter to nanometer length-scale. As a result, they rely on at least one step that requires a mask, template, or a master that cannot be rapidly fabricated in the laboratory. Thus, it remains a major challenge to develop such materials systems using simple laboratory processes and to implement the entire process – from design to fabrication – in timescales from minutes to hours.

A facile and quick approach has been recently developed to fabricate micro- and nanostructured materials, which takes advantage of the thermal shrinking of pre-stressed polymer films, such as polystyrene (PS),[128] polyolefin (PO),[138] and polyethylene.[23] Printing onto PS substrates and shrinking has been used to generate micropatterned templates, which allowed the fabrication of rounded microfluidic channels with critical dimensions as small as 65 μm.[154] Through this shrinking approach, Fu and collaborators also created uniaxial and biaxial wrinkles on gold-coated PS sheets. They demonstrated that the wrinkle wavelength could be tuned by adjusting the thickness of the metal film.[128] More recently, the shrinking approach has been applied to create micro and nanoscale structures with cross-linked PO thin films, which exhibited larger shrinking ratios (up to 95%) and greater shrinking uniformity than PS substrates.[23] These shrinking methods offer an attractive route to the fast, easy and inexpensive bench top fabrication of micro- and nanostructured devices, which can aid in the development of functional microdevices.

Here, we present a method combining millimeter patterning through vinyl masking, micrometer stress-driven wrinkling, and nanometer electrodeposition for the controlled fabrication of electrodes with hierarchical structures spanning multiple length-scales. This process offers speed, ease of fabrication and cost-effectiveness in producing micro- and nanostructured surfaces. In addition, we show that electrodes fabricated in this fashion display excellent conductive and electrochemical properties, and can be used to monitor charge transfer and reduction/oxidation reactions. Furthermore, the hierarchically structured electrodes exhibited electroactive surface area enhancements in excess of a thousand fold when compared to flat electrodes. Altogether these results show that our approach to structuring conductive surfaces produces high surface area electrodes that can be incorporated into a variety of microdevices. This newly developed prototyping method could facilitate the design and prototyping of tunable material systems applicable to the fabrication of low-cost biosensing, bioprocessing, tissue engineering and photovoltaic devices.

## 3.3 Experimental

### 3.3.1 Reagents

Potassium hexacyanoferrate(II) trihydrate ($K_4Fe(CN)_6 \cdot 3H2O$, >98.5%), potassium chloride (KCl, ≥99.0%), hydrogen tetrachloroaurate(III) trihydrate ($HAuCl_4 \cdot 3H2O$,

>99.9%), hydrochloric acid (HCl ACS reagent, 37%) were purchased from Sigma-Aldrich (St. Louis, Missouri). Sulfuric acid ($H_2SO_4$, 98%) was purchased from Calden (Georgetown, Ontario). All reagents were of analytical grade and were used without further purification. Milli-Q grade water (18.2 MΩ) was used to prepare all solutions.

### 3.3.2 Device Fabrication

All devices were fabricated on pre-stressed polystyrene shrink films (Graphix Shrink Film, Graphix, Maple Heights, Ohio). Shrink film sheets were cleaned under orbital agitation (50 rpm) for 5 minutes in isopropanol, ethanol, and water baths, and were dried using a dry nitrogen stream. Self-adhesive vinyl sheets (FDC-4300, FDC graphic films, South Bend, Indiana) were laid over the cleaned shrink film sheets and evenly flattened with a hand roller. The desired gold film shapes were cut into the self-adhesive vinyl using a Robo Pro CE5000-40-CRP vinyl cutter (Graphtec America Inc., Irvine, CA) equipped with a CB09UA supersteel blade, with force, quality and speed set at 10, 1, and 1, respectively. The cut out shapes were peeled off from the shrink film using tweezers. The remaining self-adhesive vinyl was used as a mask during gold sputtering. Gold was deposited from a 99.999% purity gold target (LTS Chemical Inc., Chestnut Ridge, New York) using a Torr Compact Research Coater CRC-600 manual planar magnetron sputtering system (New Windsor, New York) onto the masked shrink film. The argon (>99.999% purity, AlphaGaz, Air Liquide, Montreal, Quebec) plasma was created by a DC current of 37 A, which allowed for a typical gold deposition rate, monitored by the Quartz Crystal Thickness Sensor, of 1.1 Å/s. The sputtered thickness of the gold was estimated according to the deposition rate and the deposition time. After sputtering the vinyl mask was removed manually using tweezers. Gold coated shrink film devices were shrunk on aluminum boats at 130 and 160°C in an Isotemp Vacuum oven (Fisher Scientific, Ottawa, Ontario). Self-adhesive vinyl masks were used to expose a small region of the devices used for electrochemical characterization.

### 3.3.3 SEM Characterization

SEM images of the gold films before and after shrinking were obtained using a JEOL JSM-7000S Scanning Electron Microscope with an accelerating voltage of 3 kV, working distance of 6 mm, and low probe current.

### 3.3.4 Surface Roughness Characterization

The roughness of shrunken device surfaces was measured for gold coating thicknesses of 0, 20, 50, 100 and 200 nm using a Zygo NewView 5000 white light interferometer (Zygo Corporation, Middlefield, CT). The root mean square (RMS) and peak-to-valley (PV) values were obtained in 3-5 device areas and compared across devices. Measurements were taken with 10x and 50x interferometric objectives and both were with a 2×image zoom setting, which resulted in fields of view of 360×270 μm and 70×50 μm, respectively. Data was collected from a CCD camera with an imaging pixel size of 11.2 μm. The built in software, MetroPro, was used for data analysis. A Fast Fourier Transform (FFT) band pass filter was applied, using cutoff frequencies of 183.35 and 558.79 $mm^{-1}$. Spikes with height values above 10*RMS were removed from the analysis of the imaged area to eliminate any contribution from contaminants (dust particles or defects on the films) to the roughness values.

### 3.3.5 Electrochemical Characterization

Cyclic voltammetry was performed using a CHI 660D Electrochemical Workstation (CH Instrument, Austin, Texas) and a standard three-electrode set-up. The electrochemical system consisted of an Ag/AgCl reference electrode, a platinum wire counter electrode, and gold sputtered on polystyrene as the working electrode. To ensure that the planar geometric surface area of the working electrode was the same for samples before and after shrinking (0.25 cm$^2$), a vinyl mask was placed over the gold with a single 0.5 cm by 0.5 cm square cut out to expose the electrochemically active surface. To determine the electrochemically active surface area of the samples, a solution of 0.1 M $H_2SO_4$ was used to perform 10 cyclic voltammetry scans at a scan rate of 0.05 V s$^{-1}$ and a voltage range between 0 and 1.5 V. The reduction sections of the resulting cyclic voltammograms were integrated using OriginPro 8 software to determine the charge and the electrochemically active surface area was calculated (Surface area = charge/surface charge density) using the surface charge density of a monolayer of gold, 386 μC cm$^{-2}$. To test the ability to conduct electrochemical measurements, a solution of 2 mM $K_4Fe(CN)_6$ in 0.1 M KCl was used to cycle between -0.1 and 0.5 V at the following scan rates: 0.01, 0.02, 0.04, and 0.08 V s$^{-1}$. Also, chronoamperometry was performed using solutions ranging from 50 μM to 100 mM $K_4Fe(CN)_6$ in 1 M KCl at a potential of 0.5V for 1 second.

### 3.3.6 Electrical Characterization

Sheet resistance($R_s$) measurements were taken using the HL5500PC- Hall Effect Measurement System with HL5500 Buffer Amplifier (Nanometrics, Milpitas, California).

Four gold probe tips were used to take $R_s$ measurements of the samples in a standard van der Pauw configuration. The sheet resistance was calculated according to

$$R_s = \frac{2.2662(V_{43}+V_{23})}{I} \times F \times Q \qquad (1)$$

where $I$ is the applied current, $V_{43}$ and $V_{23}$ are the potentials measured perpendicular to each other on the film in response to the current, $Q$ is the symmetry factor and is calculated by $Q = \frac{V_{43}}{V_{23}}$, and $F$ is a correction factor for any asymmetry and is calculated by: $F = 1 - 0.34657A - 0.09236A^2$, where $A = \left[\frac{Q-1}{Q+1}\right]^2$. In order to cancel thermoelectric and other effects, the currents were applied in both directions between two tips, and then the measured potentials were averaged.

### 3.3.7 Electrodeposition

The CHI 660D Electrochemical Workstation (CH Instrument, Austin, Texas) was used for electrodeposition with the standard three-electrode set-up described above. To ensure the planar geometric surface area of the working electrode was the same for samples before and after shrinking (0.25 cm$^2$), a vinyl mask was placed over the gold with a single 0.5 cm by 0.5 cm square cut out to expose the electrochemically active surface. Gold nanostructures were grown by electrodeposition on the gold-polystyrene substrate using solutions containing 5 and 10 mM $HAuCl_4$ in 0.5 M HCl at potentials of -0.2 or -0.3 V for 900 seconds.

## 3.4 Results and Discussion

### 3.4.1 Quick Prototyping of Patterned Electrodes

Bench top fabrication techniques offer capabilities to prototype devices in a quick, facile and cost-effective manner. In particular, the ability to rapidly fabricate and test electrodes in a variety of configurations, shapes, and sizes ranging from the millimeter to the micrometer scale, could prove valuable in the development of new sensing electrode architectures for functional devices. To produce patterned electrodes with designed shapes and sizes, we have combined two bench top fabrication techniques: vinyl film masking and pre-stressed polystyrene (PS) sheet shrinking. The fabrication steps followed to produce patterned thin gold electrodes using the vinyl masking and PS shrinking approach are depicted in Figure 3.1a. Self-adhesive vinyl film was employed as a masking material not only because of its ease of use, ability to bind to a wide range of materials, ease of removal without leaving adhesive residue behind, and adequate resistance to solvents and mild acidic conditions, but also because it can be effectively patterned using a bench top craft cutter. To produce the pattern masks, self-adhesive vinyl films (red film, Figure 3.1a) were bound to clean PS sheets (black sheet, Figure 3.1a) and flattened using a roller. Patterns designed in a CAD program were then scored into the vinyl film bound to the PS sheets using a craft cutter. The optimization of the force, speed and acceleration with which the blade cut into the vinyl film allowed us to obtain parallel line cuts with spacings as small as 100 μm (limited by the step size of the cutter motor) and circular features with diameters as small as 200 μm (limited by the turning radius of the blade). The optimized parameters also ensured that the blade did not cut into the underlying PS sheet, which would introduce undesired topography in the final electrodes. The cut out vinyl was peeled-off using rounded tip tweezers to avoid scratching the underlying PS surface. Peeling the vinyl with a uniform force applied parallel to the thinnest features prevented tearing of the vinyl and ensured that it was removed as a continuous film. Once the desired pattern was exposed, a thin gold coating of controlled thickness (20-200 nm) was sputtered onto the devices. Finally, the remaining vinyl mask was lifted-off to reveal a patterned electrode on the PS sheet (Figure 3.1a). Occasional tearing, similar to that obtained in resist lift-off processes, could be observed after the vinyl lift-off in SEM images taken from the edges of thick gold films (Supplemental Figure 3.1). This patterning approach allowed us to quickly produce electrodes with various shapes and sizes (Figure 3.1b) and with different film thicknesses (Figure 3.1c). Although for this study we report on the patterning of gold films, the same approach can be used to produce patterns of a number of different conductive, semiconductive and insulating thin films.

The size of the gold patterns was reduced through biaxial shrinking of the PS substrate to generate electrodes with features as small as 80 micrometers. When heated above their glass transition temperature of 100°C,[155] pre-stressed PS sheets have the ability to shrink to under 50% of their original size due to polymer chain relaxation. We have taken advantage of this effect to reduce the dimensions of the features on our patterned gold films. PS sheets containing patterned gold films of thicknesses ranging from 20 to 200 nanometers were heated at 130 and 160°C and their shrinking behaviors were characterized. The higher temperature shrunk the devices significantly faster (full shrinking achieved within 2 minutes) than the lower one (full shrinking achieved within 10 minutes).

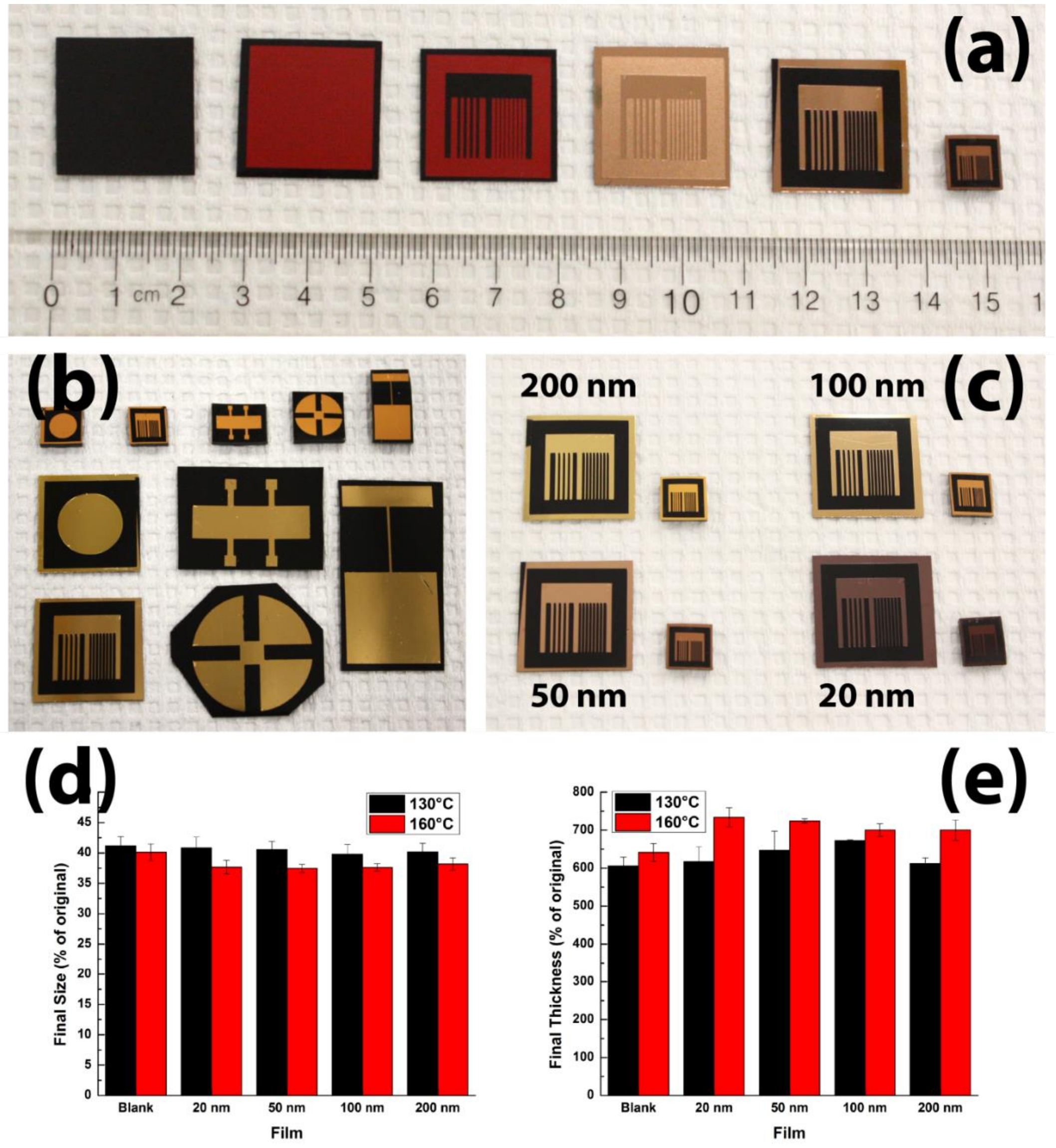

Figure 3.1 Bench top fabrication techniques can be used to produce patterned electrodes with critical dimensions < 100 µm. (a) Depiction of the fabrication of patterned electrodes through vinyl masking and pre-stressed PS substrate shrinking. (b) The bench top approach developed allows the fabrication of patterned electrodes with a wide variety of geometrical shapes. (c) Patterned electrodes were fabricated from a variety of gold film thicknesses. Shrinking of the patterned electrodes at 130 and 160°C was highly reproducible, with (d) final transverse dimensions ~40% of the original size and (e) axial dimensions ~650% of the original size.

It was observed that at both temperatures the shrunken PS sheets and the patterned gold films retained their original overall shape and that shrinking was highly reproducible (Figure 3.1c). However, slight differences were noted between the devices shrunken at the two temperatures. It was noted that devices shrunk at 160°C reached transverse dimensions that were ~38% of the original size, while those shrunk at 130°C only reached ~40% (Figure 3.1d). Conversely, the devices shrunk at 160°C reached ~700% of their original thickness, while those shrunk at 130°C reached only ~650% of their original value (Figure 3.1e). These small differences are most likely due to the higher fluidity of the PS chains at higher temperatures, as well as the more rapid relaxation of the strain in the pre-stressed film during the shrinking process. Finally, it was also observed that the shrinking process induced the gold films to become more firmly attached to the PS substrates, as shrunken films could not be removed from the surface by the scotch tape peeling test (5 successive peels), but they could be partially removed in unshrunken devices. The increase in adhesive strength has been previously observed[128] and is attributed to the fact that at elevated temperatures the shrinking PS surface becomes soft enough to integrate with the metallic film. Thus, the combination of patterning gold films through vinyl masking and shrinking of the underlying PS substrates has enabled us to quickly produce robust gold electrodes with critical dimensions as small as 80 micrometers in a reproducible fashion.

### 3.4.2 Stress-Driven Micro- and Nanostructuring of Gold Electrodes

In addition to the size-reducing effect, shrinking of the PS substrate induced micro and nanostructuring of the gold film surface. Upon shrinking the patterned gold films, a slight color change appeared and the film became more opaque (Figure 3.1b-c). Closer inspection revealed that the shrinking process induced texturing on the films, which changed the reflective and scattering properties of the surface, leading to the observed color change. As the PS sheet shrunk, compressive stress was exerted on the pliable gold film and the difference in stiffness between the two materials caused the film to buckle, producing wrinkles ranging from the nanometer to the micrometer scale (Figure 3.2). This effect has been exploited in the past to produce wrinkles in metallic films on polydimethylsiloxane (PDMS),[156], [157] on poly-ethylene sheets,[23] and on thin[158]–[160] and bulk[128], [139] PS substrates. The wrinkling phenomenon has been modeled[119], [161] for low shrinking ratios or low compressive stresses and the wavelength of the wrinkles has been estimated to scale as the cubic root of the ratio of the elastic moduli of the thin film and the PS substrate multiplied by the film thickness.[127] SEM micrographs of our patterned gold films after shrinking confirmed that the wrinkle size depended strongly on the film thickness, with smaller wrinkles forming on thinner films (Figure 3.2a). We observed wrinkled structures that went from the nanometer, for 20 nm thick films, to the micrometer range, for 200 nm thick films. The wrinkles appeared continuous when imaged through electron microscopy, which implied that the patterned gold film was intact. Furthermore, the wrinkles obtained at the large compressive stresses or shrinking ratios obtained from the pre-stressed PS sheets did not appear as regular or ordered as those previously observed from the films undergoing the initial stages of wrinkling instability.[157], [158], [160] The topologies obtained here had tall hills and deep valleys, which appeared as a result of additional crumpling on top of a first set of wrinkles.

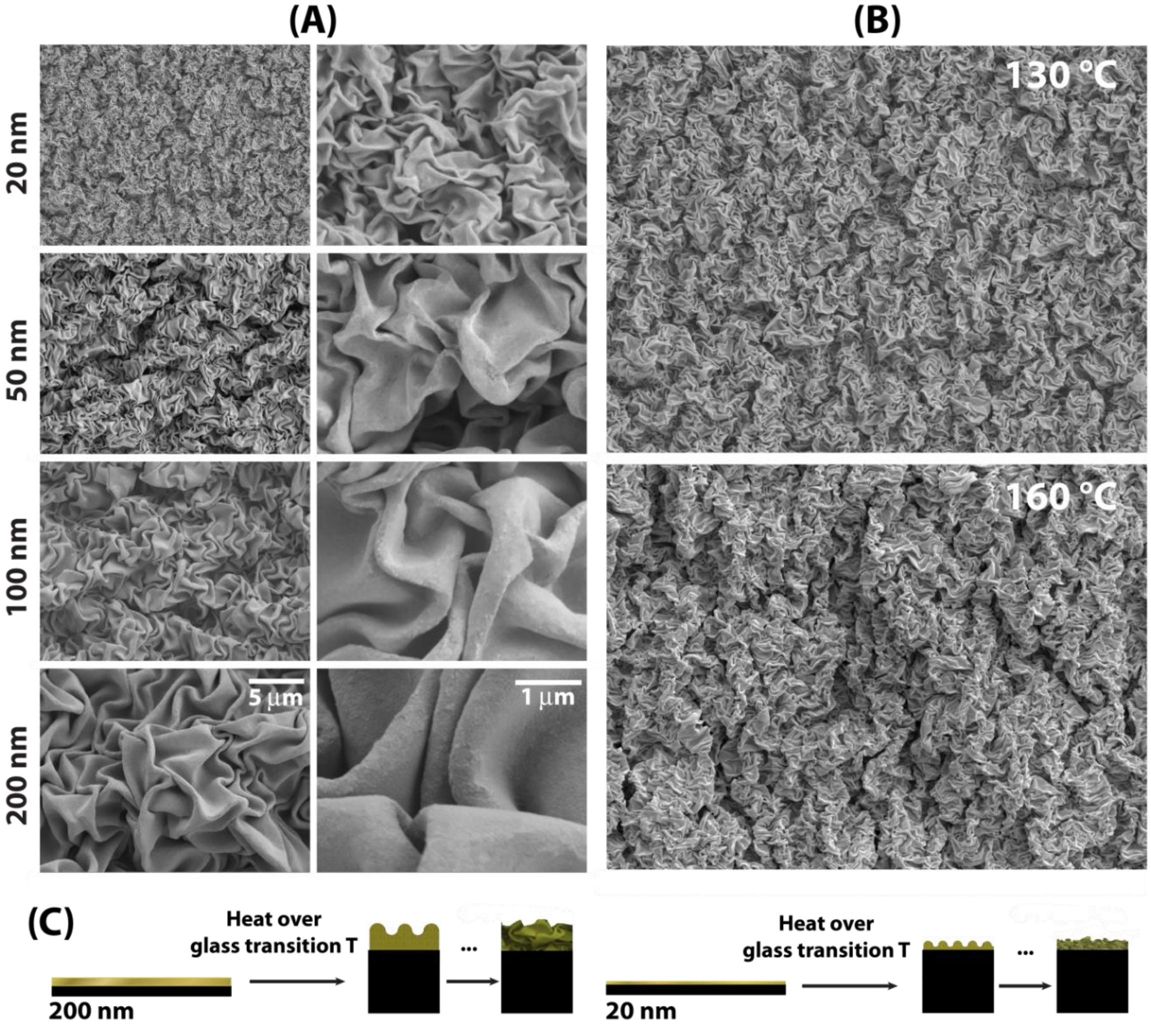

Figure 3.2 Shrinking of the polystyrene substrate causes an adhered gold film to buckle and wrinkle. (a) The size of the resulting wrinkles depends strongly on the film thickness, with thin films resulting in nanoscale wrinkles and thick films resulting in microscale wrinkles. (b) The shrinking temperature also affects the wrinkling process, with higher temperatures producing rougher surfaces. (c) Schematic depiction of the stress-driven wrinkling of gold films.

A comparison between substrates shrunk at 160 versus 130°C revealed that the former appeared to have rougher surfaces (Figure 3.2b). Although the structures observed cannot be modeled by current theoretical descriptions, it is evident that the compressive shrinking rate plays an important role in the second hierarchy of wrinkles. Thus, by controlling the film thickness of the patterned electrodes and the shrinking temperature, structured metallic surfaces with topographical structures that span from the nanometer to the micrometer range were created.

The surfaces of the crumple-structured gold films were characterized through white light interferometry to assess their roughness. Interferometry is a powerful technique that allows the measurement of surface height differences based on fringes, which arise from the interference between a reference and a measuring light beam. The pixel size of the interferometer camera used to image the surfaces was equivalent to 112 nm, which meant that the best lateral resolution that could be achieved was ~200 nm. While this prevented measuring the nanoscale structure of the thinnest wrinkled films with the same resolution as that of the electron microscope, our measurements revealed significant trends. Interferometry images showed that all crumple-structured films had similar overall surface features with islands of high elevations surrounded by valleys of lower height (Figure 3.3a-b). Although the surface structures looked similar, their heights were significantly different. As figures of merit we chose to characterize the surfaces using their root mean square (RMS) roughness, which indicates the average deviation from the baseline, and the peak-valley spread (PV), which is calculated as the height difference between the highest and the lowest points and reports on the range of height measurements.

All the crumple-structured gold surfaces exhibited RMS surface roughness values that were higher than that of the shrunken PS sheet alone (19 and 23 nm for sheets shrunken at 130 and 160°C). The RMS roughness for crumple-structured films ranged from 250 nm for 20 nm thick films shrunken at 130°C, to 1200 nm for 200 nm thick films shrunken at 160° (Figure 3.3c). The increase in surface roughness was directly correlated with increasing film thickness. This is to be expected, as the thicker films are less pliable and do not buckle as easily during the shrinking step. In addition, we observed that the surface roughness was significantly higher for films shrunken at 160°C as compared with those shrunken at 130°C. These differences confirm our observations from SEM images, where the films shrunken at the higher temperature seemed to have deeper valleys and higher peaks. The PV values for crumple-structured films ranged from ~2 μm, for 20 nm films shrunken at 130°C, to ~12 μm, for 200 nm films shrunken at 160°C, and were also significantly higher than those for shrunken PS sheets alone (ca. 450 nm for films shrunken at both temperatures). The PV followed a similar trend to that observed for the RMS roughness, with increasing PV values for increasing films thickness and higher PV values for films shrunken at 160°C (Figure 3.3d). The characterization of the crumple-structured thin films through interferometry demonstrates that the gold electrodes fabricated through vinyl masking and PS sheet shrinking have surfaces that are significantly roughened, and that this surface roughness can be controlled by the choice of film thickness and shrinking temperature.

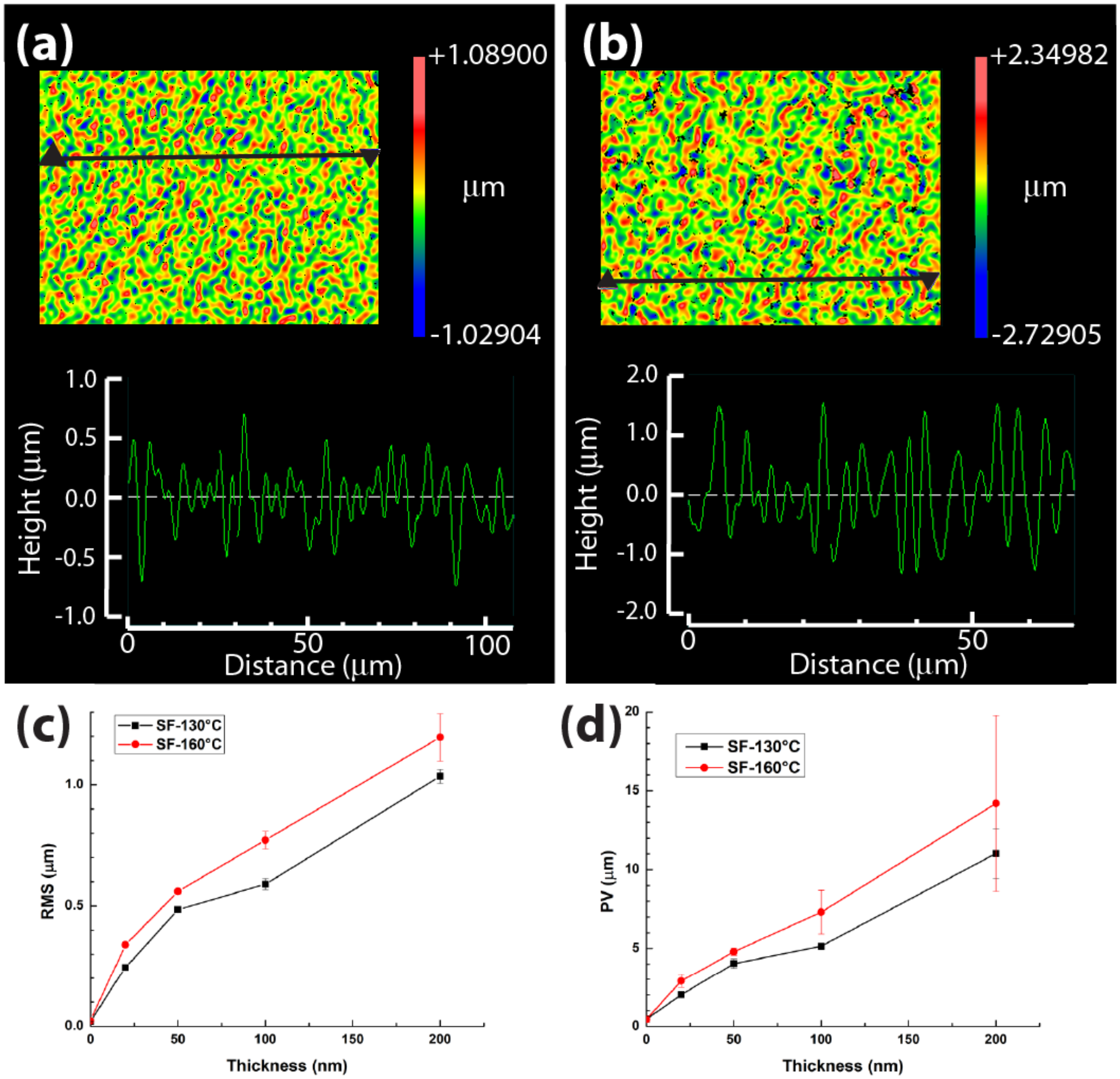

Figure 3.3 White light interferometry was used to characterize the surface roughness of crumple-structured gold films. (a) Sample interferometry image and line profile for a 20 nm thick crumpled film. (b) Sample interferometry image and line profile for a 100 nm thick crumpled film. Comparison of (c) RMS roughness and (d) PV spread for crumple-structured films fabricated at 130 and 160°C. Error bars represent the standard deviation of replicate measurements performed on the structured films (n > 3).

The increased surface roughness of the micro- and nanostructured films also influenced their wettability. To characterize the wettability of the patterned gold films we measured the contact angles of water droplets on the films before and after shrinking of the underlying PS substrate (Supplemental Figure 3.2). The contact angle of unshrunken gold films of all thicknesses was statistically equal with a value ~65°, and close to that of unshrunken PS film, which was 70°. Upon shrinking, all the micro- and nanostructured films had increased contact angles, ranging from 104° for 20 nm thick shrunken films, and increasing with thickness to a plateau value close to 120° for 100 and 200 nm thick films. In comparison, the contact angle for the shrunken PS sheets was ~90°. The increase in contact angle is a direct result of the structured surface and can be understood in terms of the crevices and clefts that are inaccessible to water, resulting in a Cassie or mixed Cassie-Wenzel wetting pattern.[162] These results show that the wettability of gold electrodes can be tailored by controlling the size of the structures induced by the shrinking of the underlying PS substrate. The ability to tailor the wettability of thin film surfaces has attracted much attention, as it can lead to applications such as self-cleaning coatings. The ease with which these structured surfaces are fabricated makes them attractive for the development of multiplexed biosensors and microfluidic devices that exploit the hydrophobic nature of the structured films to integrate multiple samples on a single substrate.

### 3.4.3 Electrochemical Characterization of Electrodes Patterned on PS Sheets

Electrical and electronic devices created on polymeric substrates hold great potential in next generation display,[163] chemical and biological sensing,[164] and photovoltaic[165] technologies because their mechanical flexibility and light weight is complemented with rapid and cost-effective manufacturing. In addition, reproducibility in conductivity, electron transfer kinetics, surface area, and electrochemical activity are essential to material systems used in electrochemical sensing. To assess the suitability of metallic films patterned on PS sheets as functional electrodes, we used cyclic voltammetry (CV) to compare the electrochemical behavior of two sets of devices: patterned electrodes on glass substrates and patterned electrodes on unshrunken PS sheets (Supplemental Figure 3.3). Self-adhesive vinyl masks with a square cutout were immobilized on the devices to ensure that the electrodes fabricated on glass and PS substrates exposed the same geometric gold surface area (Supplemental Figure 3.3a). CV curves of unshrunken PS devices measured in sulfuric acid solutions displayed a well-defined redox signature associated with the oxidation of gold and the subsequent reduction of gold oxide, which compared favorably to the voltammograms obtained from electrodes fabricated on glass (Supplemental Figure 3.3b). It was observed that the unshrunken PS devices exhibited a slightly lower electroactive surface area than their glass counterparts exposing the same geometric area, as estimated from the integrated charge contained in the reduction peak of CV scans acquired in $H_2SO_4$ solutions. We attribute the reduced electroactive surface area to irregularities on the PS substrate surface, which is rougher than the flat polished glass, and to the fabrication conditions where the sputtering of the gold film onto the PS substrates heats the polymer enough that it can partially mix with the metal being deposited. CV curves from PS devices were also obtained in solutions containing the redox complex potassium ferrocyanide. The CV curves from unshrunken PS devices exhibited well-defined oxidation and reduction peaks associated with the redox couple ferrocyanide/ferricyanide, which also compared favorably to the voltammograms obtained from devices fabricated on glass (Supplemental Figure 3.3c). Analysis of the CV curve characteristics showed that PS devices exhibit redox potentials and peak shapes that closely match those of glass devices and do not display any undesired background electrochemical activity. In addition, PS devices demonstrated exceptional device-to-device reproducibility as the variations in peak potentials and peak currents observed were less than 1% and 8% respectively (Supplemental Figure 3.3d). Altogether these experiments show that devices fabricated on PS substrates exhibit electrochemical behavior that closely resembles that of devices fabricated on glass, making them suitable for electrochemical device fabrication.

### 3.4.4 Electrical and Electrochemical Properties of Crumple-Structured Electrodes (CSEs)

Tunable high surface area inorganic materials are important to many scientific and industrial applications including catalysis, sensing, separations, and energy storage.[166], [167] The ability to fabricate micro- and nanostructured surfaces through bench top techniques is an attractive route for the rapid development of high surface area electrodes with tunable characteristics. To demonstrate the suitability of CSEs fabricated through bench top techniques as functional, high surface area electrodes, we conducted a series of measurements of their electrical and electrochemical properties. The continuity and integrity of CSE devices were first evaluated by measuring the sheet resistance of the patterned gold films through the van der Pauw method.[168] The sheet resistance measured for PS devices before shrinking showed decreasing values for increasing gold film thicknesses, with the sheet resistance values tending towards an asymptotic value of 0.28

ohms/square (Supplemental Figure 3.4). The sheet resistance for the PS devices after shrinking exhibited a similar trend, with CSEs made from thinner films showing higher sheet resistance than those made with thicker films (Supplemental Figure 3.4). In addition, shrunken devices displayed a significantly lower sheet resistance than their unshrunken counterparts. We hypothesize that the decrease in sheet resistance in CSEs arises from the contact between adjacent creases and folds present on the wrinkled films, which yields a shorter path length for current to travel through and results in a lower effective sheet resistance. The observation that the decrease in sheet resistance after shrinking is more significant for thinner films supports this hypothesis, since SEM images (Figure 3.2) show that wrinkles are more closely packed in thinner films and have a higher probability of contacting adjacent structures. The ability to successfully and reproducibly measure sheet resistance values from devices fabricated on PS substrates demonstrates that the gold films before and after shrinking are continuous and suitable for electrical measurements.

An attractive feature of the wrinkled topography of CSEs is that these devices could present significantly larger active surfaces per projected geometrical area than flat electrodes. To measure the active surface area of CSEs, we quantified the total charge involved in the electrochemical formation of a monolayer of gold oxide (Figure 3.4a). The active areas of PS devices fabricated with different film thicknesses were compared before and after shrinking at temperatures of 130 and 160°C (Figure 3.4a-b). All unshrunken devices, regardless of film thickness, showed the same electroactive surface area, which was expected as no surface structuring is present and all devices present the same geometrical area. On the other hand, all shrunken devices exhibited significantly larger electroactive surface areas, with enhancements as high as 665% of the area presented by unshrunken devices. This result is readily explained, as the shrinking process crumples the original film into a geometrical area that is ~16% of that of the original device. Figure 4b also shows that the measured electroactive surface area enhancement for shrunken devices is larger for thicker than for thinner film devices processed using identical methods. This supports our hypothesis that coalescence of adjacent wrinkles is more frequent in CSEs fabricated out of thinner films where the wrinkles are more closely packed. Additionally, we observed that the temperature at which the devices were shrunk could influence the resulting electroactive surface area. Figure 3.4b shows that shrinking of 20 nm thick devices at 160°C yielded lower enhancements than shrinking at 130°C, while the enhancement was not statistically different for all other film thicknesses. This observation can be explained by the faster shrinking kinetics at higher temperature, which results in secondary wrinkles (seen in Figure 3.2) that leave some of the primary wrinkles inaccessible to the oxidation process. This effect is more pronounced in thin film devices because the wrinkles formed are more closely packed, and are more easily shielded by secondary wrinkling than in thicker film devices. The results from the characterization of the electroactive surface area of CSEs demonstrate that the shrinking process is a facile method to create high surface area electrodes where the surface area enhancement can be tuned through experimental parameters such as film thickness and shrinking temperature.

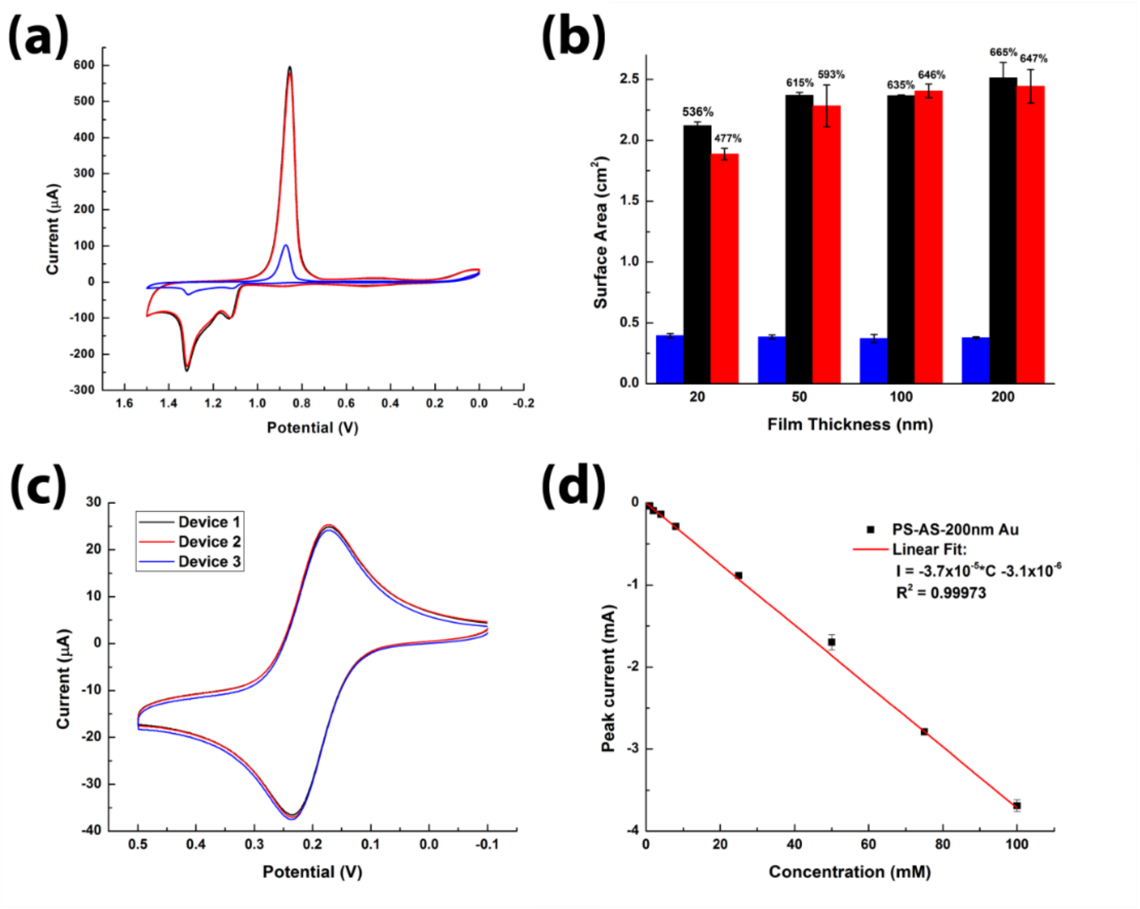

Figure 3.4 Crumple-structured electrodes are suitable devices for electrochemical measurements. (a) A comparison of cyclic voltammograms obtained in dilute acid solutions for electrodes before (blue line) and after shrinking at 130 (black line) and 160°C (red line). (b) Quantification of the charge transferred during the formation of a monolayer of gold oxide reveals significant enhancement of electroactive surface area after shrinking at 130 (black) and 160°C (red), as compared to that of the unshrunken electrodes (blue). (c) Cyclic voltammograms obtained from three different 200 nm CSE devices immersed into a potassium ferrocyanide solution demonstrate the high device-to-device reproducibility. (d) Chronoamperometric measurements performed with 200 nm CSEs immersed into solutions containing various concentrations of potassium ferrocyanide demonstrate exceptional linearity in sensing the redox complex.

To investigate the possibility of using high surface area CSEs in electrical and electrochemical devices, we assessed their performance and device-to-device reproducibility in electrochemical measurements. CV measurements were conducted with 200 nm thick CSE devices immersed in a 2 mM solution of potassium ferrocyanide. The CV curves generated form these devices showed peak oxidation/reduction currents and reduction/oxidation potentials (Figure 3.4c) that compared favorably with those measured from devices fabricated on glass and unshrunken PS substrates (Supplemental Figure 3c-d). Furthermore, the CV for three CSE devices tested displayed close to identical curves, with variations in peak redox currents and potentials that were < 1%. Thus, CSEs are suitable for electrochemical measurements and display an extraordinary device-to-device reproducibility, which translates in highly reliable electrodes for electrochemical device applications. Because electrochemical sensing relies on the accurate and quantifiable detection of redox analytes, we further tested the suitability of CSEs fabricated from 200 nm thick films as electrochemical amperometric sensors. The CSEs were used as working electrodes in a three-electrode electrochemical cell and were used to detect increasing concentrations of potassium ferrocyanide. Chrono-amperometric measurements were used to characterize the electrodes' response to the analyte concentration in solution. Figure 4d shows that the peak current response is linear and highly reproducible for potassium ferrocyanide concentrations in the 50 µM to 100 mM range, which is in accordance with the Cottrell equation for changes in current due to the diffusion limited oxidation of the target analyte. These electrochemical measurements show that CSEs are suitable for the fabrication of electrochemical devices because they exhibit properties that mimic those of electrodes fabricated on traditional substrates, high device-to-device reproducibility, and linearity in sensing of electroactive species. CSEs could thus present an attractive alternative for the fabrication of highly sensitive electrochemical sensing devices with applications ranging from toxic gas to biomolecular detection.

### 3.4.5 Hierarchical Nanostructuring of CSEs through Electrodeposition

Three-dimensional nanostructured electrodes with features in the 10-50 nm range have demonstrated superior sensitivity in detection of biomolecular analytes (*e.g.* nucleic acids and proteins) than materials comprised of larger grains.[31] In an attempt to develop electrodes suitable for biosensing applications, we sought to bring another level of hierarchical structuring to CSEs through electrodeposition. To this end, gold was electrodeposited from a solution containing $HAuCl_4$ and HCl onto flat electrodes and CSE devices fabricated out of 50 nm thick gold films. Our hypothesis was that the folds and creases present on the CSEs would present regions of local electric field enhancement where electrodeposition would occur preferentially. The resulting nanostructures would increase the electrode surface area, making CSEs even more sensitive and suitable for biosensing applications.

Systematic sampling of the electrodeposition parameter space, allowed the controlled formation of sub-50 nm structures on patterned electrode surfaces. Electrodeposition tests were performed on unshrunken devices to compare the effect of variations in the applied potential and in the concentration of $HAuCl_4$ on the shape and size of the electrodeposited gold structures. SEM images of electrodeposition on flat, unshrunken electrodes (Figure 3.5a) show that as the cathodic potential is decreased from -0.2 to -0.3 V, the resulting electrodeposited gold structures shift from hemispherical and cylindrical grains to two-dimensional leaf-like structures, where the leaf's plane lies perpendicular to the electrode. This difference in grain morphology can be explained as a shift from kinetically-controlled to diffusion-controlled electrodeposition. Previously, the electrodeposition of gold has been categorized as: kinetically controlled at small nucleation overpotentials, mixed kinetically/diffusion controlled at moderate nucleation overpotentials, and diffusion controlled at large nucleation overpotentials.[169] Images of electrodes where the deposition was performed at -0.2 V show hemispherical structures, which are indicative of the radial transport of metal ions associated with mixed kinetically-diffusion controlled electrodeposition. On the other hand, for samples where electrodeposition was performed at -0.3 V the faster reaction kinetics shifted the deposition towards a diffusion-limited regime, where growth instabilities resulted in the formation of irregularly shaped vertical dendrites that coalesced into leaf-like structures as they grew. Furthermore, increasing the concentration of $HAuCl_4$ translated into an increased deposition rate (Supplemental Figure 3.5), which increased the size of the structures. However, changing the $HAuCl_4$ concentration did not affect the morphology of the deposited structures.

Having established specific electrodeposition parameters for precisely tuning the size and morphology of the deposited structures on flat electrodes, we proceeded to use these conditions to integrate nanostructured morphologies onto CSE devices fabricated from 50 nm thick gold films.

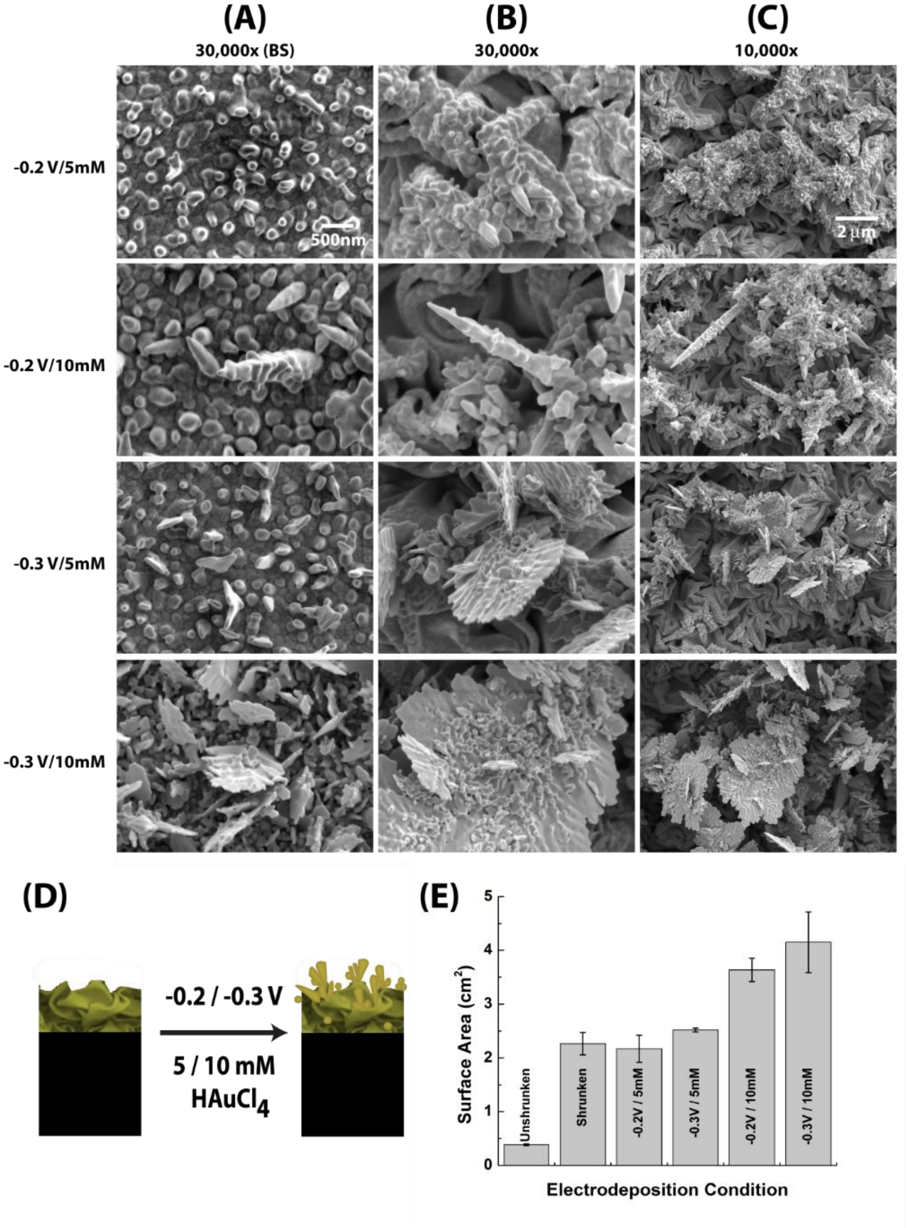

Figure 3.5 Electrodeposition of gold nanostructures enhances the electroactive surface area of CSEs. A comparison of Scanning Electron Microscopy images of the nanostructures formed through electrodeposition on unshrunken flat (a) and shrunken electrodes (b-c) shows that CSEs enhance the electrodeposition process. The deposition potential and metallic salt concentration control the morphology and size of the deposited nanostructures. (d) Schematic depiction of the electrodeposition process on CSEs. (e) The comparison of the electroactive surface area for unshrunken, shrunken, and electrodeposited devices shows that through shrinking and electrodeposition, surface area enhancements of up to 1000% of the flat electrode can be achieved.

To understand the role of the micro/nanostructuring of the CSE materials on the morphology of the electrodeposited gold structures, we compared the SEM images obtained from electrodeposition experiments on un-shrunken and shrunken substrates (Figures 3.5a-c). Analysis of high magnification images (Figure 3,.5b) showed that deposition on CSE devices yielded structures with similar morphology to those deposited on their unshrunken counterparts. However, the structures formed on CSE devices were significantly larger than structures formed on flat substrates under similar electrodeposition conditions. This indicates that although deposition on CSE devices does not change the electrodeposition regime, it influences the growth kinetics of the deposited structures. Local electric field enhancement[170] along with increased heterogeneous electron transfer kinetics[171], [172] have been previously observed on nanostructured metallic films and are likely responsible for the enhanced deposition rate on CSE devices. The analysis of low-magnification SEM images showed that the deposition of nanostructures on CSE devices was not as homogeneous as the deposition on unshrunken devices. Under all deposition conditions, CSE substrates exhibited regions of nanostructure formation alternating with regions where no significant deposition occurred. The reasons for these differences are unclear, but might be related to the existence of regions that are inaccessible due to poor wetting of the surface by the electrolyte solution.

Nanostructures formed through electrodeposition on the electrode surfaces increased the electroactive surface area of CSE devices. This process is schematically depicted in Figure 3.5d. To quantify the change in surface area induced by the electrodeposited structures, we measured the charge transferred by the electrochemical formation of a monolayer of gold oxide on the modified electrodes. Figure 3.5e summarizes the measured electroactive surface area for devices where electrodeposition was performed under the four conditions pictured in Figures 3.5a-c. Significant surface area enhancement was only observed for conditions where large structures were formed, namely electrodeposition experiments conducted at 10 mM $HAuCl_4$. The largest enhancement was observed for devices where electrodeposition was performed at -0.3 V and 10 mM $HAuCl_4$, where the final electroactive surface area was ~200% of the surface corresponding to the bare shrunken device and ~1000% of the unshrunken device. The results presented demonstrate that it is possible to increase the electroactive surface area of CSE devices by the controlled growth of nanostructures with different morphologies through electrodeposition.

### 3.5 Conclusions

A rapid, facile and inexpensive bench top approach has been developed for fabricating electrodes with hierarchical structures spanning from the millimeter to the nanometer range. The use of self-adhesive vinyl as masking material and a craft cutter allowed prototyping of electrodes with critical dimensions in the sub-millimeter range in timeframes of minutes to hours. Furthermore, the use of a PS shrinkable substrate allowed the reduction of the patterned feature dimensions to sub-100 μm sizes. The shrinking of the PS substrates induced stress-driven wrinkling of the gold films, and it was observed that the size of the topographical features and surface roughness could be tailored from the micrometer to the nanometer scale by adjusting the thickness of the gold film deposited. We characterized the behavior of these crumple-structured electrodes (CSEs) and found that they exhibit electrical and electrochemical properties that compare favorably with electrodes fabricated on traditional substrates, such as glass. We also found that the CSEs exhibited high device-to-device reproducibility and robustness. The most attractive feature of CSEs, however, is that they exhibit significantly enhanced electroactive surface areas per geometric area (665% compared to flat electrodes). Further controllable nanostructuring was produced on CSEs through the tuned electrodeposition of gold nanostructures. We observed that the electrodeposition was improved on CSEs (compared to flat electrodes) due to the field enhancement offered by the structured surface. Devices with electrodeposited nanostructures exhibited further electroactive surface area enhancements (up to 1000% compared to flat electrodes). Thus, we have shown that it is possible to produce hierarchically structured electrodes, with features spanning the sub-millimeter to nanometer scales, through inexpensive, easy to implement and rapid bench top techniques in timeframes less than one hour. We anticipate that such materials will find wide application in the development of highly sensitive point-of-care devices, where high surface area materials can offer enhanced sensitivity and bioprocessing capability towards target analytes.

### 3.6 Acknowledgements

We thank Laura Dodge for help with the measurement of contact angles, and Dr. Maneesh Khanna for help with white light interferometry. This research made use of facilities at the McMaster Manufacturing Research Institute and the Canadian Centre for Electron Microscopy at McMaster. JMM acknowledges funding through the Science and Engineering Research Board at McMaster University.

## 3.7 Chapter 3: Supplementary Information

**Authors:** Christine Gabardo, Yujie Zhu, Leyla Soleymani, and Jose Moran-Mirabal

**Publication:** Advanced Functional Materials, 23, 24, 3030-3039

**Publication Date:** January 2013

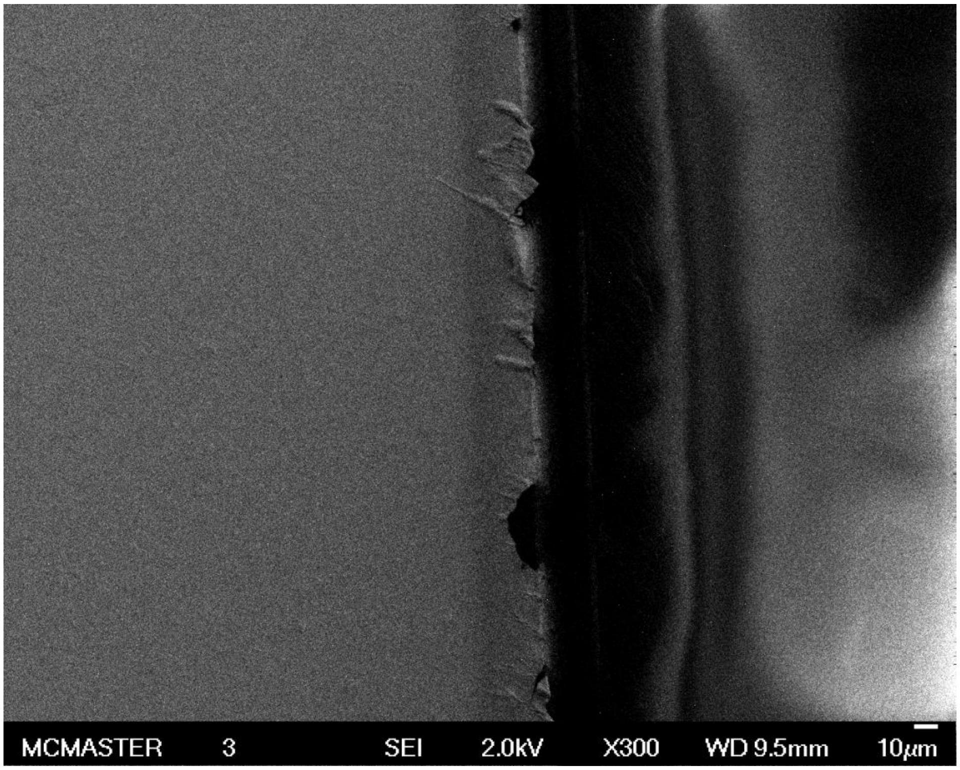

Supplementary Figure 3.1 Scanning electron microscopy image depicting tearing of gold film at pattern edges after vinyl lift-off. Tearing was more evident in thick gold films (100-200 nm).

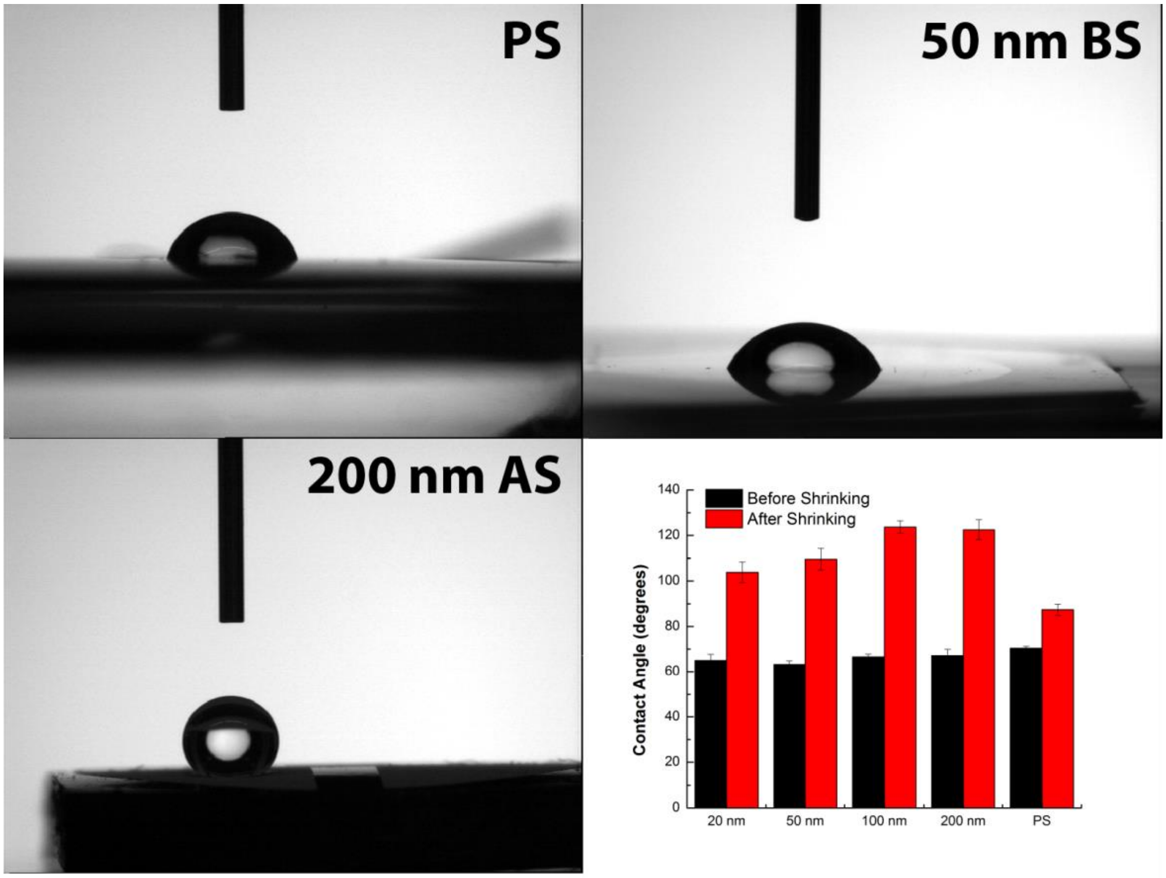

Supplementary Figure 3.2 The contact angle for water droplets placed on the polystyrene (PS) and gold films before (BS) and after shrinking (AS) was measured to assess the change in surface wettability due surface structuring. The contact angles were measured for all gold film thicknesses in four different areas on three different devices. Error bars represent standard deviations of the measurements (n > 36).

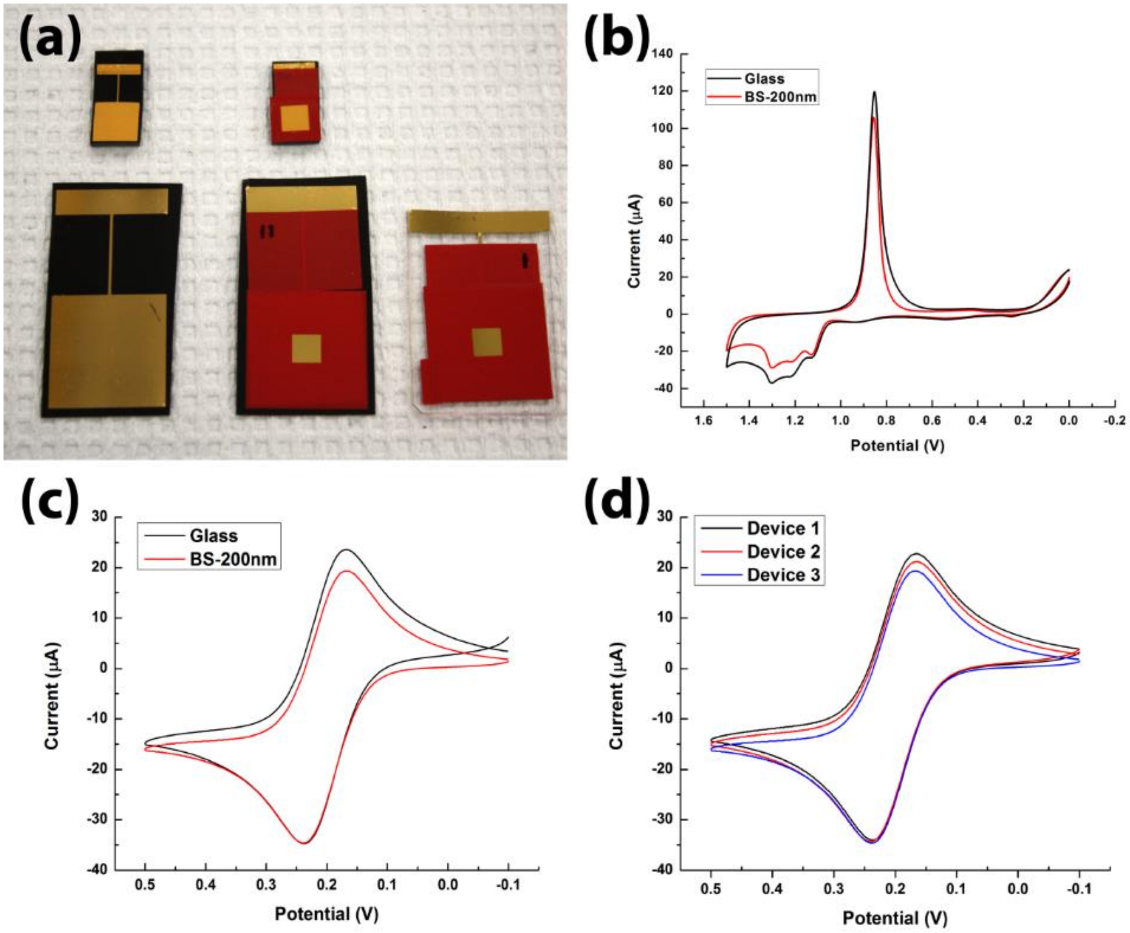

Supplementary Figure 3.3 Comparison of the performance of devices fabricated on polystyrene and glass substrates. (a) Representative devices (and their shrunken counterparts) designed for electrochemical measurements. From left to right: device layout as fabricated on polystyrene substrate, polystyrene device with area masked by self-adhesive vinyl film, glass device with area masked by vinyl film. (b) Comparison of the cyclic voltammograms obtained from glass and unshrunken polystyrene devices (200 nm gold film) immersed in 0.1 M $H_2SO_4$. (c) Comparison of the cyclic voltammograms obtained from glass and unshrunken polystyrene devices (200 nm gold film) immersed in 0.1 M KCl solution containing 2 mM $K_4Fe(CN)_6$. (d) Comparison of the cyclic voltammograms obtained from three different unshrunken polystyrene devices (200 nm gold film) immersed in 0.1 M KCl solution containing 2 mM $K_4Fe(CN)_6$. The polystyrene devices show high device-to-device reproducibility.

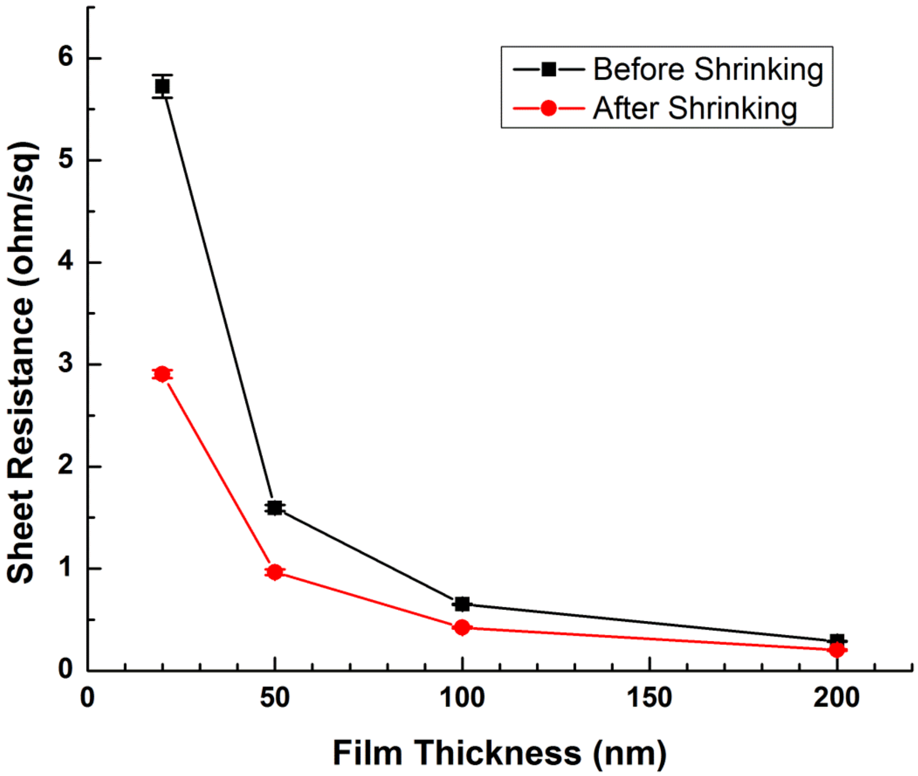

Supplementary Figure 3.4 Sheet resistance measured using the van der Pauw method for devices fabricated on polystyrene substrates before and after shrinking. Film thickness reported is the nominal film thickness measured during gold sputtering. Error bars represent the standard deviation of measurements performed on three different devices (n > 9).

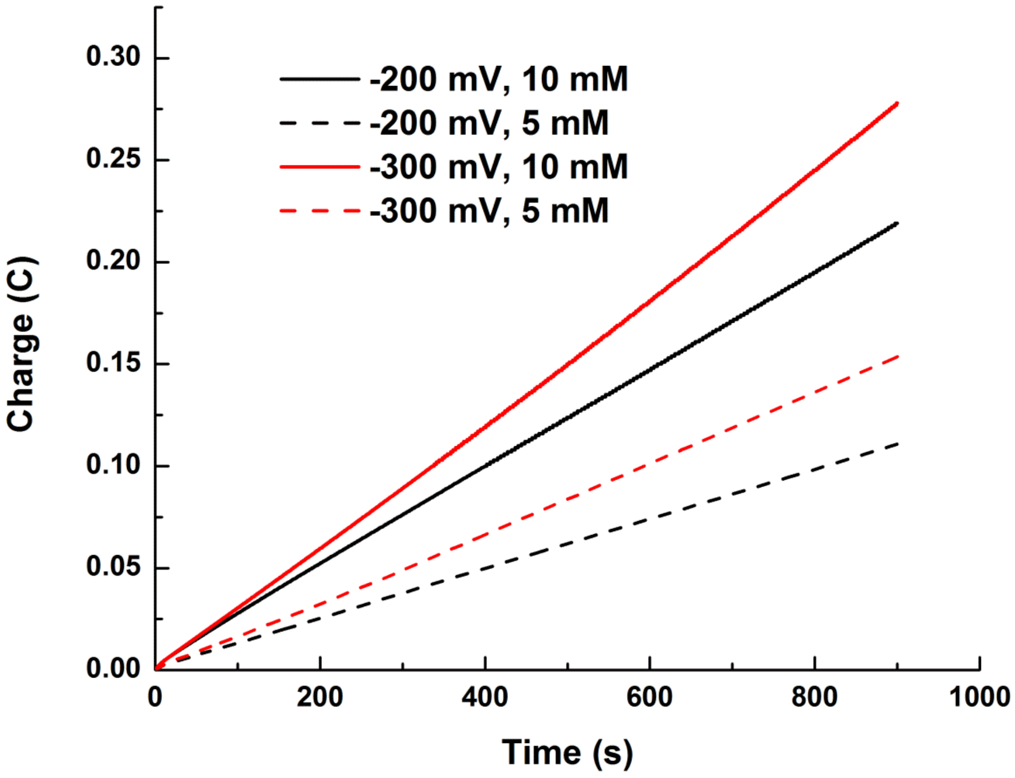

Supplementary Figure 3.5 Effect of change in $HAuCl_4$ concentration on electrodeposition rate at -200 and -300 mV. Increase in charge transfer correlates with faster deposition rate.

# Chapter 4 Rapidly Prototyped Multi-Scale Electrodes to Minimize the Voltage Requirements for Bacterial Cell Lysis

## Chapter Introduction (Objectives C and D)

Cell lysis is an essential sample preparation step for molecular assays that rely on the detection of intracellular contents; however, electrical cell lysis platforms often suffer from high voltage requirements, limiting their use for POC devices. This chapter concentrates on the application of the rapid patterning process, discussed in Chapter 3, to create functional multi-scale electrode devices for LOC applications. Specifically, interdigitated nanostructured microelectrodes were patterned for the LOC bioprocessing application of electrical bacterial cell lysis. An investigation into tuning the structure and function of the electrodes is carried out through scanning electron microscopy imaging and electroactive surface area measurements, and the impact it has on the voltage required to lyse *E.coli* samples is explored in order to minimize the power requirements of the device. Three electrode structures are investigated: flat (planar microelectrodes patterned through standard photolithography), wrinkled (patterned through method described in Chapter 3), and electrodeposited (patterned through method described in Chapter 3 with additional electrodeposited nanostructures). Cell lysis is assessed through different assays (colony formation on plates, membrane permeability with fluorescent dye, and polymerase chain reaction (PCR) for nucleic acid release), and it is determined that the electrode structure has a significant impact on the lysis efficiency of each device. The electrodeposited wrinkled electrodes have the lowest voltage requirements to lyse >95% of the cells at only 4 V. We look to understand the mechanism by which these three-dimensional multi-scale electrodes outperform the wrinkled and flat electrodes through numerical simulations and pH experiments, and determine the mechanism is likely a combination of electroporation and electrochemical lysis.

**Authors:** Christine Gabardo, Aaron Kwong, Leyla Soleymani

**Publication:** Analyst, 140, 5, 1599-1608

**Publication Date:** January 2015

### 4.1 Abstract

Lab-on-a-chip systems used for nucleic acid based detection of bacteria rely on bacterial lysis for the release of cellular material. Although electrical lysis devices can be miniaturized for on-chip integration and reagent-free lysis, they often suffer from high voltage requirements, and rely on the use of off-chip voltage supplies. To overcome this barrier, we developed a rapid prototyping method for creating multi-scale electrodes that are structurally tuned for lowering the voltage needed for electrical bacterial lysis. These three-dimensional multi-scale electrodes – with micron scale reaction areas and nanoscale features – are fabricated using benchtop methods including craft cutting, polymer-induced wrinkling, and electrodeposition, which enable a lysis device to be designed, fabricated, and optimized in a matter of hours. These tunable electrodes show superior behaviour compared to lithographically-prepared electrodes in terms of lysis efficiency and voltage requirement. Successful extraction of nucleic acids from bacterial samples processed by

these electrodes demonstrate the potential for these rapidly prototyped devices to be integrated within practical lab-on-a-chip systems.

## 4.2 Introduction

Molecular diagnostic methods that detect pathogen-specific markers within the genome offer key advantages, such as rapid sample-to-answer-time and strain-specific identification, compared to conventional culture-based testing used for infectious diseases diagnostics.[173] In spite of these advantages, molecular methods have not made the predicted impact in resource-poor regions having a high infectious disease burden.[174] This implies the need for portable and miniaturized, easy-to-use, low-power, and inexpensive point-of-care (POC) platforms, which are highly suitable for use in resource-poor and low-income settings.[175] Chip-based platforms are ideal for implementing POC systems as several hundreds or thousands of miniaturized devices, with dimensions in the nano- to microscale, can be integrated into a single platform using scalable manufacturing methods.[176] However, in spite of recent advancements in developing on-chip biosensing platforms,[177] their lack of integration with suitable sample preparation systems has restricted their use in resource-poor and POC settings.[15]

Cell lysis is a critical sample preparation step for nucleic acid detection, as DNA or RNA molecules need to be extracted from cells to be analyzed using chip-based platforms.[178] Lysis by permanent rupture of the cell membrane and/ or cell wall has been achieved through chemical,[179], [180] biochemical (enzymatic),[181] mechanical,[182], [183] thermal,[184], [185] or electrical[186]–[189] means. Electrical lysis, through irreversible electroporation and/or electrochemical species generation, is ideal for integration into POC devices due to its controllability, reagent-free nature, rapid response time, and compatibility with on-chip fabrication.[15]

Recently, there has been great interest in the field towards engineering lysis electrodes that are optimized in geometric configuration and structure for creating devices that combine high lysis efficiency with low voltage operation.[190] A commonly used method to lower voltage requirements deals with designing devices with electrode configurations that confine the applied electric potential to spatially-confined regions. These systems either use decreased separations between microelectrodes[191] or microfluidic channels to focus the potential drop across small spatial locations.[192], [193] In addition, structurally-tuned electrodes with features on multiple length-scales have been shown to outperform those made with only bulk materials in cell lysis applications. Carbon nanotube-modified stainless steel electrodes[39], [40] and zinc oxide nanorod-modified aluminium electrodes[194] have been used to obtain lower voltage requirements and higher lysis efficiencies compared to their device counterparts made from bulk materials, due to electric field enhancement at the sharp nanoscale features. Another structure-related approach has focused on creating high aspect ratio three dimensional electrodes, which allow a larger sample volume to be exposed to the active lysing region within the device.[191], [195]

Our vision was to create high efficiency lysis devices (>95 %) with a voltage requirement of less than 12 V (for battery operation), which could be manufactured in a rapid, inexpensive and scalable fashion. For this purpose, we sought to engineer lysis electrodes combining all three of the previously mentioned approaches: reducing the inter-electrode separation, incorporating nanoscale materials onto the electrode surfaces, and creating solution penetrating three-dimensional and high aspect ratio electrodes. This would require materials with different feature sizes – millimeter scale features for electrical contact, microscale features for the electrode body, and nanoscale features for enhancing device performance – to be combined on a single platform.

Integrating materials with a wide range of length-scales onto a single chip-based system remains challenging as methods optimized for fabrication in a certain length-scale may become too expensive or time-consuming when used for fabricating materials in a different length-scale. Lithography-based techniques are ideal for fabricating structures in the 0.5-100 µm range,[58] bottom up methods based on self-assembly are ideal for fabricating materials in the 1-100 nm range,[196] and traditional machining techniques are ideal for manufacturing in the macroscale.[197] Here we present a new benchtop method based on craft cutting, heat-induced thin film wrinkling, and electrodeposition to create closely spaced nanostructured microelectrode arrays in a matter of hours from design to testing. In order to minimize the cost of such devices, we avoided using expensive glass and silicon substrates[66] and selected plastic substrates which are more appropriate for single-use disposable devices.[175] These devices are then used to study the effect of electrode structure on the lysis efficiency and voltage requirement of the chip-based system.

## 4.3 Experimental

### 4.3.1 Reagents

Hydrogen tetrachloroaurate(III) trihydrate ($HAuCl_4 \cdot 3H_2O$, > 99.9%), hydrochloric acid (HCl ACS reagent, 37%), 1.0M pH 7.4 phosphate buffer, 10X tris-acetic acid-EDTA buffer, LB Miller broth, bovine serum albumin (BSA), 10X polymerase chain reaction

(PCR) buffer, Taq polymerase, and HaeIII endonuclease were purchased from Sigma-Aldrich (St. Louis, Missouri). Sulfuric acid ($H_2SO_4$, 98%) and formaldehyde were purchased from Calden (Georgetown, Ontario). All reagents were of analytical grade and were used without further purification. Milli-Q grade water (18.2 MΩ) was used to prepare all solutions.

### 4.3.2 Device Fabrication

Adhesive vinyl (FDC 4304, FDC graphic films, South Bend, Indiana) was bound to pre-stressed polystyrene (PS) (Graphix Shrink Film, Graphix, Maple Heights, Ohio) sheets. The desired lysis electrode layout was cut into the vinyl layer using a Robo Pro CE5000-40-CRP vinyl cutter (Graphtec America Inc., Irvine, CA). Gold (100 nm) was sputtered from a 99.999% purity gold target (LTS Chemical Inc., Chestnut Ridge, New York) using a Torr Compact Research Coater CRC-600 manual planar magnetron sputtering system (New Windsor, New York). After sputtering, the remaining vinyl was removed from the PS and the devices were shrunk in an oven (Fisher Scientific, Marietta, OH) at 160°C for 3 minutes.

Electrodeposition for the electrodeposited devices was performed using a CHI 420B Electrochemical Analyzer (CH Instrument, Austin, Texas) and a standard three-electrode set-up. The electrochemical system consisted of an Ag/AgCl reference electrode, a platinum mesh counter electrode, and PS lysis devices as the working electrode. Gold nanostructures were grown by electrodeposition on the crumpled gold using solutions containing 20 mM $HAuCl_4$ in 1 M HCl at a potential of -0.1 V vs. Ag/AgCl for 360 s.

The planar devices were fabricated through conventional photolithography and a lift-off process in order to obtain electrodes with critical dimensions smaller than the minimum step size of the craft cutter (100 μm). PS substrates the same dimensions as those for the wrinkled devices (30 mm x 40 mm) were first shrunk in an oven (Fisher Scientific, Marietta, OH) at 160°C for 3 minutes. The PS substrates were cleaned by sonication in isopropyl alcohol, followed by rinsing with Milli-Q grade water, and dried using a dry nitrogen stream. Positive photoresist (S1808; MicroChem, Inc.) was spun on the PS and followed by baking. A transparency mask with the interdigitated electrode pattern with dimensions that were 40 % of the vinyl mask geometry (to be approximately the same dimensions as the after shrinking pattern) was used to pattern the resist layer using UV exposure. After developing the photoresist, 100 nm of gold was sputtered to create the planar electrodes on the device. Photoresist stripper (SVC-175, Rohm Haas, Philadelphia, Pennsylvania) was used to remove the photoresist layer.

### 4.3.3 Scanning Electron Microscopy

SEM images of the different lysis devices (planar, wrinkled, and electrodeposited) were obtained using a JEOL JSM-7000S scanning electron microscope with an accelerating voltage of 2 kV, working distance of 6 mm, and low probe current.

### 4.3.4 Electrochemical Characterization of Device Surface Area

Cyclic voltammetry (CV) in 0.1 M $H_2SO_4$ was carried out to determine the electroactive surface area of each of the lysis electrode structures with CHI 420B Electrochemical Analyzer (CH Instrument, Austin, Texas) and a standard three-electrode set-up. The electrochemical system consisted of an Ag/AgCl reference electrode, a platinum mesh counter electrode, and PS lysis devices as the working electrode. Ten CV cycles between

0 to 1.5 V was performed on each electrode structures, and the charge transferred during the reduction section was used to calculate the surface area (surface area = charge/surface charge density) using the surface charge density of a monolayer of gold, 386 μC $cm^{-2}$. Three separate devices were measured for each electrode structure and the average surface area was calculated.

### 4.3.5 Bacteria Preparation

*E. coli DH5α* inoculated into LB Miller broth and incubated at 37°C overnight. Liquid culture diluted 1:100 into fresh LB broth in the morning, and grown into late log phase (OD600~0.8). Cells were washed and suspended into 10 mM phosphate buffer at a concentration of $10^7$ cells/ml. *E. Coli BL21 (DE3*) containing plasmids for green fluorescence protein (GFP) were inoculated into LB Miller broth with ampicillin (100 μg/ml) and incubated at 37°C overnight. Liquid culture diluted 1:100 into fresh LB broth containing ampicillin in the morning, and grown to OD600~0.6 and IPTG was added to a final concentration of 1 mM. Bacteria were incubated for another 2.5 hours before being washed and suspended in 10 mM phosphate buffer to a final concentration of $10^8$ cells/ml.

### 4.3.6 Lysis Experimental Setup

The lysis devices were rinsed with 70 % ethanol for 5 minutes, rinsed with sterile Milli-Q grade water, and dried with a dry nitrogen stream prior to use. The lysis devices were mounted onto a microscope slide using double sided tape and the hooked test leads were attached to the device. The bacteria sample was manually mixed using a pipette and 13 μl was deposited onto the electrode array. The bacteria sample formed a droplet on the electrode array. In order to spread the droplet over the array and minimize evaporation during the experiment, a sterilized coverslip coated with 1.5 % BSA was placed on top of the drop and device, causing the height to of the liquid on the device to be approximately 200 µm. A sequence of voltage pulses was then applied using a Keithley 236 Source and Measure Unit (Keithley, Tektronix). The pulse sequence consisted of a single voltage (V) pulse applied for 500 ms at a 0.67 Hz for 30 s (20 pulses total). Pulses were chosen over applying a DC voltage because it minimized bubble formation. The voltage (V) pulses tested were 0, 2, 4, 6, 8, and 10 V. The coverslip was carefully removed with sterilized tweezers and the liquid sample was pipetted off and mixed with the remaining sample drop on the electrodes. Finally, 10 µl of the sample was pipetted off the electrode array and subsequently used for lysis evaluation (cell viability, membrane permeability, or nucleic acid release). All devices were intended for single use, but were decontaminated prior to disposal by sonication in 70% EtOH for 10 minutes, and rinsing with de-ionized water.

### 4.3.7 Cell Viability (Agar Plating)

10 µl of treated bacteria was pipetted off the device and the appropriate serial dilutions ($10^{-2}$, $10^{-3}$, and $10^{-4}$ dilution factors) were performed in 10 mM phosphate buffer. 10 µl from each dilution step was pipetted onto the LB-agar plates and spread using a sterile disposable microbiological spreader (Lazy-L-Spreaders, Excel Scientific, Inc). Plates were inverted and incubated at 37°C for 16 hours until colonies formed on the plates. Plates were removed from the incubator and the number of colonies on each plate was counted. The concentration in colony forming units per milliliter (CFU/ml) was determined from the following equation:

$$\mathrm{CFU/ml} = Numberof\ colonies \times \frac{1}{dilution\ factor} \times \frac{1000\mu\mathrm{l/ml}}{10\mu\mathrm{l}}$$

The concentration of the sample was determined by averaging the determined concentration for each countable dilution step plated. Each voltage condition was tested on at least three separate devices. The cell lysis efficiency at each voltage was determined as:

$$Lysis\ Efficiency = (1 - \frac{\text{CFU/ml for condition}}{\text{CFU/ml for 0V}}) \times 100\%$$

### 4.3.8 Cell Membrane Permeability (Fluorescence Microscopy)

10 µl lysate from *E. Coli BL21 (DE3)* was stained with 10 µl of 60 µM propidium iodide (PI) (Molecular Probes, Invitrogen, Eugene, Oregon), and imaged with IX 51 inverted microscope (Olympus, USA) after 30 minutes incubation in the dark. Fluorescence images were captured using a QImaging Retiga 2000R camera (monochromatic, BX53) with FITC and Texas Red filters for the GFP and PI observation, respectively. The pseudocolor green and red fluorescence images were merged and processed using cellSens Dimension software, contrast was enhanced with Adobe Photoshop CS4 of all images the same way (Increase contrast 3).

### 4.3.9 Nucleic Acid Analysis (PCR)

E. coli DH5α was cultured and suspended identically to the conditions stated in 4.3.5 Bacteria Preparation. Cells were lysed at 0 V, 4 V, and 8 V using the previously mentioned lysing parameters on electrodeposited devices. Lysate was diluted 1:25 in additional phosphate buffer then centrifuged at 10,000 g for 10 min at 4°C. The top 50 µl of supernatant was collected and homogenized via pulse vortex for 10 s. Cells unexposed to the devices were diluted and centrifuged using the previously stated parameters, and were used as a negative control. A positive control was generated from the active culture similarly; however, it was not centrifuged in order to assess the total DNA content within unlysed cells during the PCR high temperature steps. Ten microlitres from the homogenized extract of each lysate was mixed with dNTPs, primers, and Taq Polymerase to final concentrations of 200 µM, 0.1 µM, and 0.1 unit/µl respectively. Samples were buffered with 10X PCR buffer to a final volume of 50 µl. Primer sequence and thermal cycling conditions were mimicked from Lu et al.[198] Ten microlitres of amplicon was run on a 3% agarose gel in tris-borate-EDTA buffer and run at 80 V for 1.5 hours before imaging with Redsafe nucleic acid stain.

### 4.3.10 COMSOL Simulations

The electric fields of the different electrode types and Joule heating of the electrodeposited device were numerically modelled using the finite element analysis software COMSOL Multiphysics 4.2 (COMSOL, Burlington, MA). In both simulations, a two-dimensional model was created for the cross-sectional model of the device and a physics-controlled mesh was implemented with extremely fine element sizes. The electric field simulations were calculated based on the standard values for electric conductivity and relative permittivity of the materials used in the model. A potential of 4 V was applied to the electrodes and the electric field distribution and magnitudes were calculated. For the Joule heating model, all three edges of the device and the coverslip are in contact with room temperature air. The heat equation was solved for with 4 V applied to the electrodes, assuming all the electrical energy is converted to heat.

## 4.4 Results and Discussion

### 4.4.1 Device Fabrication

To study the effect of electrode structure on the lysis efficiency and voltage requirement of the devices, we created three sets of devices using (1) craft cutting and polymer-induced thin film wrinkling (wrinkled device), (2) craft cutting and polymer-induced wrinkling followed by electrodeposition (electrodeposited device), and (3) photolithography on a shrinkable polymer (planar device). The first two sets of rapidly fabricated devices, were fabricated by a benchtop and rapid milli/micro/nanofabrication method developed at our laboratory (Figure 4.1).[199] This method allows transferring the electrode design created using Computer Aided Design (CAD) software onto a vinyl-coated polystyrene (PS) substrate using a craftcutter (Figure 4.1 (i-iii)). A craftcutter is an electronic cutting machine, originally developed for artists and hobbyists, which allows designs created using a CAD software to be automatically cut using a sharp blade into a variety of substrates. The patterned vinyl was used as a shadow mask through which gold was sputtered onto the pre-stressed PS, followed by the removal of the vinyl mask (Figure 4.1 (iv-v)). The substrate was heated following the sputtering process to shrink the pre-stressed PS and induce wrinkling in the gold thin film (Figure 4.1 (vi)). The PS shrinking process exerts a compressive stress on the sputtered gold film, causing it to wrinkle on the surface of the PS and decrease the effective lateral electrode dimensions to ~40% of their original size. We have shown previously that the wrinkled features of these structures can be precisely tuned by varying the gold film thickness, and consequently, parameters such as resistance, wettability, and surface roughness can be controlled.[199] The electrodeposited devices

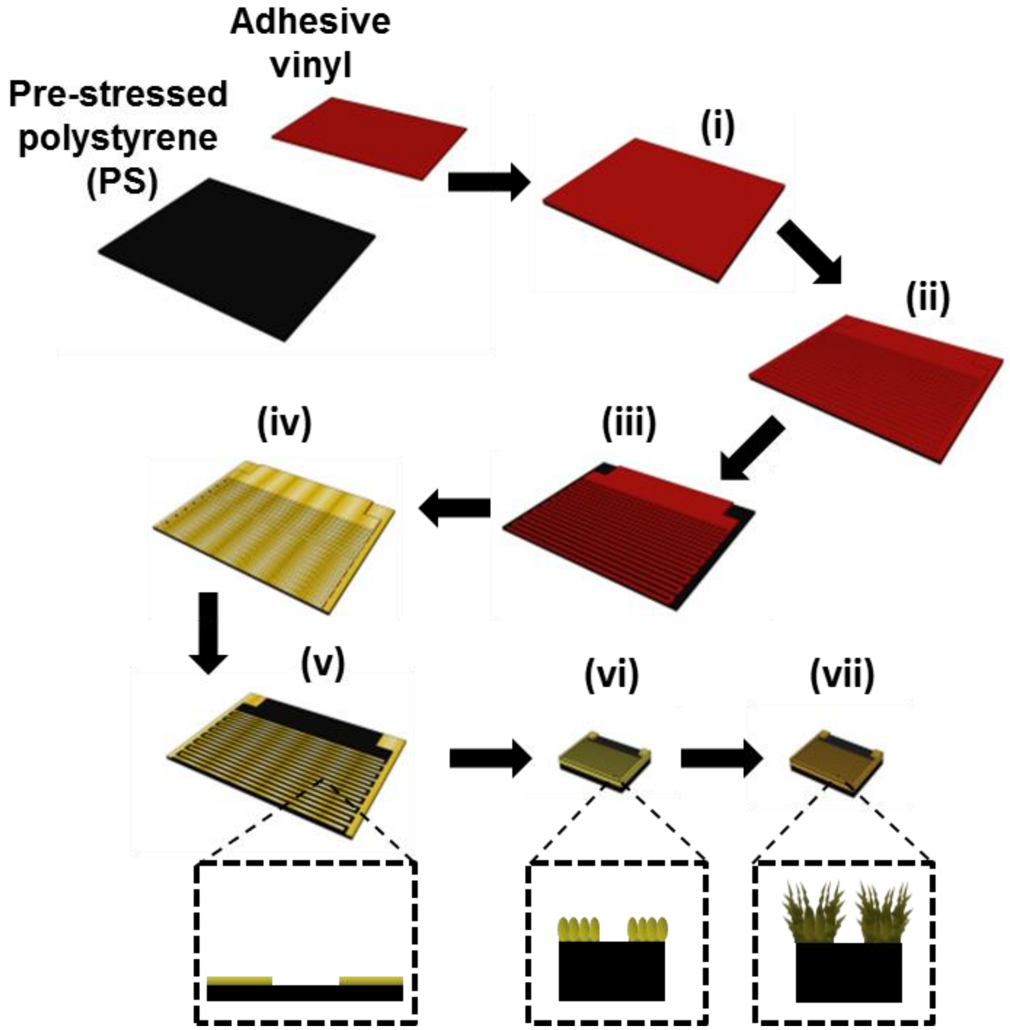

Figure 4.1 Schematic representation of the rapid prototyping fabrication process flow: (i) binding adhesive vinyl to PS, (ii) cutting electrode pattern into vinyl, (iii) removing vinyl cutout to create shadow mask, (iv) sputtering gold, (v) removal of vinyl mask, (vi) heating PS above glass transition temperature to induce shrinking and wrinkling of gold film, and (vii) optional electrodeposition of gold nanostructures on wrinkled gold electrodes. Insets in sub-figures (v-vii) demonstrate the enlarged side-view schematic drawing of each electrode type.

were fabricated with an additional fabrication step of electrodepositing sharp gold structures on the wrinkled electrodes (Figure 4.1 (vii)). In order to compare the performance of the two types of rapidly fabricated lysis devices to planar gold electrodes, we used conventional photolithography and lift-off to create electrode arrays made from non-textured surfaces (planar devices).

### 4.4.2 Device Characterization

The top-view schematic drawing of the three different device types is presented in Figure 4.2 (a). To observe the differences in structure, size, and aspect ratio of these three classes of lysis electrodes, we characterized them using optical and scanning electron microscopy (SEM) (Figure 4.2 (b)). It is clear from the optical microscopy images of the three electrode structures (Figure 4.2 (b)-top row) that their overall dimensions and inter-electrode separations were very similar. However, high resolution imaging through SEM (Figure 4.2 (b)-middle rows) revealed major differences in the morphology and surface texture of these electrodes. The planar devices displayed a mostly smooth surface, with uneven sparsely-spaced defects caused by the sputtering process. The wrinkled devices displayed continuously wrinkled structures that came to sharp peaks ($< 1\mu m$) in between frequent valleys, and a surface that appeared much rougher than the planar electrodes. The base of the electrodeposited devices appeared to be identical to that of the wrinkled electrodes, but they were decorated with sharp, feather-like structures. The electrodeposited structures came to points that were measured to be < 100 nm. The side-view SEM images (Figure 4.2 (b)-bottom row) gave an indication to the difference in electrode heights. It is apparent that the wrinkled electrodes had a significant height increase compared to the planar devices, almost two orders of magnitude (100 nm to ~10 μm), due to the crumpling of gold into a smaller surface area. Moreover, the electrodeposition process increases the electrode height even further to greater than 20 μm.

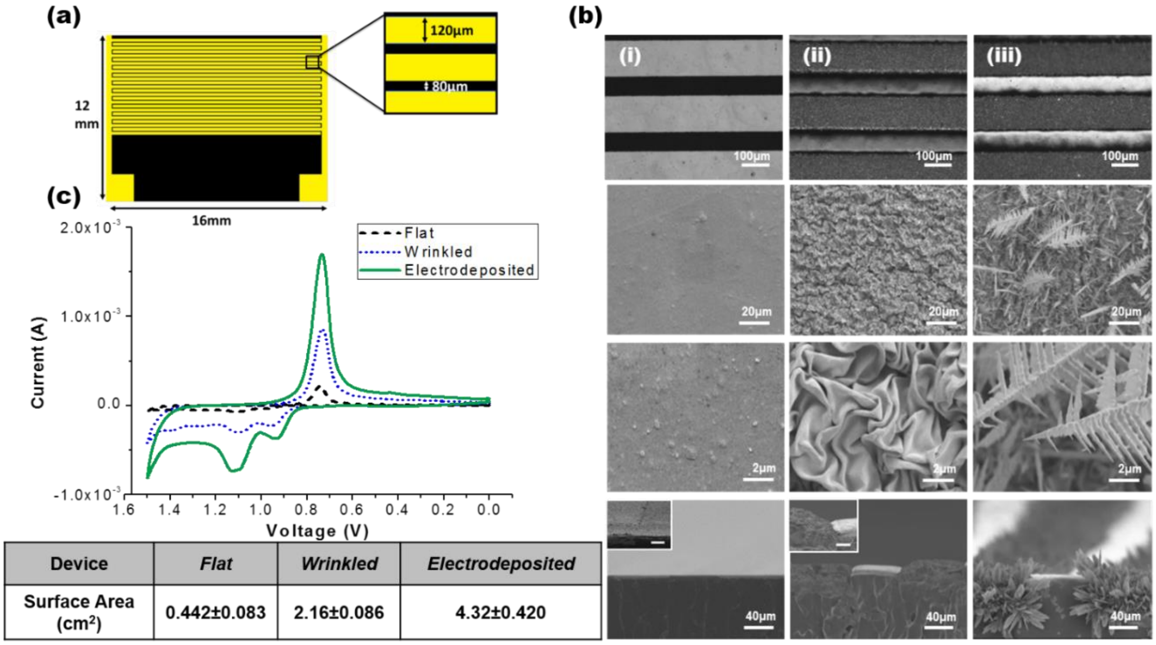

| Device | *Flat* | *Wrinkled* | *Electrodeposited* |
|---|---|---|---|
| Surface Area ($cm^2$) | 0.442±0.083 | 2.16±0.086 | 4.32±0.420 |

Figure 4.2 Characterization of the three classes of electrodes: planar, wrinkled and electrodeposited. a) Schematic of lysis device dimensions. b) First row: optical micrographs of all three electrode types (i) planar, (ii) wrinkled, (iii) electrodeposited; Second row: low magnification SEM images showing electrode textures; Third row: high magnification SEM images showing electrode textures; Fourth row: Side-view SEM images showing the electrode heights, insets show higher magnification of electrode edge (scale bar: 20 µm for planar, 10 µm for wrinkled). c) Overlaid cyclic voltammograms for all electrode structures and a table of the calculated electrode surface areas below. The average surface area (from three different devices) followed by the standard deviation is presented in the table.

The surface areas of the three electrode types were measured electrochemically using cyclic voltammetry (CV) in dilute sulfuric acid. The resulting cyclic voltammograms for all three electrode types were overlaid and are displayed in Figure 4.2 (c). The calculated surface area for each device, based on the charge transferred during the reduction region of the CV curve, is also displayed below the overlaid cyclic voltammograms. It is evident that the surface area of the electrodes on the rapidly prototyped devices, wrinkled and electrodeposited, is significantly greater than that of the planar devices, nearly five and ten times larger, respectively. In addition to the increased surface area, the rapidly prototyped electrodes have increased adhesion to the polystyrene substrate after shrinking, as tested by the scotch tape method.[199] This is a clear advantage resulting from the newly-developed fabrication technique, which we suspect would be highly beneficial for creating devices that are to be operated in 'wet' environments.

### 4.4.3 Lysate Analysis

We hypothesized that wrinkled and electrodeposited structures would increase electrical lysis efficiency through charge crowding at the spike tips resulting in the lightning rod effect and greatly enhancing electric field strengths at these points.[39] In addition, the observed height and surface area increases could be highly beneficial during the electrical lysis process by exposing a larger sample volume to the electric field,[191] or by providing an increased area for direct oxidation of cells or producing oxidizing agents in the solution.[200] To address this hypothesis and understand the effect of electrode structure and height on the device lysis efficiency, we tested the lysing capabilities of the three different electrode types using *Escherichia coli (E. coli)* samples as explained in detail in the Experimental Section. The bacterial sample was manually mixed and deposited onto the electrode array, and covered using bovine-serum albumin-coated coverslips. Voltage pulses were applied to the devices, and then an aliquot of the treated sample was used for further analysis to determine lysis efficiency or nucleic acid release efficiency.

Plate counting before and after voltage application was used to determine bacterial cell culture viability and the fraction of viable bacteria present in a voltage-treated sample, respectively. Electric potential was applied to the lysis device by grounding one set of the interdigitated electrodes and applying a low frequency rectangular pulse train to the other electrode. We tested voltage pulse trains with peak values of: 0, 2, 4, 6, 8, and 10 V. The lysis efficiency, in terms of cell viability, was found at each voltage by comparing the cell counts for each of the 2-10 V treatments to the 0 V treated samples considered as the negative control, which is shown in the graph of Figure 4.3 (a). For the planar devices, the lysis efficiency increases steadily with voltage, but does not exceed 80 % even at the highest voltage tested. It should be noted that the planar electrodes began to visibly corrode at applied voltages of 8 V or higher, which could have impacted their lysis efficiency at these potentials. This degradation of the electrodes was not observed for either of rapidly prototyped devices, indicating that they are more robust electrode structures. The lack of degradation for these electrodes may be due to the thicker gold layer created through multiple layers of wrinkled gold stacked on top of each other. The wrinkled devices displayed a similar trend as the planar; however, the lysis efficiency curve was shifted upwards demonstrating higher lysis efficiencies compared to planar devices at the same voltages. Over 95 % lysis efficiency was achieved at 8 V for the wrinkled devices. The

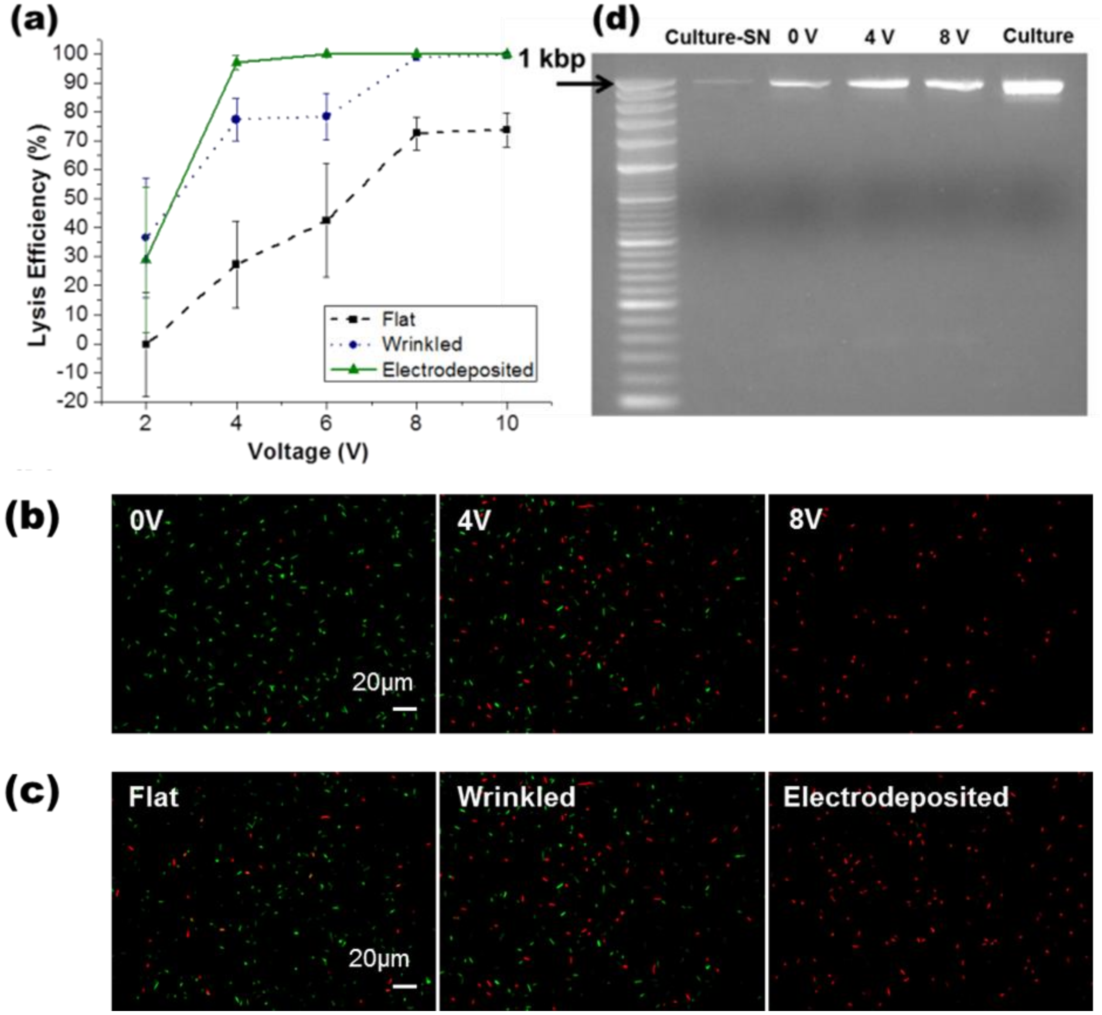

Figure 4.3 Studying the effect of electric potential and structure on the lysis process. a) Graph of lysis efficiencies derived from bacterial culture experiments for planar, wrinkled, and electrodeposited devices with respect to magnitude of voltage pulses applied. b) Fluorescence microscopy images showing the effect of voltage on membrane damage using wrinkled electrodes. c) Fluorescence microscopy images showing the effect of electrode structure on membrane damage at an applied potential of 4 V. Scale bars refer to 20 μm. d) Gel electrophoresis analysis of PCR amplicons of supernatants extracted from non-treated samples (Culture-SN), supernatant of samples placed on the devices under the potentials of 0, 4, and 8 V, and non-centrifuged cultures (Culture).

electrodeposited devices performed significantly better in terms of lysis efficiency compared to planar and wrinkled devices: the number of colonies drastically decreased between the 2 V and the 4 V treatments, and a lysis efficiency higher than 95 % was achieved at 4 V. Moreover, applying electrical pulses having peak values of 4 V or lower, yielded a negligible amount of bubbles generated due to electrolysis of the media, which further emphasizes the importance of low-voltage lysis.

In addition to the culture-based cell lysis assay, the effect of applied voltage on membrane damage was confirmed using fluorescence microscopy in the presence of a membrane impermeable stain, propidium iodide (PI). For this experiment, E. coli BL21 (DE3) expressing green fluorescence protein (GFP) was treated with a subset of voltages used for the plating experiment described above using the wrinkled devices. It is known that PI only penetrates bacteria with compromised membranes, indicating lysis, and stains the nucleic acids of such cells red with an excitation/emission maximum at 490/635 nm.[201] The merged pseudocolor fluorescent images obtained for lysis at 0 V, 4 V, and 8 V are displayed in Figure 4.3 (b). A clear trend is visible in these images: at 0 V, almost all of the cells fluoresce green indicating that PI has not penetrated into the cells and that these cell are not damaged; as the voltage is increased to 4 V, a combination of red and green cells are apparent with the majority of cells fluorescing red indicating voltage-induced damage to the bacterial cell wall/membrane; at 8 V, almost all cells fluoresce red indicating high efficiency lysis. The fluorescence microscopy images are in very good agreement with the culture-based results demonstrating the voltage dependence of the lysis process and indicating that high efficiency lysis is indeed possible at an applied potential of 8 V for the wrinkled structures.

The effect of electrode structure on the voltage-induced lysis was also validated using fluorescence microscopy to monitor cell wall/membrane permeabilization. For this purpose, we applied 4 V pulses to the three different classes of devices and observed the damage induced to the GFP-expressing bacteria in the presence of PI. It should be noted that at this potential, the device degradation and bubble generation were at a negligible level for all three electrode types. The same methods as above were used to distinguish between damaged cells fluorescing red and undamaged cells fluorescing green. The fluorescence images presented in Figure 4.3 (c) indicate that the majority of cells treated on the planar device fluoresce green, with very few cells staining red, indicating that most of the *E. coli* bacteria were still alive in this sample. A mix of red and green stained cells are observed in the image for the wrinkled device, indicating a mix of live and dead cells in this sample. Finally, the sample treated on the electrodeposited device appeared to be almost all stained red, suggesting that the vast majority of the cells were lysed. The fluorescence microscopy results agree with the bacterial culture-based results indicating that the electrode structure greatly influences the lysis efficiency at a given potential. This suggests that voltage requirements for on-chip lysis devices can be greatly reduced simply by altering the electrode structure towards 3D, high surface area, high aspect ratio electrodes featuring sharp nanoscale features as achieved by the electrodeposited devices demonstrated here.

The experiments based on bacterial culture and fluorescence microscopy demonstrated the effect of the applied potential and electrode structure on cell viability and cell wall/membrane intactness, respectively. However, for the demonstrated lysis device to be usable in lab-on-a-chip systems, it is essential for nucleic acids to be released from cells. To demonstrate that nucleic acids are indeed extracted using our on-chip lysis protocol, we applied polymerase chain reaction (PCR) to amplify a specific region of the 16s rRNA gene of *E. coli* directly from the cell lysate supernatant processed using our electrodeposited devices. The cell lysate supernatant was used instead of unprocessed lysate to remove the intact cells present in the samples, and to avoid skewed results due to the heat lysis of *E. coli* during the PCR denaturing step (94°C). The supernatant of samples treated with voltages 0, 4, 8 V, the supernatant taken directly from the liquid culture (culture-SN) and samples taken directly from the liquid culture (culture) without the centrifugation step were put through the PCR process and served as the sample, negative control and positive control (Figure 4.3 (d)). The PCR product from each sample was analyzed using gel electrophoresis to visually study the presence, absence or relative quantity of the E. coli DNA in each sample. It is evident from the gel results demonstrated in Figure 4.3 (d) that increasing the applied potential from 0 to 4 V increases the amount of free chromosomal DNA available for amplification as the band intensity increases by about 90%. However, increasing the potential beyond 4 V to 8 V changes the band intensity by less than 10%. The trends seen here are similar to those obtained from culture-based lysis characterization of electrodeposited devices (Figure 4.3 (a)). It is interesting to note that there was a noticeable increase in amplicon intensity from the supernatant extracted from the active culture (culture-SN) compared to the supernatant from the sample placed on the device without any voltage applied (0 V). We hypothesize this to be due to the mechanical lysis induced because of the sharp nanoscale tips on the electrode surface (Di Carlo et al., 2003).[202] It can also be seen that the bands for the samples treated with voltages are not as intense as the band of the liquid culture sample (culture). This could be due to the residual nucleic acids being left on the electrodes after the voltage application.

### 4.4.4 Lysis Mechanism

In order to confirm that the lysis observed here was indeed electrical – electric-field assisted or electrochemical – and not due to the heat generated as a result of Joule heating, we performed COMSOL modelling to calculate the temperature increase that occurs during device operation. A 2D model was created, which consisted of the electrode array cross section. The model geometry was based on the side-view SEM images of the electrodeposited device (Figure 4.4 (a)). The electrode cross sections were modelled as rectangles that had sharp nanoscale features extending from the electrodes into the solution (40 μm thick, 140 μm wide, separated by 60 μm) and a 4 V potential was applied between alternating electrodes. The model contained gold electrodes on the PS base, which were surrounded by a liquid having the materials properties of phosphate buffer solution. Similar to the experimental setup used, the model included a glass coverslip (200 μm thick) on top of the liquid layer. It is evident from these results that the applied voltage causes a temperature increase in the liquid surrounding the electrodes. However, due to an increase in temperature of less than 6° C yielding an operating temperature of under 30°C, Joule heating was eliminated here as a possible mechanism for bacterial lysis.[203]

The voltage dependence of the lysis efficiency observed in Figure 4.3 along with the negligible temperature increase suggested by Figure 4.4 (a) indicates that the application

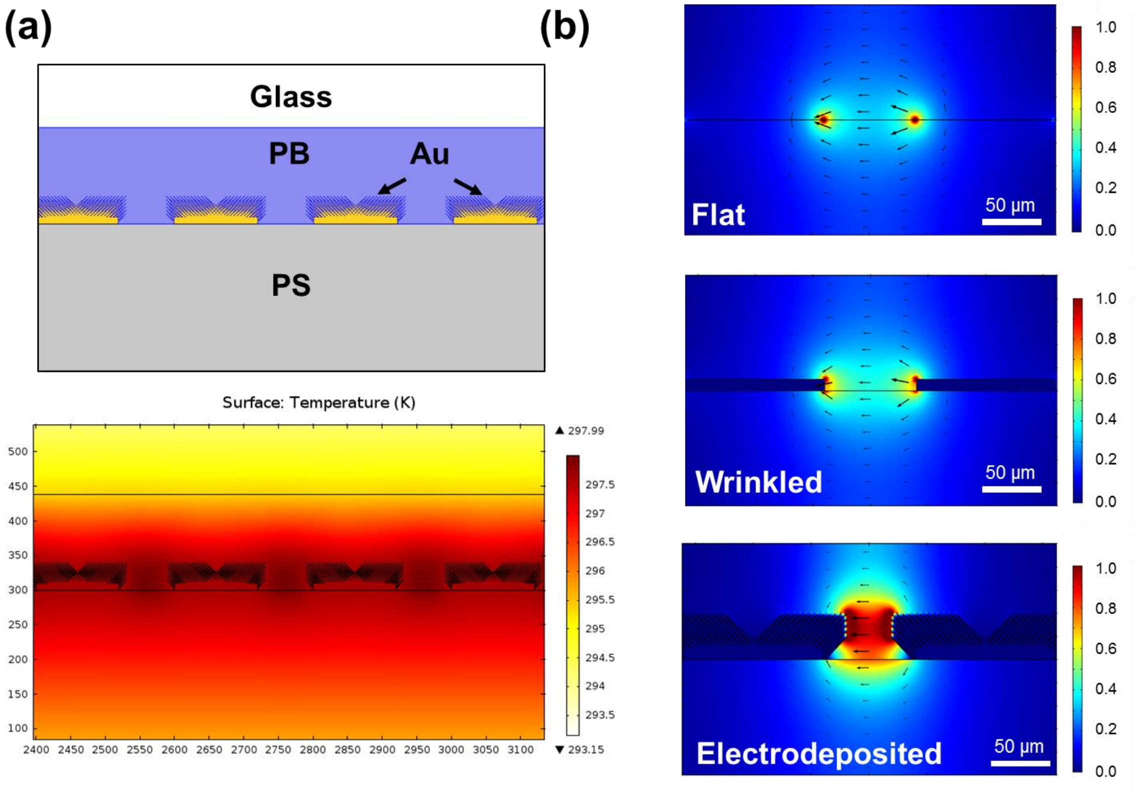

Figure 4.4 Analysing the mechanism of lysis a) Cross-sectional view of the electrodeposited lysis device (top) and COMSOL simulation of temperature distribution due to Joule heating (bottom). b) Electric field distributions and magnitudes (legend units in kV/cm) simulated between two electrodes at 4 V in COMSOL for the three electrode types. The arrow plot shows the electric field normal and the length of the arrows are proportional to their magnitudes.

of electric potential is responsible for the bacterial lysis observed here. In order to determine if the voltage-induced lysis of these three device types was due to local electrochemical hydroxide production at the cathode[200], an experiment was performed to monitor the solution pH upon voltage application. This was done by adding universal pH indicator to the phosphate buffer solution and observing the resultant colour change within the liquid. The measured pH of 11 was well within the previously reported pH range (>10) necessary for *E. coli* lysis.[204] While electrochemical hydroxide generation may be the predominant mechanism for lysis in these devices, electric field assisted lysis could also be present, contributing to the high lysis efficiency that was observed at 4 V for the electrodeposited devices. To validate this hypothesis, 2D simulations of the electric field generated for each of the electrode types were performed and the electric field distribution is shown in Figure 4.4 (b). The models were based on the geometries that were obtained from SEM images of the devices similar to those presented in Figure 4.2. The flat devices were modelled as thin rectangular electrodes (100 nm thick, 120 μm wide, separated by 80 μm), the wrinkled devices were modelled as high aspect ratio rectangular electrodes (10 μm thick, 120 μm wide, separated by 80 μm), and the electrodeposited devices were modelled as the wrinkled electrode with sharp nanoscale features extending from the electrodes into the solution (40 μm thick, 140 μm wide, separated by 60 μm). Similar to the heat generation models presented above, the electrodes were modelled on a polystyrene substrate and surrounded by a phosphate buffer solution. It can be seen that the area of the solution that experiences the electric field strength of at least 1 kV/cm, the minimum needed to induce cell lysis in *E. Coli*,[205] differs greatly between the electrodes. While the flat and wrinkled electrodes do have a very high local electric field at the edges of the electrodes, the field decays rapidly when moving away from the edges. The electrodeposited electrodes provide a much larger region within the solution with the electric field of at least 1 kV/cm, which supports the hypothesis of structure-dependant electric field enhancement with these devices.

## 4.5 Conclusions

In summary, we have developed a new rapid prototyping method for creating multi-scale electrodes with features ranging from the millimeter scale to the nanometer scale. This fabrication method enabled us to create disposable chips with high aspect ratio 3D microelectrodes decorated with nanoscale features and microscale inter-electrode separations at a low-cost. We show that the lysis efficiency of the devices can be controlled by changing the applied voltage and the electrode structure. Through numerical modelling, we demonstrate that temperature increase due to Joule heating is minimal, confirming that electrical lysis is achieved here. It is evident from this work that tuning the electrode structures decreases the required voltage and increases the lysis efficiency of on-chip lysis devices. Using structurally-optimized electrodes created here, we achieved a lysis efficiency higher than 95 % at an applied potential of 4 V for E. coli cells, making them a potential candidate for integration in portable lab-on-a-chip systems. Additional studies are being performed to better understand the effect of applied potential and electrode structure on the lysis of different bacterial cell types, and to determine the applicability of these electrode system to a wide range of infectious disease applications.

## 4.6 Acknowledgements

The authors acknowledge funding support through NSERC Discovery Grant and PGSD scholarship, Canada Foundation for Innovation, Ontario Ministry of Research and Innovation, and Grand Challenges Canada, Rising Stars in Global Health programs. The electron microscopy research described in this paper was performed at the Canadian Centre for Electron Microscopy at McMaster University, which is supported by NSERC and other government agencies. The authors would like to thank Z. Peng for his support with photolithographic fabrication.

# Chapter 5 Rapid Prototyping of Microfluidic Devices with Integrated Wrinkled Gold Micro-/Nano Textured Electrodes for Electrochemical Analysis

## Chapter Introduction (Objective E)

Microfluidics are integral to the creation LOC POC devices, as they transport the liquid phase sample through the various stages of sample preparation to the biosensor, as well as provide a barrier to the environment external to the device. This chapter focuses on the benchtop integration of the wrinkled electrodes on PS substrates, fabricated using the technique discussed in Chapter 3, with microfluidics to create contained electrochemical devices. The bonding of unconventional substrates, like thermoplastic polymers, to conventional microfluidic materials, like PDMS, has challenged many scientists and engineers. Moreover, features with substantial height (>5 µm) and rough texture, such as the electrodes fabricated using the patterning technique in Chapter 3, limit the conformal contact and subsequent bonding between the microfluidics and bottom substrate, as evidenced by our investigation into the bonding interfaces using electron microscopy. We assess various bonding methods for PDMS microfluidic integration with the wrinkled electrodes on polystyrene using electron microscopy, flow rate testing, and burst pressure testing, ultimately overcoming these two bonding issues using surface modification and partial curing of the PDMS microchannels. The bonding technique that has the best performance when subjected to flow rate (>25 mL/min) and burst pressure testing (>125 kPa), is used to create an integrated electrochemical flowcell with a three-electrode setup on the benchtop. The detection of a standard redox analyte is performed under stagnant and flow conditions with the electrochemical behaviour that is predicted by theory.

**Authors:** Christine Gabardo, Robert Chris Adams-McGavin, Oriana Vanderfleet, Leyla Soleymani

**Publication:** Analyst, 140, 16, 5781-5788

**Publication Date:** July 2015

## 5.1 Abstract

Fully-integrated electro-fluidic systems with micro-/nano-scale features have a wide range of applications in lab-on-a-chip systems used for biosensing, biological sample processing, and environmental monitoring. Rapid prototyping of application-specific electro-fluidic systems is envisioned to facilitate the testing, validation, and market translation of several lab-on-a-chip systems. Towards this goal, we developed a rapid prototyping process for creating wrinkled micro-/nano-textured electrodes on shape memory polymers, fabricating microfluidics using molds patterned by a craft-cutter, and bonding electrical and fluidic circuitries using a PDMS partial curing method optimized for creating void-free bonds at the side walls and surfaces of tall (> 5 μm) micro-/nano-textured wrinkled electrodes. The resulting electro-fluidic devices, featuring closely spaced high topography electrodes for electrochemical analysis, can withstand flow-rates and burst pressures larger than 25 mL/min and 125 kPa, respectively. In addition, the fully-integrated electrochemical flow-cell developed here demonstrates excellent electrochemical behaviour with negligible scan to scan variation for over 100 cyclic

voltammetry scans and expected redox signatures measured under various voltage scan rates and fluidic flow rates.

## 5.2 Introduction

Lab-on-a-chip (LOC) systems that allow chemical and biological reactions to be controlled in small volumes using miniaturized devices are being developed for many applications including use in drug discovery,[206], [207] point-of-care pathogen sensing,[208] and environmental analysis.[209] When macro-scale laboratory components are miniaturized into micro-/nano-scale, it becomes possible to integrate multiple (tens to thousands) devices on a single platform for creating handheld, portable and low-cost systems.[210] In contrast to standard microelectronics devices, LOC systems require the integration of solid phase devices with liquid phase samples and reagents. This implies that miniaturizing the solid-phase devices must be paralleled with scale down of liquid volumes and liquid handling components, making microfluidics an essential part of LOC systems. Microfluidics integration is often achieved using monolithic or hybrid approaches where matching or heterogeneous materials are bonded together to create microchannel networks for functional devices. Soft lithography has revolutionized the area of microfluidics by making it possible to create microchannels rapidly and inexpensively by casting polydimethylsiloxane (PDMS) into microfabricated molds.[70] PDMS has excellent optical properties, has high electrical resistivity, is easily released from mold surfaces, and is flexible enough to bond to both flat and curved surfaces.[71] PDMS has been bonded to PDMS to create monolithic microfluidic devices through surface modification,[211] corona discharge, uncured PDMS adhesive, cross-linker variation, and partial curing techniques.[212] PDMS can also be irreversibly bonded to glass, silicon, and quartz substrates using oxygen plasma treatments.[213] Polymer substrates, like polystyrene (PS), offer several advantages over traditionally used silicon and glass substrates for fabricating LOC devices including lower material costs, the possibility of new form factors, disposability, and compatibility with less expensive batch processing techniques.[66] PS substrates are also inert, biocompatible, and durable, making them applicable to biosensing systems.[214] Since PDMS microfluidics and PS substrates are both widely used in microsystems, it is often desirable to integrate these two materials to create a sealed hybrid microfluidic system. Previous methods for bonding PDMS and PS or other thermoplastics include plasma treatment,[215] surface modification through silanization,[211], [216]–[219] and the use of an adhesive layer.[220] However, the integration of these materials can become challenging when non-planar polystyrene substrates with micro- or nano-scale roughness and features are used.

LOC platforms often require the integration of electrodes and microfluidic networks to create electro-fluidic devices capable of electrical actuation or sensing in liquid samples. We have previously developed a benchtop method for rapidly prototyping electrical biosensing[221] and sample preparation[222], [223] devices on PS substrates. In this method, the electrodes are deposited onto a shrinkable PS substrate by sputtering tens to hundreds of nanometers of metal through an adhesive vinyl mask patterned through xurography.[199] The device is then heated over the PS glass transition temperature to induce the shrinking of the polymer substrate. The polymer shrinking process enables the miniaturization of the patterned electrodes and causes the metallic thin films to wrinkle, in one or two dimensions, due to the mismatch in the mechanical properties of the stiff metallic thin film and the compliant substrate. The resulting wrinkled electrodes display structural advantages including enhanced substrate adhesion compared to planar electrodes, texturized surfaces with feature sizes that are controllable in the nanometer to micrometer length-scales by tuning the film thickness, and increased heights that extend into the tens of microns length-scale.[199]

The high surface area, three-dimensional nature, and sharp nanoscale features of these wrinkled electrodes have been previously exploited to improve the performance of sample preparation and bioanalytical devices. For example, wrinkled gold electrodes have been used to lower the voltage needed to electrically lyse bacterial cells through increasing the device interaction volume and enhancing the local electric field strength generated at nanoscale tips of the wrinkles.[222] Biosensing devices based on optical, plasmonic, or electrochemical detection of analytes have also been developed to exploit the benefits of the wrinkled surfaces.[137] Electrochemiluminescent sensors based on wrinkled gold surfaces have demonstrated enhanced sensitivities and lower limits of detection compared to planar devices due to their increased surface area.[224] DNA microarrays fabricated from wrinkled $SiO_2$ structures demonstrated the ability to enhance the fluorescence signal of bound fluorophores, which translated to improved detection sensitivity and 30–45 times greater signal-to-noise ratio compared to flat glass substrates.[225] Surface enhanced Raman scattering substrates have been fabricated using wrinkled nanoporous $Au_{79}Ag_{21}$ films. These substrates demonstrated electromagnetic “hot spots” at the sharp creases and tips of the wrinkles, and enabled single molecule detection.[49] Furthermore, multiplexed electrochemical DNA sensors fabricated using structurally tunable wrinkled electrodes allowed for a higher concentration of immobilized DNA probes compared to planar substrates due their increased surface area. In addition, these substrates offered the unique capability to control the density of immobilized DNA probes by controlling the thickness of the gold film.[221]

Although these wrinkled electrode devices have shown both mechanical and analytical advantages, fully contained devices with microfluidic channels have not been realized due to the challenge of bonding channels over the wrinkled three dimensional electrodes present on the PS substrates. The difficulty arises from the large topographical variation in electrode height (hill-to-valley measurements of about 10 μm) induced by the wrinkling process. As observed by many researchers, the mechanical flexibility of PDMS elastomer is not adequate to allow a conformal contact between the microfluidics, the polymer substrate, and the thick film (>5 μm) electrodes.[226] As a result, poor microfluidic to substrate adhesion and rapid device failure are observed in functional electro-fluidic devices with microscale electrode topography, such as screen printed electrodes.[227] Therefore, there is a need to develop alternative PDMS to polymer bonding techniques to account for thick film electrodes having large variations in height.

Here we present a rapid fabrication method to produce three-dimensional multi-scale electrodes on polymeric substrates, create microfluidic channels in PDMS, and develop fully integrated electrochemical flow cells. The integration of electrochemical devices with closed flow-through microfluidics has been made possible by our assessment of multiple methods for bonding PDMS and patterned polystyrene substrates that feature three-dimensional and micro-/nano-textured electrodes. Through these studies, we developed a bonding method based on partially cured PDMS, which enables intimate and void-free contact between the microfluidics, the substrate, and the electrodes having microtextured surfaces and microscale side walls. These fully integrated electro-fluidic systems that combined a multiplexed arrangement of working, reference, and counter electrodes inside a fluidic system, were then used for the analysis of electroactive species under static conditions and fluidic flow.

## 5.3 Experimental

### 5.3.1 Reagents

Potassium hexacyanoferrate(II) trihydrate/ potassium ferrocyanide ($K_4Fe(CN)_6$ ·3H2O, > 98.5%), potassium chloride (KCl, ≥ 99.0%) and (3-Aminopropyl)triethoxysilane (APTES) were purchased from Sigma-Aldrich (St. Louis, Missouri). Sulfuric acid ($H_2SO_4$, 98%) was purchased from Calden (Georgetown, Ontario). All reagents were of analytical grade and were used without further purification. Milli-Q grade water (18.2 M Ω) was used to prepare all solutions.

### 5.3.2 Patterned PS Fabrication

Unshrunk pre-stressed PS substrates (Graphix Shrink Film, Graphix, Maple Heights, Ohio) were covered in self-adhesive vinyl cut-outs (Figure 5.1(a) (i)) using a roller. The patterns were designed in Adobe Illustrator, with inlet and outlet holes, as well as any electrode layouts that were needed. Inlet and outlet holes were designed to be 6.25 mm in diameter and the design was cut out from vinyl covered PS sheets using the Robo Pro CE5000- 40-CRP vinyl cutter (Graphtec America Inc., Irvine, CA). The design was cut repeatedly until the PS pieces separated. The electrode patterns were also cut through the vinyl mask at the same time using a lower programmed force (Figure 5.1 (a) (ii). The vinyl cut-outs for the electrodes were then removed and the remaining vinyl acted as a mask (Figure 5.1 (a) (iii), which was then sputtered with 200 nm of gold (Figure 5.1 (a) (iv). After sputtering, the vinyl mask was removed (Figure 5.1 (a) (v)). The patterned PS substrate was then placed in an oven (Model: 664, Fisher Scientific, Marietta, OH) at 160℃ for 3 minutes, or until the pre-stressed PS completely shrunk and flattened (Figure 5.1 (a) (vi). This caused the PS sheet to decrease in length and width to 40% of the original size, and increased height to greater than 600% of the original size[22]. Tubing (8000-0002 x 180 PVC Tubing, Thermo Scientific) was placed into the inlet and outlet holes, approximately 2.5 mm in diameter after shrinking, and Super

Glue Ultra Gel (Lepage, Mississauga, Ontario, Canada) placed around interface between the PS and tubing (Figure 5.1 (c)).

### 5.3.3 Microfluidic Channel Mold Fabrication

The molds used to produce the microfluidic channels were fabricated out of self-adhesive vinyl cut-outs (FDC 4304, FDC graphic films, South Bend, Indiana) bound to cleaned pre-stressed polystyrene (PS) substrates (Graphix Shrink Film, Graphix, Maple Heights, Ohio). The self-adhesive vinyl sheet is spread over the pre-stressed PS sheet using a roller prior to producing the cut-outs to form the molds (Figure 5.1 (b) (i)). The desired microfluidic channel layout was designed in Adobe Illustrator, and the channel layout was cut into the vinyl covering the PS sheet (Figure 5.1 (b) (ii) using the Robo Pro CE5000- 40-CRP vinyl cutter (Graphtec America Inc., Irvine, CA). Vinyl was removed from the bonding area, leaving the channel design intact (Figure 5.1 (b) (iii)).

### 5.3.4 Channel Fabrication

The vinyl/PS molds were secured into a petri dish using double sided tape. Sylgard 184 Silicone Elastomer Kit (Dow Corning Corporation, Midland, MI, USA) was mixed in a 10:1 ratio of elastomer to curing agent by weight and mixed thoroughly. The mixture was then degassed, and poured into the petri-dish containing the channel molds (Figure 5.1 (b) (vi)) and allowed to cure for 24 hours (partially cure) or 48 hours (fully cure) at room temperature. It should be noted that although the partially cured PDMS was cured for 24 hours at room temperature, a faster curing time can be achieved by heating the sample at 60°C for 35 minutes.[212] The

PDMS was then removed from the mold using a single-edge razor blade and tweezers (Figure 5.1 (v)).

### 5.3.5 Bonding Techniques

Seven PDMS-PS bonding techniques were tested and each had 5 or fewer steps prior to firmly contacting the PS substrate and PDMS microfluidics together to seal the device. They are summarized in Table 5.1. The first step was curing the PDMS channels on the molds, which was done at room temperature for 24 hours for the partially cured channels or 48 hours for the fully cured channels. Step 2 was an air plasma surface oxidation treatment, which was conducted by placing the PS substrate in the Expanded Plasma Cleaner (Harrick Plasma) on HIGH RF power setting for 60 seconds. Step 3 was APTES treatment of the activated PS substrates, which was performed by placing the plasma treated substrates immediately into a 1% (v/v) APTES solution at room temperature for 20 minutes. After the APTES immersion, substrates were rinsed with DI water and dried with air. Step 4 was the activation of the APTES on the surface of the PS substrate by treating it with air plasma on the HIGH RF power setting for 60 seconds. Step 5 was the air plasma activation of the PDMS microfluidics, which was also performed in the plasma cleaner on HIGH RF power for 60 seconds. Finally, the PS substrate and PDMS microfluidics were brought into firm contact with each other to complete the bond. For the techniques that used partially cured PDMS (PC, PC-P, PC-PA, and PC-PAP), the PDMS was allowed to cure for another 24 hours prior to testing.

### 5.3.6 Bond Strength Testing

A standard design (Figure 5.1) was used to measure the maximum flow rate a bonding technique could withstand before failure. The fluidic channels were 5 mm long, 500 μm wide, and 90 μm tall. Reservoirs 3 mm wide, 3 mm long, and 90 μm tall were placed at the end of the channel over the inlet and outlets. Devices contained two parallel wrinkled gold electrodes (200 nm thick, 500 μm wide, separated by a 500 μm gap before shrinking) across the channel of the device.

An 18G1 needle was then inserted into the inlet (tubing) of the testing devices. A plastic 60 ml Becton Dickinson syringe was filled with a mixture of blue dye and DI water. A syringe pump (Harvard Apparatus, 11 Ellite I/W) was used to pump a constant flow rate of the mixture into the device. Firstly, the devices were tested using a flow rate of 0.5 mL/min for 10 seconds. The flow rate was incremented by 0.5 mL/min for periods of 10 seconds until device failure was observed, at which point the greatest flow rate successfully withstood was recorded.

Burst pressure tests were also performed on devices with the same electrode configuration as the flow rate testing devices bonded with PDMS using the PC-PA (Table 5.1) technique. These devices had microchannels that were 5 mm long, 500 μm wide, and 90 μm tall with an inlet reservoir that was 3 mm wide by 3 mm long, for a total volume of 1.035 μL. The microchannel was connected to a pressure sensor (PX273–300DI, Omega Engineering Inc., CT, USA) and the syringe pump through a T-shaped fluidic interconnect. The voltage output from the pressure sensor was measured by a voltmeter (Keithley 2410, Keithley Instruments Inc., OH, USA) and recorded on a computer using Agilent Benchvue 1.1 software (Keysight Technologies, Santa Rosa, CA, USA). There was no outlet to the microchannel and a syringe pump flow rate of 0.5 mL/min was used to slowly increase the pressure in the microchannel until it burst.

### 5.3.7 Electrochemical Device Testing

Electrochemistry experiments were performed in a system fabricated on the PS and integrated with a PDMS microfluidic channel to form a contained electrochemical cell. The electrochemical cell, shown in Figure 5.3 (a), consisted of two gold working electrodes, a gold reference electrode, and a gold counter electrode. The microfluidic channel was 90 μm tall, 3 mm wide and 16 mm long and bonded to the device using the Partial Curing and APTES technique (PC-PA). Cyclic voltammetry (CV) was performed with the electrochemical cell using a CHI 660D electrochemical workstation (CH Instrument, Austin, Texas). CV was performed at various flow rates (0 μL/min, 100 μL/min, and 1000 μL/min) with a ferrocyanide solution of 2 mM $K_4Fe(CN)_6$ in 0.1 M KCl. The voltage was cycled between -0.2 and 0.4 V vs. Au at the following scan rates: 0.01, 0.02, 0.04, and 0.08 V/ s. CV scans were also performed on each device with a solution of 0.05 M $H_2SO_4$ to determine the electrochemically active surface area of the working electrodes, as well as electrochemically polish the electrodes prior to bonding to microfluidics. In order to assess the stability of the electrodes within the devices, 100 CV scans were performed in 2 mM $K_4Fe(CN)_6$ in 0.1 M KCl within the channel.

## 5.4 Device Fabrication and Integration

The benchtop fabrication process outlined in Figure 5.1 was used to create multi-scale electrode structures integrated with microfluidic networks. To create the PS substrate with micro-/nano- structured wrinkled gold electrodes, pre-stressed PS is covered with vinyl adhesive (Figure 5.1 (a) (i)). Benchtop craft cutting is then used to pattern the vinyl with the electrode design and make inlet and outlet holes into the pre-stressed PS substrate for interfacing the fluidic system with the outside world (Figure 5.1 (a) (ii)). The vinyl is removed from the pre-stressed PS substrate to form a vinyl shadow mask (Figure 5.1 (a) (iii)). The PS substrate is then sputtered with 200 nm of gold (Figure 5.1 (a) (iv)), and the vinyl shadow mask removed to reveal the electrodes (Figure 5.1 (a) (v)). The gold patterned substrate is then heated in an oven at 160℃ for 3 minutes or until completely flat (Figure 5.1 (a) (vi)). Previous studies have demonstrated that heating pre-stressed PS over its glass transition temperature results in a greater than 40 % reduction in length and width of the substrate, and an increase in height by over 600%, due to the relaxation of the polymer chains.[199] The contraction of the polymer substrate, exerts a compressive force on the metal film, which is relieved through the wrinkling of the gold. This shrinking process reduces the minimum feature sizes achievable using the simple craft-cutter-based patterning method and it incorporates wrinkled three-dimensional microelectrodes onto the device.

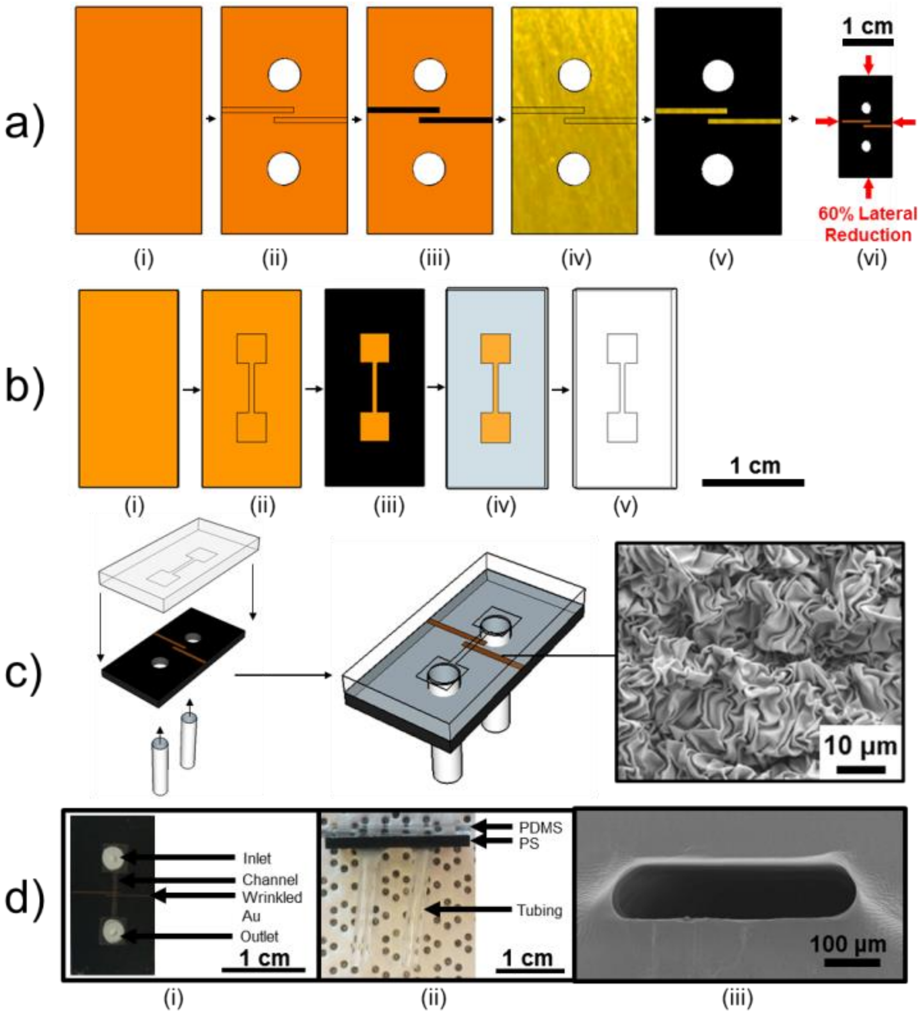

Figure 5.1 Development of the electro-fluidic devices a) Fabrication of patterned PS substrate (i) Unshrunk pre-stressed PS is covered with vinyl. (ii) Electrode pattern and inlet and outlet holes are patterned using a craft cutter (iii) Excess vinyl is removed to form a shadow mask (iv) Sputtering gold through vinyl shadow mask created by a craft cutter. (v) Removal of vinyl mask to reveal the electrode pattern. (iv) PS substrate is shrunk at 160°C. b) Fabrication of PDMS microchannel (i) Unshrunk pre-stressed PS is covered with vinyl. (ii) Channel geometry cut into the vinyl. (iii) Vinyl removed at specific locations leaving the mold containing the channel geometry. (iv) PDMS is poured on vinyl-PS mold. (v) Cured PDMS is removed from vinyl-PS mold. C) Inlet and outlet tubing inserted into patterned shrunken PS substrate and PDMS microchannel bonded to PS substrate to complete device. Inset demonstrates the scanning electron micrograph of the resulting wrinkled electrode structure. d) Demonstration of the fabricated device (i) Top-view and (ii) side-view photograph of the fully-integrated device. (iii) Cross-sectional SEM of the channel created using partial curing.

The abovementioned rapid prototyping method based on craft cutting was also used to fabricate the molds for casting the PDMS-based microfluidic channels. An adhesive vinyl film was first applied to non-shrunk pre-stressed PS (Figure 5.1 (b) (i)). A microfluidic channel geometry, was then cut into the vinyl sticker (Figure 5.1 (b) (ii)) using a robotic craft cutter, which can create intricate channel geometries with widths as small as 100 μm. Excess vinyl was then removed from the PS (Figure 5.1 (b) (iii)), creating the channel mold for soft lithography. PDMS was poured over the rapidly-prototyped vinyl, cured at room temperature (Figure 5.1 b) (iv)), and then removed from the mold (Figure 5.1 (b) (v) to form the patterned microchannel. This rapid prototyping method allows molds to be constructed in a matter of minutes, and used repeatedly (up to ~10 times) without degradation.

Tubing was then inserted into holes in the shrunken patterned PS substrate to form the inlet and outlet, and the PDMS microfluidic channel was bonded to the patterned PS substrate for creation of the electro-fluidic system (Figure 5.1 (c)). Seven techniques, summarized in Table 5.1, were assessed to bond the rapidly patterned PS substrates featuring the wrinkled electrodes to the PDMS microfluidic channels. The techniques either used partially cured (PC, PC-P, PC-PA, and PC-PAP) or fully cured (FC-P, FC-PA, FC-PAP) PDMS channels. While fully cured PDMS is usually used in bonded devices, partially cured PDMS has been used in a previous study[213] as an intermediate layer to seal PMMA channels due to its high viscosity and stickiness. We investigated bonding strategies based on partially cured PDMS because we hypothesized it would have suitable flexibility for sealing the micro-scale crevices of the wrinkled electrodes, while maintaining the overall channel shape. Photographs of flow testing devices are shown in Figure 5.1 (d) (i) and (ii). As it can be seen in the side-view device images (Figure 5.1 (d) (ii)), inlets and outlets were integrated into the PS substrate using craft cutting as this created more robust sealing around the tubing than when integrated in the PDMS layer. From the top view device image (Figure 5.1 (d) (i)), it can be seen that we have placed two closely spaced wrinkled three-dimensional electrodes to be perpendicular to the fluidic channels. This allows us to examine PDMS bonding to the PS substrate, the top surface of the wrinkled gold electrode, and most importantly the side walls of the wrinkled gold electrodes. The dimension and shape of the partially cured PDMS channel were characterized with cross-sectional SEM (Figure 5.1 (d) (iii)). The partial curing of the PDMS on the molds produced smooth and rounded channels, that could have applications in microfluidic platforms that mimic microvascular networks.[228] The fully cured PDMS had rectangular cross-sections, as determined by the cross-section of the vinyl mold (data not shown). With both curing methods, channels had heights of approximately 90 μm, due to the thickness of the vinyl film used.

The partially cured (PC) PDMS bonding method was tested without any surface modifications, as well as with previously used functionalization methods involving plasma treatment and surface coating with a silane terminated linker. Plasma treatment of PDMS using air or pure oxygen generates silanol (Si-OH) groups at the polymer surfaces, while similar treatment of PS results in hydroxyl group (-OH) formation on the surfaces. Coating the plasma-treated PS substrate with (3-Aminopropyl)triethoxysilane (APTES), covalently attaches this molecule to the substrate effectively silanizing the surface. The final functionalization method involved plasma activating the PS substrates, coating the activated PS with APTES, and plasma treating the APTES coated PS substrates prior to bonding it to plasma-activated PDMS through the formation of Si-O-Si covalent bonds upon surface contacts .[229] The second plasma treatment step was used to substitute the amine-termination of the APTES molecules with silanol groups for establishing strong Si-O-Si bonds between PS and PDMS substrates.[218]

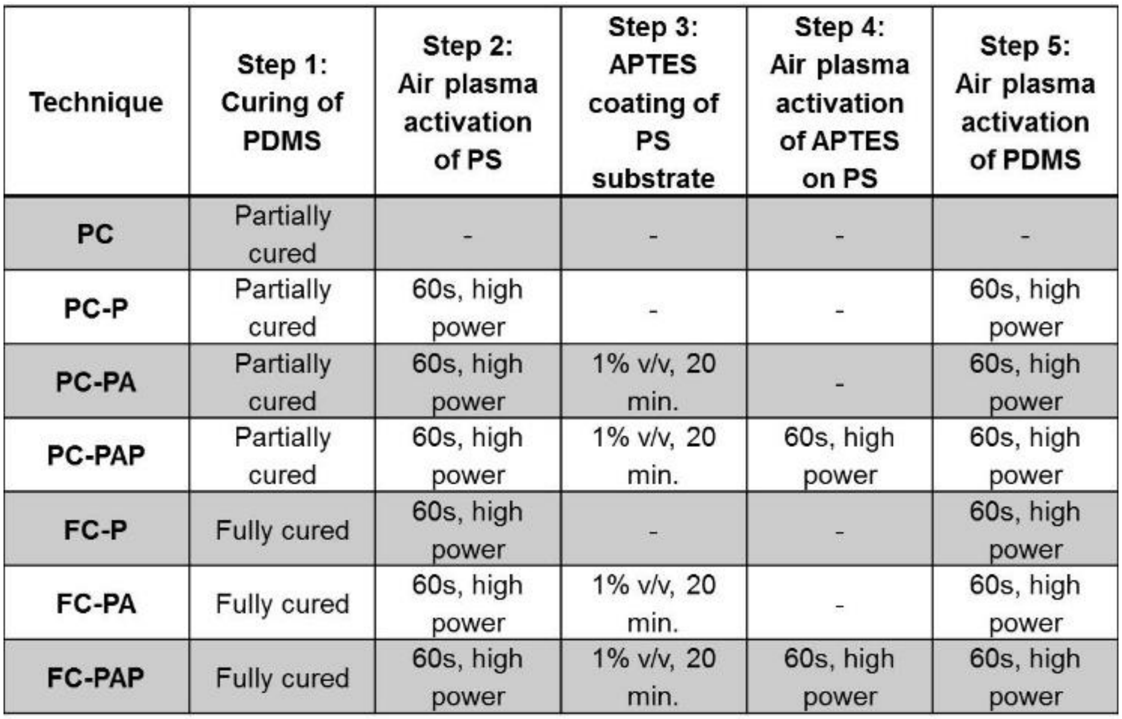

| Technique | Step 1: Curing of PDMS | Step 2: Air plasma activation of PS | Step 3: APTES coating of PS substrate | Step 4: Air plasma activation of APTES on PS | Step 5: Air plasma activation of PDMS |
|---|---|---|---|---|---|
| **PC** | Partially cured | - | - | - | - |
| **PC-P** | Partially cured | 60s, high power | - | - | 60s, high power |
| **PC-PA** | Partially cured | 60s, high power | 1% v/v, 20 min. | - | 60s, high power |
| **PC-PAP** | Partially cured | 60s, high power | 1% v/v, 20 min. | 60s, high power | 60s, high power |
| **FC-P** | Fully cured | 60s, high power | - | - | 60s, high power |
| **FC-PA** | Fully cured | 60s, high power | 1% v/v, 20 min. | - | 60s, high power |
| **FC-PAP** | Fully cured | 60s, high power | 1% v/v, 20 min. | 60s, high power | 60s, high power |

Table 5.1 Summary of PDMS/PS bonding techniques investigated.

## 5.5 Results and Discussion

### 5.5.1 Characterization of Bonding Techniques

The patterned PS substrates were bonded with PDMS microfluidics (Figure 5.2 (a)) using the above-mentioned seven bonding techniques and cross-sectional Scanning Electron Microscope (SEM) micrographs were obtained to visualize the bond interface between the PS, PDMS, and the nano/microtextured electrodes (Figure 5.2 (b)-(c)). The techniques that used fully cured PDMS (Figure 5.2 (b)) were seen to have an incomplete bond at the interface of the three materials, with micro-scale gaps observed between the PDMS and patterned PS. The bonding methods that used partially cured PDMS (Figure 5.2 (c)) were observed to have a much more conformal PDMS layer around the wrinkled electrode and the PS. This is schematically represented in Figure 5.2 (e). Based on these observations, we hypothesized that the devices that were bonded with fully cured PDMS (FC-P, FC-PA, and FC-PAP) would be more likely to fail at the electrode interface compared to their partially-cured counterparts.

There is a wide variety of integrated microdevices that require high operational flow rates, such as inertial devices and high throughput cell sorters.[230] However, operating under high flow rates can lead to channel leakage, a commonly encountered problem in microfluidics. In order to assess the reliability of the different bonding conditions under continuous flow conditions, we performed leakage testing experiments. The flow rate started at 0.5 mL/min and was increased by 0.5 mL/min increments until the devices failed. The maximum

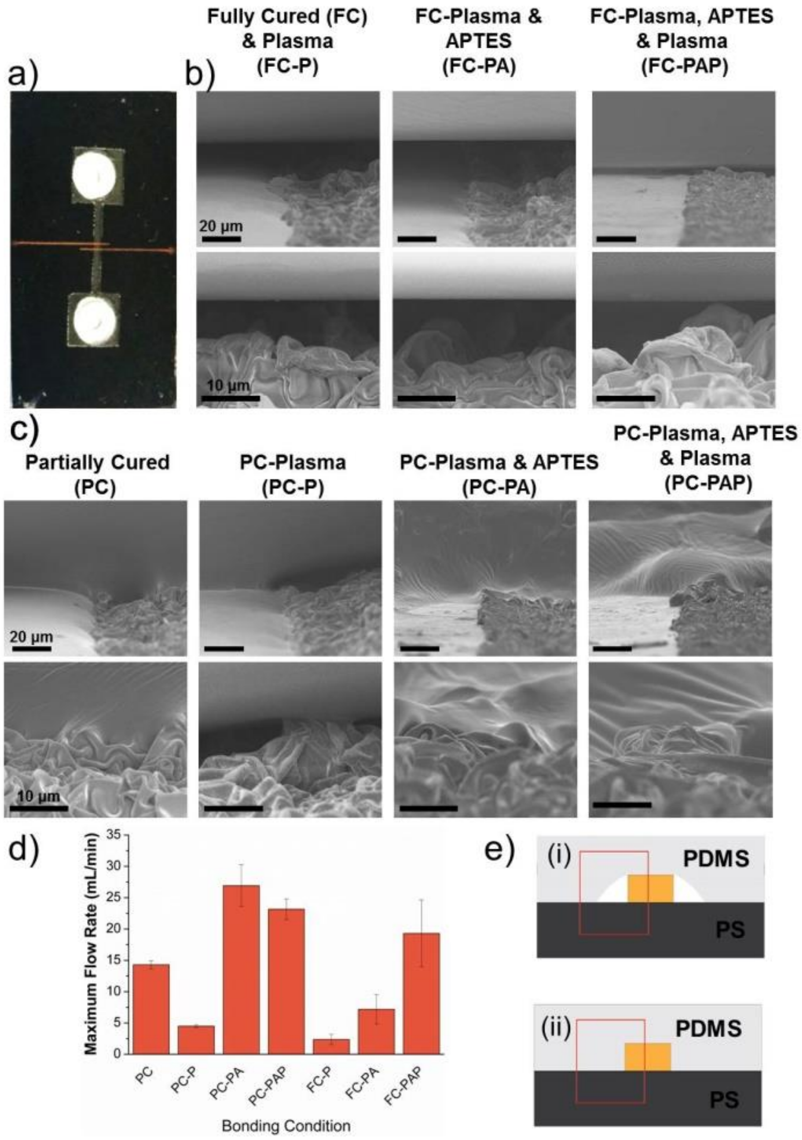

Figure 5.2 Characterization of the seven PS/PDMS bonding techniques. a) Top-view photograph of devices characterized here. b) Side-view SEM images of fully cured PDMS bonded over a wrinkled gold electrode with the different bonding techniques at a low (top row) and high (bottom row) magnification. c) Side-view SEM images of partially cured PDMS bonded over a wrinkled gold electrode with the different bonding techniques at a low (top row) and high (bottom row) magnification. d) Summary of maximum flow rates achieved before fluid leakage was observed using different bonding techniques. e) Schematic of bonding over a three-dimensional electrode (orange rectangle) patterned on PS with (i) fully cured PDMS techniques and with (ii) partially cured PDMS techniques. The red rectangle shows the approximate location for the low magnification images in (b) and (c).

flow rates for the different bonding techniques, as determined by the leakage testing are summarized in Figure 5.2 (d). It was observed that the fully cured techniques (FC-P, FC-PA, FC-PAP) achieved flow rates that were 17-73% lower than their partially-cured counterparts. (PC-P, PC-PA, PC-PAP) This is expected as SEM micrographs (Figure 5.2 (a)) demonstrated that bonding was not as effective across the surface of the fully cured PDMS. Leakage was observed around the interface between PDMS and electrodes, due to the ineffective bonding around the three-dimensional electrodes. The partial curing without surface modification of the PS (PC) was able to withstand average flow rates of 14.3 mL/min. The average maximum flow rate of the PC-P technique was unexpectedly lower (4.5 mL/min) than PC technique alone, although it was still stronger than the fully cured and plasma treated bonding (FC-P) technique (2.4 mL/min). This may be due to the cross-linking of the surface PDMS layer during the plasma treatment process,[231] resulting in a less efficient seal forming around the wrinkled electrodes. The method PC-PA achieved the highest average flow rate of any technique tested, with an average maximum flow rate of 26.9 mL/min, far exceeding the requirements of many lab-on-a-chip devices.[232] Furthermore, the maximum flow rates obtained here using the partially curing method are well-within range (4-60 mL/min)[216], [217], [219] of flow-rates achieved in previously reported PDMS/PS bonding methods that did not contain tall, high topography features. The PC-PAP method, with the extra plasma activation step, had a lower average maximum flow rate of 23.2 mL/min than PC-PA. Although the difference in the average maximum flow rates is not statistically significant, the PC-PA method has the advantage of not having an extra plasma activation step. We believe the PC-PA and PC-PAP methods perform significantly better than the PC-P method due to the presence of APTES on the gold electrodes and the PS base. APTES could be bonded to gold at the amino group through a weak covalent bond,[233] and the plasma activated PDMS could bond to the ethoxy or silanol groups through a condensation reaction.[234] Several microfluidic applications require devices to perform reliably under high pressures[235], making the burst pressure an important metric for evaluating bonding techniques. To investigate the maximum pressure our optimized device based on partial curing, plasma, and APTES treatments (PC-PA) can withstand, we performed the burst pressure test. In these tests, the syringe pump was used to pump in DI water mixed with dye into the inlets of the devices shown in Figure 5.2 (a), with their outlets sealed to increase the pressure until the device leaked. The maximum burst pressure for the optimized PC-PA device was ~130 kPa, which is similar to values obtained when PS and PDMS substrates lacking tall and high-topography features were bonded and tested using a similar liquid burst pressure testing setup[219]. Given the excellent liquid flow rate and burst pressure handled by the patterned PS/PDMS materials bonded using the PC-PA protocol, these devices were chosen for creating electrochemical flow cells.

### 5.5.2 Development of the Fully Integrated Electro-Fluidic Systems

The rapid prototyping of electrochemical cells has enabled advances in the areas of electroanalysis, power generation, and electrosynthesis.[236] To investigate the applicability of the rapid prototyping method developed here to electrochemical systems, we developed a fully-integrated electro-fluidic system. The electrochemical cell consisted of four gold electrodes: two concentric working electrodes (WEs) surrounded by a pseudo-reference electrode and a large surface area counter electrode. The pseudo-reference electrode was placed in close proximity to the working electrodes to minimize the ohmic drop between working and reference electrodes. The electrodes were deposited (100 nm) and then wrinkled using the previously described device shrinking technique based on a pre-stressed PS substrate.[199] Two working electrodes were fabricated to demonstrate the ability to develop arrays of individually-accessible electrodes on a single substrate for use in multiplexed biosensors[237]. The inner working electrode (1 WE) had an electroactive surface area, determined through cyclic voltammetry with sulfuric acid, of 0.02±0.002 $cm^2$ and both electrodes combined (2 WE) had an electroactive surface area of 0.04±0.002 $cm^2$. The PDMS was bonded to the device and a microfluidic channel contained all the electrodes. Inlets and outlets were installed and a photograph of a completed device is displayed in Figure 5.3 (a).

In order to assess the bonding capability of the PC-PA method over several three-dimensional nano-/micro-textured electrodes in a practical solution environment with continuous liquid contact, the electrochemical cells were evaluated by running cyclic voltammetry (CV) with the redox couple ferro-/ferricyanide, with and without flow. The robustness of the on-chip electrochemical cell was tested by continuously running 100 CV scans in a ferrocyanide solution (Figure 5.3 (b)). The expected redox signature of ferro/ferricyanide was observed with negligible scan-to-scan variability demonstrating the reliability, stability, and robustness of the system. Typical cyclic voltammograms obtained from the devices with one and two WEs under different scan rates are displayed in Figure 5.3 (c) (i) and (ii), respectively. The obtained curves display the characteristic peaks that are expected from this redox couple, as well as increasing peak current values with increasing scan rates. The peak oxidation and reduction currents were plotted against the square root of the scan rate for one and two WEs (Figure 5.3 (c) (iii)). It can be seen that the current linearly increases with the square root of the scan rate, as given by the Randles-Sevcik equation.[238] This demonstrates that the developed electrochemical cells display the predicted behaviour under static conditions.

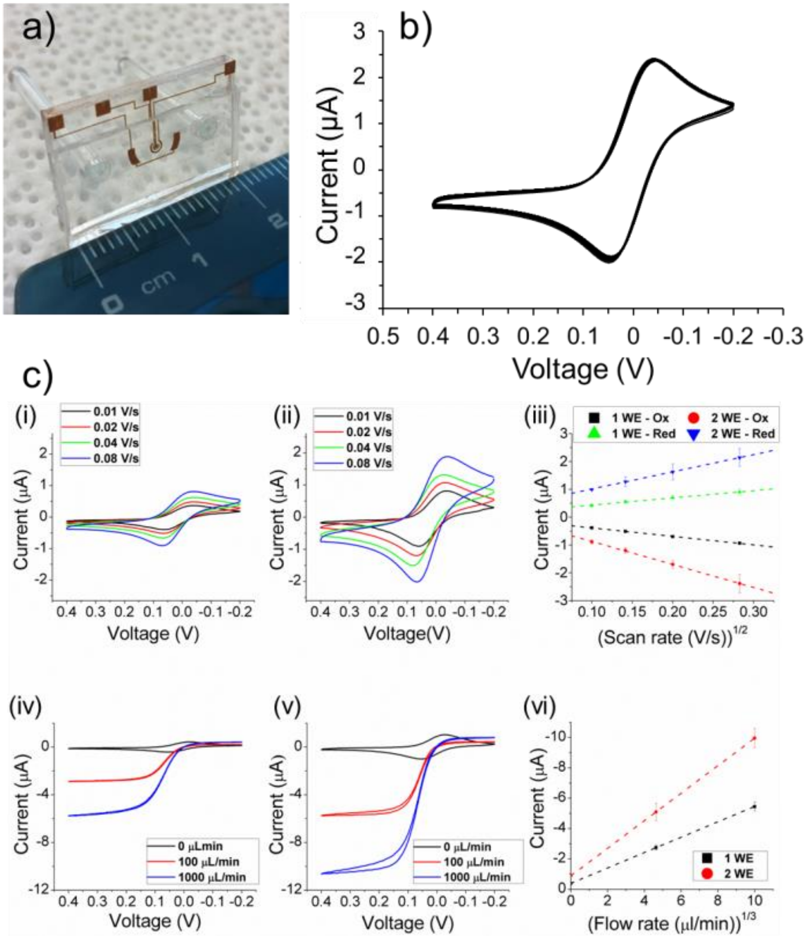

Figure 5.3 Electrochemical characterization of the electro-fluidic device a) Photograph of the electrochemical cell bonded to the PDMS microfluidics. b) Overlays of cyclic voltammograms for 100 consecutive cycles using two working electrodes in a solution of 2 mM potassium ferrocyanide in 0.1 M potassium chloride under no flow. c) Graphs of electrochemical behaviour of the devices in solutions containing 2 mM potassium ferrocyanide in 0.1 M potassium chloride. (i) Overlay of cyclic voltammograms using a single working electrode at different scan rates with no flow. (ii) Overlay of cyclic voltammograms using both working electrodes at different scan rates with no flow. (iii) Plot of the peak oxidation (Ox) and reduction (Red) currents for one and two working electrodes versus the square root of scan rate. Dashed lines are the linear fit for the data points ($R^2$ values > 0.99) and error bars are standard errors between multiple devices. (iv) Overlay of cyclic voltammograms using a single working electrode at 0.01 V/s scan rate for different flow rates. (v) Overlay of cyclic voltammograms using two working electrode at 0.01 V/s scan rate for different flow rates. (vi) Plot of peak oxidation current for one and two working electrodes versus the cubic root of the flow rate at a scan rate of 0.01 V/s.

Operating electrochemical systems under flow increases their current sensitivity by enhancing mass transport through convective flow compared to static devices operated under diffusion-limited conditions. We investigated the operation of the electro-fluidic device under flow by running CV scans as redox solutions were flown through the cells at 100 μL/min and 1000 μL/min. Overlays of the characteristic curves obtained at 0, 100, and 1000 μL/min flow rates for one and two WEs are displayed in Figure 5.3 (c) (iv) and (v), respectively. The shape of the cyclic voltammograms becomes sigmoidal when flow is introduced to the cell, which is expected under forced convection conditions. The peak oxidation currents for one and two WEs were plotted against the cubic root of the flow rate and the expected linear relationship, according to the Levich equation,[239] was observed. This indicates the applicability of the electro-fluidic devices developed here to a wide-range of static and flow-based electrochemical applications related to sensors, corrosion studies, super-capacitors, and batteries.

### 5.6 Conclusions

In summary, we developed a method to rapidly fabricate integrated electro-fluidic devices, consisting of PDMS microfluidic channels and three-dimensional wrinkled electrodes on PS thermoplastic substrates. We assessed various bonding techniques structurally using electron microscopy and operationally using leakage and burst pressure testing to determine which method would provide the most effective bond for use in electrochemical flow cells. The method based on bonding partially cured PDMS with APTES functionalized PS substrates significantly outperformed the other six techniques evaluated in terms of maximum achievable flow rate (maximum flow rate: 27 mL/min, maximum pressure 130 kPa). We applied the developed bonding technique to fabricate an inexpensive (<$1 per device) and disposable microfluidic electrochemical cell featuring high surface area three-dimensional electrodes. It was demonstrated that the voltammetric detection of electroactive analyte could be performed with these devices under flow and static conditions without the need for any off-chip electrodes, as well as that the electrodes demonstrated excellent stability for over a hundred cyclic voltammetry cycles.

## 5.7 Acknowledgements

The authors acknowledge funding support through NSERC Discovery Grant, USRA, and PGSD scholarship, Canada Foundation for Innovation, and Ontario Ministry of Research and Innovation. The electron microscopy research described in this paper was performed at the Canadian Centre for Electron Microscopy at McMaster University, which is supported by NSERC and other government agencies.

# Chapter 6 Rapid Prototyping of Structurally- and Functionally-Tunable All-Solution-Processed Electrodes Using Polymer-Induced Thin Film Wrinkling

## Chapter Introduction (Objectives B, C, and D)

All-solution processed conductor deposition is an attractive alternative to vacuum-based physical vapour techniques for the low-cost manufacturing of electrodes; however, the films deposited using these methods often suffer from low conductivity and poor substrate adhesion. In Chapter 3, a rapid benchtop approach to pattern hierarchical electrodes based on the combination of xurography and thin film wrinkling was presented. However, this fabrication method relies on the coating of a thin metallic layer onto the pre-stressed polymer substrate through vacuum-based deposition methods. We sought to overcome this limitation and produce a completely benchtop fabrication method by using all-solution processed conductor deposition techniques. Electroless deposition, directed by a nanoparticle seed layer, is used to deposit a high quality gold film on the substrate and is compatible with the patterning technique presented in Chapter 3. The growth of the gold film on the surface of the polymer substrate is studied. It is determined that both porous and non-porous wrinkled electrodes can be realized and tuned by varying the electroless deposition time/ thickness and the wrinkling process. The structural and functional properties of the wrinkled and non-wrinkled electrodes are assessed for various electroless deposition times, with the all-solution processed electrodes showing excellent adhesion (no peeling) when subjected to the tape test and resistance similar to the sputtered films. The porosity, a feature not observed in the sputter-deposited wrinkled films, show advantages over their continuous counterparts, including a higher surface area and a larger enhancement (>$10^4$ enhancement over planar sputtered films) in the intensity of SERS spectra when employed as substrates for chemical sensing.

**Authors:** Christine Gabardo, Robert Chris Adams-McGavin, Barnabas Fung, Eric Mahoney, Qiyin Fang, and Leyla Soleymani

**Publication:** To be submitted in 2016.

### 6.1 Abstract

Three-dimensional electrodes that are controllable over multiple length-scales are very important for use in bioanalytical systems that integrate solid-phase devices with solution-phase samples. Here we present a fabrication method based on all-solution-processing and thin film wrinkling using smart polymers that is ideal for rapid prototyping of tunable three-dimensional electrodes and is extendable to large volume manufacturing. Although all-solution processing is an attractive alternative to vapour-based techniques for low-cost manufacturing of electrodes, it often results in films suffering from low conductivity and poor substrate adhesion. These limitations are addressed here by using a smart polymer to create a conformal layer of overlapping wrinkles on the substrate to shorten the current path and embed the conductor onto the polymer layer. The structural evolution of these wrinkled electrodes, deposited by electroless deposition onto a nanoparticle seed layer, is studied at varying deposition times to understand its effects structural parameters such as porosity, wrinkle wavelength and height. Furthermore, the effect of structural parameters on functional parameters such as electro-active surface area and surface-enhanced Raman scattering are investigated. It

is found that wrinkling of electroless-deposited thin films can be used to reduce sheet resistance, increase surface area, and enhance the surface-enhanced Raman scattering signal.

## 6.2 Introduction

Conductive layers that interface between solid devices and liquid samples are critical components of electrical bioanalytical sensors and transducers.[31], [240]–[243] Borrowed from the microelectronics industry, vacuum-based vapor deposition technologies are commonly used to deposit conductive films onto the substrates of bioanalytical devices.[244], [245] While precise control over the deposited film thickness can be achieved with these methods, they rely on expensive vacuum-based instrumentation placed in multi-million dollar foundries for depositing and patterning thin films. This model works for large volume production of microelectronics; however, for bioanalytical devices that rely on inexpensive components (ex. disposable chips, strips, or cartridges), manufacturing methods which are more cost-effective at lower volume production are desirable.

Depositing and patterning electrodes using all-solution-processed methods, such as printing, enables device fabrication outside the semiconductor foundries and has been used for applications ranging from rapid prototyping to high volume production of bioanalytical devices, such as glucose monitoring strips.[246] However, the difficulty with printed bioanalytical electrodes for use in new and advanced applications, such as ultrasensitive biomolecular detection, is twofold. Firstly, these electrodes suffer from conductivity issues without high temperature post-printing steps which are incompatible with many polymer substrates needed for creating inexpensive disposable bioanalytical cartridges.[97] Secondly, it is difficult to create three-dimensional electrodes with controllable structural parameters that are critical for tuning the metrics of bioanalytical systems, such as sensitivity,[33] response time[50], [51], and power requirement.[222] To address the challenges involved in inexpensive fabrication of three-dimensional metallic electrodes for bioanalytical sensing, we sought to develop an all-solution processing method that (1) enabled the fabrication of high conductivity electrodes without the need for high temperature (>300°C[83] the minimum temperature for sintering gold nanoparticles and above the melting temperature of commonly used polymer substrates) processing, and (2) was suitable for the creation of three-dimensional metallic films with a high degree of structural tunability.

Electroless deposition is a facile and inexpensive solution-based method for producing high quality uniform and continuous metallic films on a variety of conductive and non-conductive substrates.[247] Although electroless deposition is able to create high quality conductive films, the resulting planar electrodes often lack functional micro-/nano-structures with significant height (>1 µm). Wrinkling, through the compression of thin films in-plane, presents a rapid and inexpensive method to controllably add multi-scale structuring to planar films and their footprints, features both important for creating bioanalytical systems.[116], [128], [199] Shrink-memory polymer thin film wrinkling as a method to structure conductive interfaces has mainly been applied to thin metallic films deposited with physical vapor deposition (PVD) methods.[128], [199] More recently, researchers have explored other methods to deposit conductive/semi-conductive films for subsequent wrinkled structuring, such as implanting or spray-coating metallic nanoparticles[248] or semiconductive nanocrystal films.[249] Although these methods introduced novel nanostructuring and/or porosity not observed in the PVD films, these deposition techniques did not produce the uniformity, continuity, and conductivity of PVD films due to the low density and/or non-uniform deposition of the nanomaterials. To date, thin film wrinkling has not been applied to all-solution-processed materials to induce controllable three-dimensional structuring. Therefore, it is important to explore integration of thin film wrinkling with all-solution processing methods such as electroless deposition that possess high degree of uniformity and continuity to create inexpensive and high quality yet structurally tunable electrodes.

Here we demonstrate that patterned wrinkled electrodes with tunable minimum feature sizes, topography, and porosity can be readily fabricated using all-solution-processing on shape memory polymer substrates. The resulting structurally tunable three-dimensional electrodes also exhibit a combination of useful functional properties including high surface area, good electrical conductivity, and significant enhancement in surface-enhanced Raman scattering signal, making them suitable for a range of chemical and bioanalytical sensing applications. In addition, given that these wrinkled electrodes are fabricated using a combination of inexpensive solution-phase processes – molecular self-assembly, colloidal nanoparticle seed layer deposition, electroless deposition – they do not rely on expensive instrumentation and can be applied to rapid prototyping and be extended to batch-based industry-scale manufacturing.

## 6.3 Experimental

### 6.3.1 Chemicals

(3-Aminopropyl) triethoxysilane (APTES, 99%), 4-Mercaptopyridine (4Mpy, 95%), hydrogen tetrachloroaurate(III) trihydrate ($HAuCl_4 \cdot 3H_2O$, > 99.9%), and hydrogen peroxide ($H_2O_2$, 30%) were purchased from Sigma-Aldrich (St. Louis, Missouri). Sulfuric acid ($H_2SO_4$) was purchased from Calden (Georgetown, Ontario). All reagents were of analytical grade and were used without further purification. Milli-Q grade water (18.2 M Ω) was used to prepare all solutions.

### 6.3.2 Polystyrene Substrate Preparation

Pre-stressed polystyrene (PS) substrates (Graphix Shrink Film, Graphix, Maple Heights, Ohio) were cut into the desired shape using the Robo Pro CE5000- 40-CRP cutter (Graphtec America Inc., Irvine, CA). The PS substrates were cleaned with 2-propanol, DI water, and then dried with air. The substrates were treated with air plasma in an Expanded Plasma Cleaner (Harrick Plasma) on HIGH RF power setting for 60 seconds, oxidizing the surface of the substrate. Then, the substrates were immersed in a 10% APTES solution in an Incubating Mini Shaker (VWR International) for 16 hours at 120 rpm and at room temperature. Following silanization, the substrates were sonicated in DI $H_2O$ for 10 minutes, rinsed and dried. The desired electrode layout was designed in Adobe Illustrator and cut into vinyl (FDC 4304, FDC graphic films, South Bend, Indiana) using the Robo Pro CE5000- 40-CRP vinyl cutter. The masks were applied to the silanized PS substrates.

### 6.3.3 Gold Nanoparticle Synthesis and Deposition

Gold nanoparticles (Au NPs) were synthesized according to Preparation 1[250] and were refrigerated until used. The masked PS substrates were then fixed in petri dishes using double sided tape and covered in a solution of Au NPs for 16 hours.

### 6.3.4 Electroless Deposition

The Au NP covered PS substrates were placed in a 5 ml solution of 0.1% $HAuCl_4$ solution on a shaker at 250 rpm at room temperature. Then, 250 µL of 30% $H_2O_2$ was added to the solution, resulting in Au deposition. Bubbles forming on the edges of the vinyl mask were eliminated using a pipette tip. The vinyl mask was removed after deposition and the devices were then placed in an oven (Model: 664, Fisher Scientific, Marietta, OH) at 160˚C to shrink for 3 minutes.

### 6.3.5 Sheet Resistance Measurements

Sheet resistance values of both shrunk and unshrunk electroless deposited electrodes on PS were measured with the van der Pauw method using the HL5500PC- Hall effect measurement system with a HL5500 buffer amplifier (Nanometrics, Milpitas, California). A Greek cross electrode geometry was used with a length and height of 10 mm before shrinking, and width of 3 mm.

### 6.3.6 Adhesion Tests

Adhesion was assessed using the scotch tape peel test with the Instron 4411 (Instron Corporation, Norwood, MA, USA) machine. Tape was applied to the surface of the electrodes and peeled away using a constant velocity of 20 mm/min over multiple devices (n=3).

### 6.3.7 Roughness and Peak-to-Valley Measurements

The roughness ($R_a$) and peak-to-valley (PV) values of the wrinkled electrode devices were measured using a Zygo NewView 5000 white light interferometer (Zygo Corporation, Middlefield, CT) over multiple areas per device (n>3) and over multiple devices (n=3). Measurements were obtained with 10× and 2× image zoom setting (360 µm × 270 µm field of view) using a charge couple camera with an imaging pixel size of 11.2 µm. Data filtering and analysis was performed with MetroPro. A fast Fourier transform (FFT) high pass filter was applied, using a cut-off frequency 183.35 $mm^{-1}$, and spikes with height values above 10 × RMS (root mean square) were removed to eliminate any variations due to the unevenness of the substrate or any surface contaminants, respectively.

### 6.3.8 Electrochemistry

Electrochemistry was performed using a CHI 660D electrochemical workstation (CH Instrument, Austin, Texas) and a standard three-electrode set-up. The electrochemical system consisted of an Ag/AgCl reference electrode, a platinum wire counter electrode, and the all-solution-processed Au electrode as the working electrode. Electrodes were electrochemically polished prior to use by performing cyclic voltammetry (CV) between 0 and 1.5 V for 80 cycles at 0.1 V/s in 0.05M $H_2SO_4$. Electrochemical surface area measurements were performed by doing another 3 cycles of cyclic voltammetry using the same parameter but at 0.05 V/s. The peaks for the reduction portion of the resulting cyclic voltammograms were integrated to obtain the electric charge involved in the redox process and divided by the surface charge density of Au (386 μC/cm$^2$)[168] to acquire the values of surface area.

### 6.3.9 Raman Measurements

Raman measurements were performed using Renishaw inVia Raman Microscope, with a 632.8 nm HeNe laser at 5% power (25 mW) and 50x objective. Measurements were acquired using 10 s exposures and accumulated 5 times. Au film samples were incubated with 4Mpy for an hour at room temperature, rinsed with DI $H_2O$, and dried. Measurements were performed on samples prior to incubation with 4Mpy, after incubation with 4Mpy, and after shrinking. The background fluorescence signal was subtracted from the spectra and a fourth order polynomial baseline subtraction was performed. The enhancement factor (EF) of the 1 min-AS films was calculated with respect to the 20 min-BS films using Equation 1:

$$EF= [(I_{1\text{ min-AS}})(C_{20\text{ min-BS}})]/ [(I_{20\text{ min-BS}})(C_{1\text{ min-AS}})] \quad \text{(Equation 1)}$$

Where $I$ is the intensity of the 1090 cm$^{-1}$ peak, which is associated with ring stretching/ breathing and C-S stretching, and $C$ is the concentration of 4Mpy the substrate is incubated with.

## 6.4 Results and Discussion

Figure 6.1 **(a-b)** schematically illustrates the all-solution-based fabrication process used to produce wrinkled gold structures to be used as electrodes or other sensing devices. Gold (Au) was chosen for this study due to its importance in chemical and biological sensing owed to its high conductivity, nobility/chemical inertness, and ability to be functionalized with thiol-terminated biorecognition molecules.[251], [252] In this method, a biaxially pre-stressed commercially-available polystyrene (PS) substrate is treated with air plasma (Figure 6.1 (a)(i)) for surface activation and subsequent silanization (the surface chemistry of devices is shown in Figure 6.1 (b)). The activated PS substrate is incubated in a 10% (3-aminopropyl) triethoxysilane (APTES) solution (Figure 6.1 (a)(ii)), which forms a molecular linking layer for connecting citrate-stabilized gold nanoparticles (~12 nm diameter) to the polystyrene substrate through electrostatic interactions (Figure 6.1 (b)). An adhesive vinyl shadow mask, patterned through xurography, is then bound to the substrate (Figure 6.1 (a)(iii)). Then, the masked PS substrates are incubated in an Au nanoparticle (Au NP) solution to form a thin, uniform seed layer of Au NPs on the substrate (Figure 6.1 (a)(iv), Figure 6.1 (b)). In order to create high conductivity electrodes, electroless deposition is subsequently performed on the seed layer to produce a continuous gold film. (Figure 6.1 (a)(v)).[253] The PS substrate modified with a Au NP seed layer is immersed in a cyanide-free and environmentally-friendly plating solution containing the gold precursor (chloroauric acid ($HAuCl_4$)) and the reducing agent (hydrogen peroxide ($H_2O_2$)). The monolayer of Au NPs on the PS acts as the nucleation site for the growth and formation of the continuous Au layer (Figure 6.1 b)), and is expected to minimize the reduction of gold within the bulk solution. After the continuous Au layer is formed, the vinyl shadow mask is removed (Figure 6.1 (a)(vi)), exposing the electrode geometry. The pre-stressed polymer substrate then undergoes a thermally induced shrinking process by heating it in an oven at 160˚C,

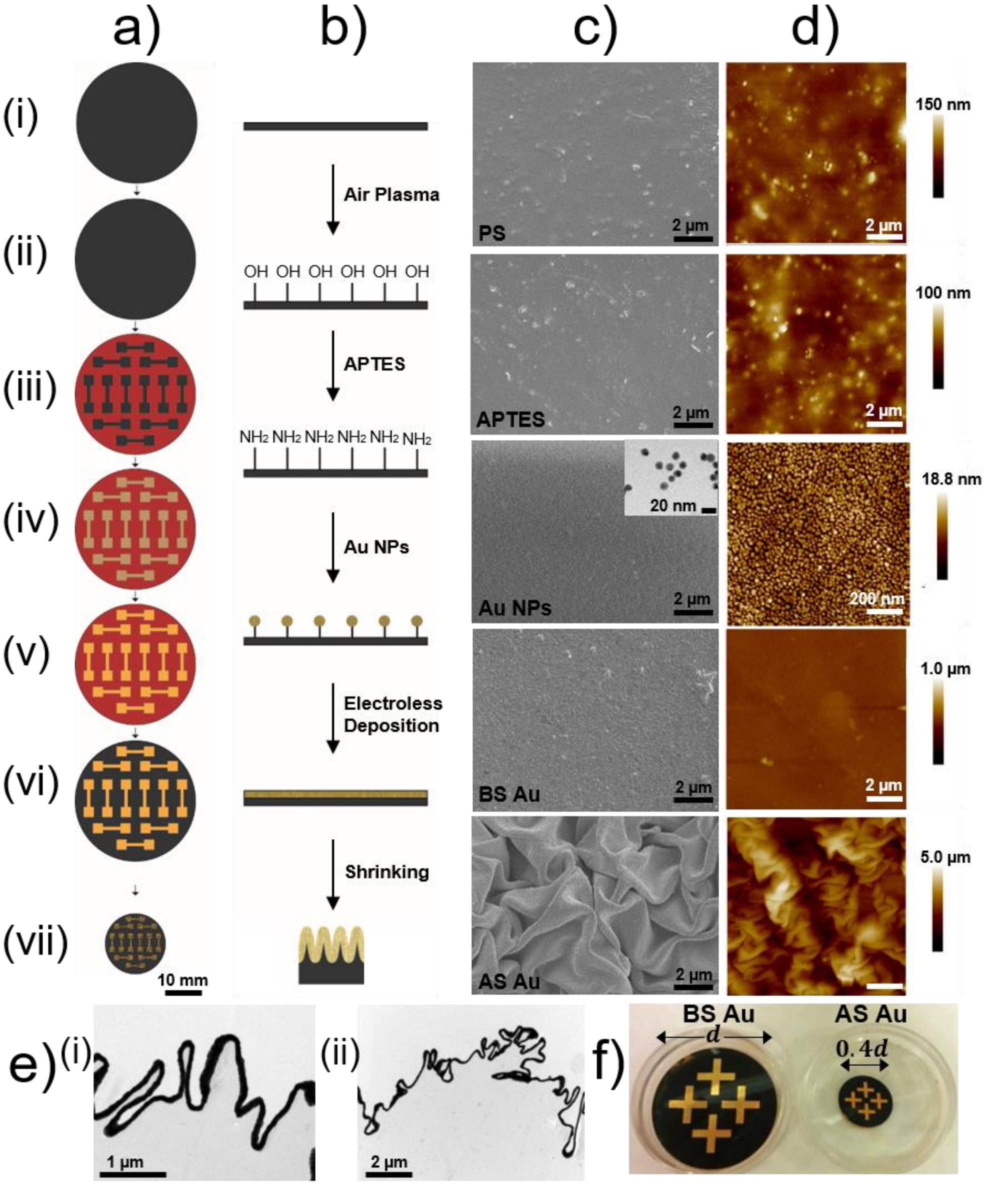

Figure 6.1 Fabrication of the all-solution-processed wrinkled films. a) Schematic of the top view fabrication process: i) Plasma cleaning pre-stressed PS substrate, ii) modifying the substrate with an amino-silane (APTES) layer, iii) masking the substrate with a xurography-patterned vinyl film, iv) creating a Au NPs seed layer, v) electroless deposition of Au, vi) mask removal, and vii) heating the device to create wrinkled electrode structures. b) Side view schematic with surface chemistry during the fabrication process. c) SEM images after each fabrication, inset of iv) displays TEM image of unbound Au NPs. d) AFM images after each fabrication step. e) TEM images of wrinkled film cross-sections showing the primary and secondary wrinkling at i) high and ii) low magnification. f) Photograph of all-solution-processed electrodes before shrinking (BS) and after shrinking (AS), *d* indicates the diameter of the device.

past the glass transition temperature for PS, for 3 minutes. Heating the pre-stressed PS over the glass transition temperature reduces the length and width of the substrate by more than 60% and increases its thickness by over 600%.[199] As the polymer substrate contracts, it exerts a compressive stress on the overlaying Au film, driving the gold film to buckle and wrinkle and causing the lateral dimensions of the gold patterns to be reduced by 60% (Figure 6.1 (a)(vii)).

Figure 6.1 (c-d) demonstrates the structural evolution of all-solution-processed gold films after each processing step using scanning electron microscopy (SEM) (Figure 6.1 (c)) and atomic force microscopy (AFM) (Figure 6.1 (d)). The Au NPs bind and form a uniform layer on the silanized PS substrate, as evidenced in the corresponding SEM image and AFM measurements. The subsequent electroless deposition forms a smooth layer of Au over the substrate. We hypothesized this smooth all-solution-processed gold layer to wrinkle similar to the previously reported sputtered films[128], [199] upon heating because of the mismatch between the elastic moduli of the stiff thin film and the compliant PS substrate. Following the heating of the pre-stressed PS substrate, we observed wrinkles that result in feature sizes in the nano/microscale and height variations in the micrometer scale. The high and low magnification TEM images of a cross-section of a wrinkled electrode (Figure 6.1 (e)) show the conformal interface between the Au layer and PS, as well as the primary (smaller) and secondary (larger) wrinkling along this interface. A photograph of devices before (BS) and after (AS) shrinking are displayed in Figure 6.1 (f). It is apparent that the after shrinking Au electrodes show the same electrode layout as the before shrinking Au electrodes; however, they appear miniaturized and show a darkened gold colour that is less reflective due to the wrinkled structuring of the electrodes (Figure 6.1 (f) and Supplementary Figure 6.1). Moreover, the shrinking occurs across the entire substrate, reducing the lateral dimensions of the device to 40% of their initial sizes.

The shrinking of the polymer substrate and the resulting wrinkled Au layer has several physical advantages over the planar before shrinking device, including a reduction in the lateral dimensions of the patterned Au film, structuring of the Au layer, and improved film-to-substrate adhesion. The lateral reduction in size allows for development of smaller electrode geometries and smaller device footprints. With this fabrication method, <100 µm line-and-space arrays could be produced, as well as 150 µm circular features. When a scotch tape adhesion test was performed on films before and after this shrinking process, it was observed that the Au layer partially peeled off prior to shrinking, but could not be removed after the shrinking and wrinkling process. This improved adhesion can be attributed to the effective anchoring of the Au film within the PS wrinkles, as observed in the cross-sectional TEM images.

The ability to structurally tune the newly developed all-solution-processed wrinkled film is highly desirable for optimizing the functional parameters of these materials.[33] To achieve tunability in minimum feature size, porosity, thickness, and

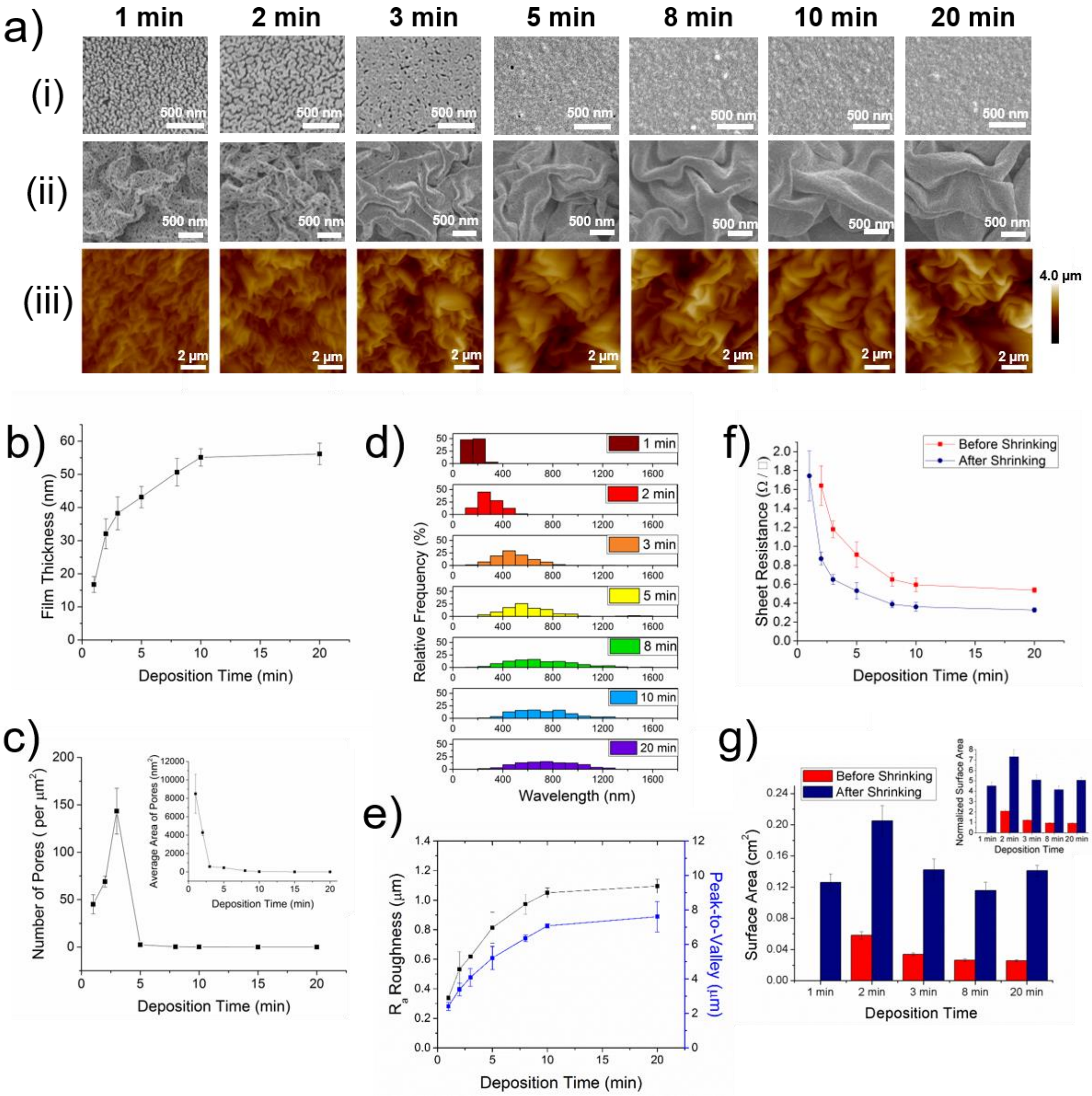

Figure 6.2 Characterization of structure and properties of Au films at different electroless deposition times. a) SEM images of films (i) before shrinking and (ii) after shrinking, as well as (iii) AFM images of wrinkled electrodes. b) AFM measured film thickness before shrinking. c) Estimation of pore frequency in film before shrinking, with the inset showing the average area of the pores. d) Relative frequency distributions of wrinkle wavelength, as estimated by SEM of uniaxially wrinkled devices. e) Electrode roughness ($R_a$) and peak-to-valley (PV) white light interferometry measurements. f) Sheet resistance of electrode devices before and after shrinking. g) Electrochemically determined surface area of electrode devices before and after shrinking. Inset displays the normalized surface area (electroactive surface area/ geometric surface area) to indicate how many times larger the electroactive surface area is compared to the geometric area.

topography, we investigated the structure of the all-solution-processed wrinkled films fabricated using different electroless deposition durations (Figure 6.2 a-e**)**. SEM images of the Au films before shrinking (Figure 6.2 (a)(i)) indicate that the film morphology strongly depends on the electroless deposition time. It was found that the film thickness increased with increasing deposition time (Figure 6.2b)), with a plateau at approximately 55 nm observed around 10 min. Moreover, the film porosity was strongly affected by deposition time. Discontinuous islands of gold can be observed after 1 min of electroless deposition, while the coalescence between these islands increases as the electroless deposition time increases until around 8 min, where a continuous gold film can be observed. Image analysis of these films (Figure 6.2 (c)) indicate that the density of pores increases between deposition times of 1 and 3 min, as the large pores between islands are split into multiple smaller pores (average size of pores shown in Figure 6.2 (c) inset), then decreases rapidly until 8 min.

It is evident that after shrinking, the wrinkle size and porosity are also dependant on the electroless deposition duration (Figure 6.2 (a)(ii)). Interestingly, an additional degree of tunability in material structure is observed through this newly-developed all-solution-processing method that was not previously reported with wrinkled PVD films. Thin films deposited at short electroless deposition durations demonstrating a non-continuous and porous structure are able to wrinkle and become more connected during the shrinking process. Based on the SEM images, the wrinkle sizes increase with increasing electroless deposition duration. To quantify the all-solution-processed wrinkle wavelengths and to compare these with the wavelength of PVD wrinkles, we also created uniaxial wrinkles by restricting the shrinking process to one axis (Supplementary Figure 6.2). The analysis of the relative frequency distributions of wrinkle wavelengths demonstrated that the wavelength distribution broadened and shifted toward larger values until 10 min. The direct dependence of wrinkle wavelength to film thickness is in agreement with theoretical models and experiments performed with PVD thin films.[119], [121], [127] When the average wrinkle wavelength is plotted against the average film thickness (Supplementary Figure 6.3), an increasing, but not perfectly linear trend is observed. Previous theoretical models indicate that the wrinkle wavelength is directly related to the cubic root of the ratio of the elastic moduli of the thin film and the substrate, suggesting that the mechanical properties of the film is also changing with varying electroless deposition times.

The AFM data demonstrates that the thin film topography is also tunable by varying the duration of electroless deposition before wrinkling. As the electroless deposition time is increased, we see a corresponding increase in topographical variation across the wrinkled films (Figure 6.2 (a) (iii)). The roughness of the surface of the wrinkled Au layer is also characterized using white light interferometry (Figure 6.2 (e)). With increasing deposition time, the surface roughness ($R_a$) and peak-to-valley (PV) variation increase rapidly until 10 min. Between 10 to 20 min, there is a smaller increase in the surface roughness and PV values. This is consistent with the finding that the film thickness plateaus after 10 min. of electroless deposition.

In order to study how the structural differences between electrodes translate into differences in their electrical properties, we performed four-point probe sheet resistance measurements before and after shrinking (Figure 6.2 (e)). It is evident that the sheet resistance of the electrodes, before and after shrinking, decreases rapidly as the deposition duration increases between 1 and 10 min, and then a slower decrease in sheet resistance is observed as the deposition duration increases past 10 min. The rapid decrease observed prior to 10 min is attributed to the filling of the porous structures and the increasing film thickness during this stage of deposition. Moreover, it is observed that the electrical properties of the electrodes are improved through the shrinking process at all deposition durations, as the sheet resistance is significantly lower after shrinking. The decrease in sheet resistance after shrinking can be attributed to the increased connectivity between adjacent folds and the increased overall conductor path thickness, as well as partially or fully connecting discontinuities in the porous film present at short deposition times. It should be noted that devices that were fabricated using 1 min of electroless deposition were not conductive enough to obtain sheet resistance values prior to shrinking, however the wrinkled electrodes at this deposition time did overcome the measuring threshold to obtain sheet resistance values. In addition, a comparison of all-solution-processed devices (8 min wrinkled, 0.39±0.04 Ω/□) to sputter coated devices (~50 nm wrinkled, 0.40±0.02 Ω/□) of approximately the same thickness was performed and the electroless deposited wrinkled devices of the same dimensions had approximately the same resistance of the sputter coated devices (Supplementary Figure 6.4). Overall, this solution processing fabrication method could produce devices with sheet resistances as low as 0.25 Ω/□.

High surface area electrodes are finding applications in a number of fields, ranging from biosensing[30], [254] to energy storage and conversion[255]. To assess the suitability of the all-solution-processed Au films for use as high surface area electrodes in electrochemical applications, we measured their electro-active surface areas (Figure 6.2 (g)). Electrodes deposited for 1 min, 2 min, 3 min, 8 min, and 20 min having the same geometric surface area (0.028 cm$^2$) were evaluated before and after shrinking. The electrochemically-measured surface areas of the electrodes deposited for 8 min and 20 min before shrinking were approximately equal to their projected surface area. However, the measured surface area of the 2 min and 3 min devices before shrinking were larger by 106% and 20%, respectively, compared to their geometric surface areas. This is attributed to the presence of the pores within the electrode film (Figure 6.2 (a)) at shorter deposition durations. The electroactive surface area of the 1 min before shrinking device could not be determined due to the lack of conductivity. All of the wrinkled electrodes showed significantly larger electroactive surface areas compared to their before shrinking counterparts for the same constrained area (0.028 cm$^2$). This is expected and consistent with previous results obtained using PVD films because the shrinking process wrinkles the electrode material into a fraction (~16 %)[199] of the original footprint. The 2 min electroless deposited device demonstrated the largest surface area after shrinking (0.204 cm$^2$) corresponding to a greater than 7 times enhancement compared to the geometric surface area. The decrease in surface area at 3 min (0.142 cm$^2$) and even further at 8 min (0.116 cm$^2$) compared to the 2 min devices is due to the partial and complete filling of the porous features within the Au films as observed in the SEM images (Figure 6.2 (a)). The surface area of the 20 min after shrinking devices was larger than the 8 min after shrinking devices, which is hypothesized to be related to the more separated and accessible wrinkles present in the 20 min devices. It is clear that the electroactive surface areas of the all-solution-processed electrodes can be precisely controlled by tuning the thin film porosity and wrinkle sizes, which is enabled by varying the duration of electroless deposition before electrode wrinkling.

In addition to their role as electrodes, nanostructured metal films play an important role as substrates for enabling surface-enhanced Raman spectroscopy (SERS).[47], [256] Due to the presence of nano-gaps, sharp edges, and sharp corners on nanostructured noble metal substrates, very large electromagnetic (EM) fields can be produced by exciting the surface plasmon resonance at the surfaces of substrates with light.[49], [257], [258] As a proof-of-concept SERS sensor, the Au films at different electroless deposition times (1 min, 2 min, 8 min, and 20 min) were applied as substrates for the sensing of 4-mercaptopyridine (4Mpy) with the spectra measured before and after shrinking (Figure 6.3 (a)). The 4Mpy is incubated on the before shrinking substrates, and it is evident from the SERS spectra that the intensity of spectral features becomes larger after shrinking. This can be attributed to the sharp Au film features that are produced through the wrinkling process, as well as the increase in the surface density of the analyte as the device footprint is reduced. Although the wrinkling enhances the Raman signal for all four deposition times, the enhancement is more significant for the continuous films (8 min and 20 min), where the peaks are likely due to the structuring of the wrinkles creating EM hot spots. On the other hand, the porous films have nanostructures that can contribute

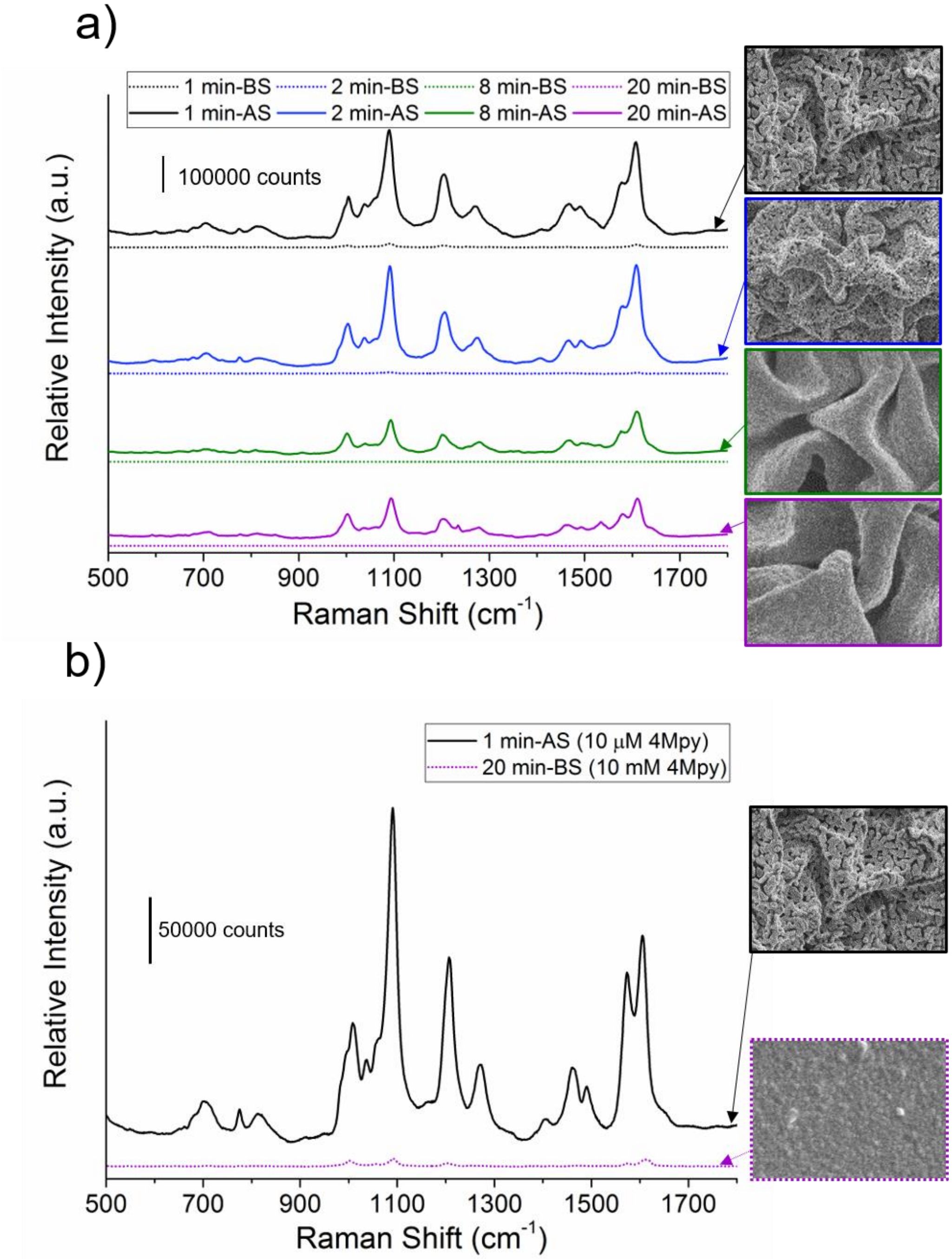

Figure 6.3 Application of Au films as surface enhanced Raman spectroscopy (SERS) substrates. a) SERS spectra of Au films at different electroless deposition times before shrinking (BS) and after shrinking (AS) after 1 hour incubation with 1 mM 4Mpy. b) SERS spectra of after 1 hour incubation of 20 min-BS with 10 mM 4Mpy and 1 min-AS with 10 µM 4Mpy used to calculate the enhancement factor.

to the Raman signal enhancement prior to wrinkling, as evidenced by the visible peaks in their spectra, and provide a boost in the signal by 4.2 and 9.4 times after shrinking (adjusting for the surface area increase) for the 1 min and 2 min, respectively. The wrinkled 1 min and 2 min devices showed significantly higher intensity spectra (2.5 to 3.3 times larger) compared to the wrinkled continuous films (8 min and 20 min) after shrinking, likely due to the high density of pores and nano-gaps within the wrinkled film that could contribute to the EM field enhancement and their higher surface areas. Due to the very low peaks (not statistically different than the background noise) of the continuous planar films, the enhancement factor of the porous wrinkled films compared to planar gold films was determined by comparing 1 min substrates after shrinking incubated with 10 µM 4Mpy against 20 min substrates before shrinking with 10 mM 4Mpy (Figure 6.3 (b)). The 1090 $cm^{-1}$ peak, associated with ring stretching/ breathing and C-S stretching, was used to calculate the enhancement factor (equation in Supporting Information). The 1 min and wrinkled substrates were able to enhance the signal over planar Au devices (20 min-BS) by $4.24\times10^4$. Accounting for the larger surface area of the 1 min wrinkled device over the planar device, the enhancement in the Raman signal due to the structure of the substrate is $8.54\times10^3$. Evidently, the structural tunability of these solution-processed metallic film allows them to be extended to applications where nanostructuring and high surface area are crucial to sensor performance.

## 6.5 Conclusions

In summary, we have developed a rapid all-solution-processing methods by combining electroless deposition and thin film wrinkling on shrink-memory polymer substrates.

Through this work, we have: (1) demonstrated the tunability of the resulting Au film surface porosity, topography and morphology, through the electroless deposition parameter manipulation and shrink-induced wrinkling; (2) characterized the effect of the structural control of the metallic film on important functional parameters, such as the conductance and electrochemically active surface area; and (3) translated the structural control to functional optimization of substrates for surface enhanced Raman spectroscopy. As a result, we have discovered that electroless deposition duration is a key parameter for creating functional three-dimensional wrinkled materials that are optimized in terms of surface area, morphology, conductance, and SERS enhancement for use in application-specific devices. With the speed, ease, and low cost per surface area (<\$ 0.01/cm$^2$) that these functional conductive films are fabricated, we foresee them being applicable to many electrical, electrochemical, and optical applications.

## 6.6 Acknowledgements

The financial support for this work was provided by the Natural Sciences and Engineering Research Council of Canada (NSERC). The electron microscopy was carried out at the Canadian Centre for Electron Microscopy (CCEM), a national facility supported by the NSERC and McMaster University.

## 6.7 Chapter 6: Supplementary Information

### DEVELOPMENT OF TUNABLE POROUS AND NON-POROUS THREE-DIMENSIONAL ALL-SOLUTION-PROCESSED WRINKLED FILMS ON SHAPE MEMORY POLYMERS

**Authors:** Christine Gabardo, Robert Chris Adams-McGavin, Barnabas Fung, Eric Mahoney, Qiyin Fang, and Leyla Soleymani

**Publication:** To be submitted in 2016.

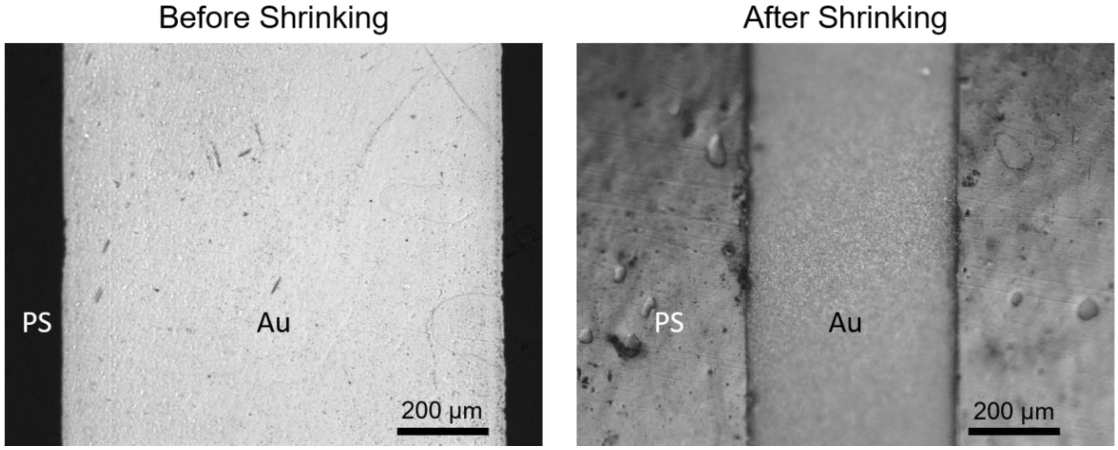

Supplementary Figure 6.1 Patterned Au film line before and after shrinking to demonstrate the miniaturization of the pattern, as well as the texturing of the Au layer after shrinking.

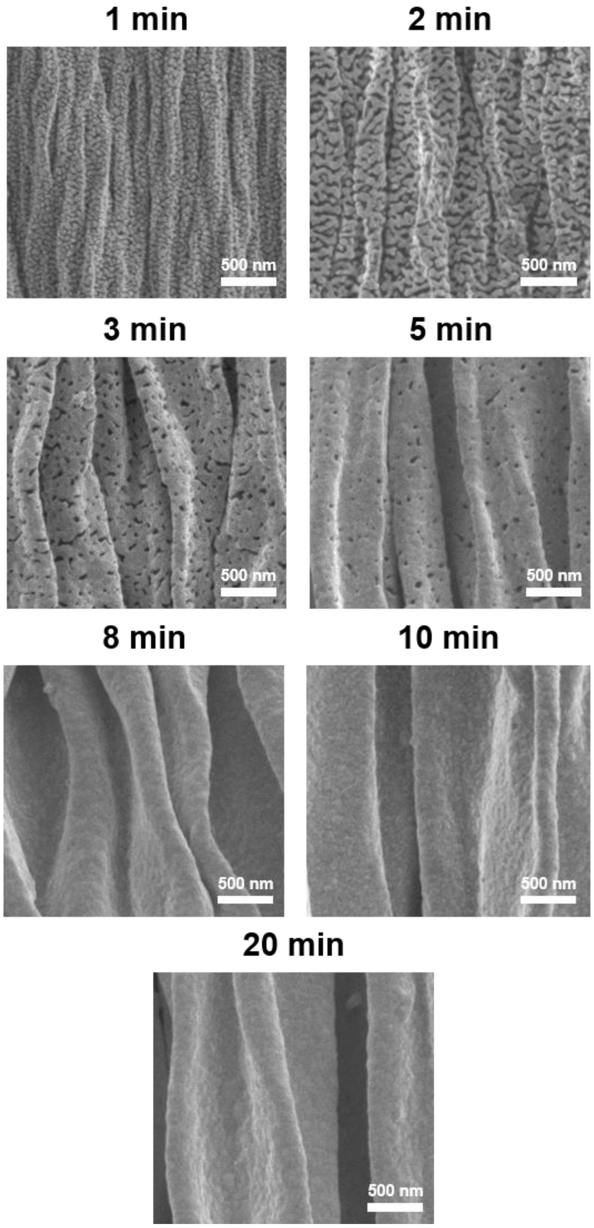

Supplementary Figure 6.2 SEM images of uniaxial wrinkled Au films at different electroless deposition times.

.

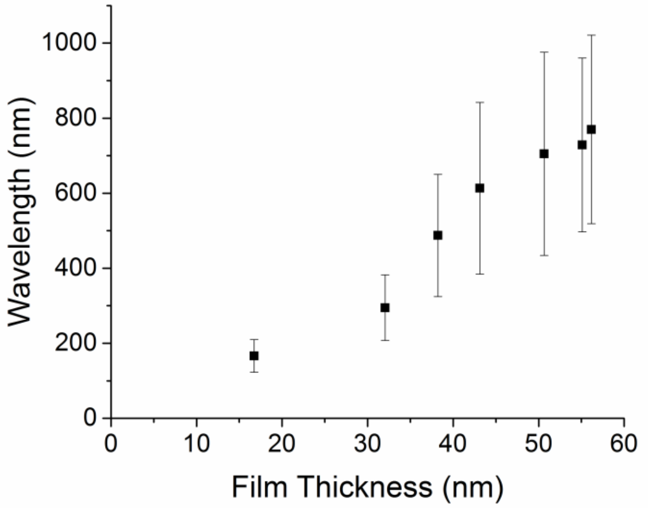

Supplementary Figure 6.3 Electroless Au film thickness before shrinking and the resulting wavelength after shrinking.

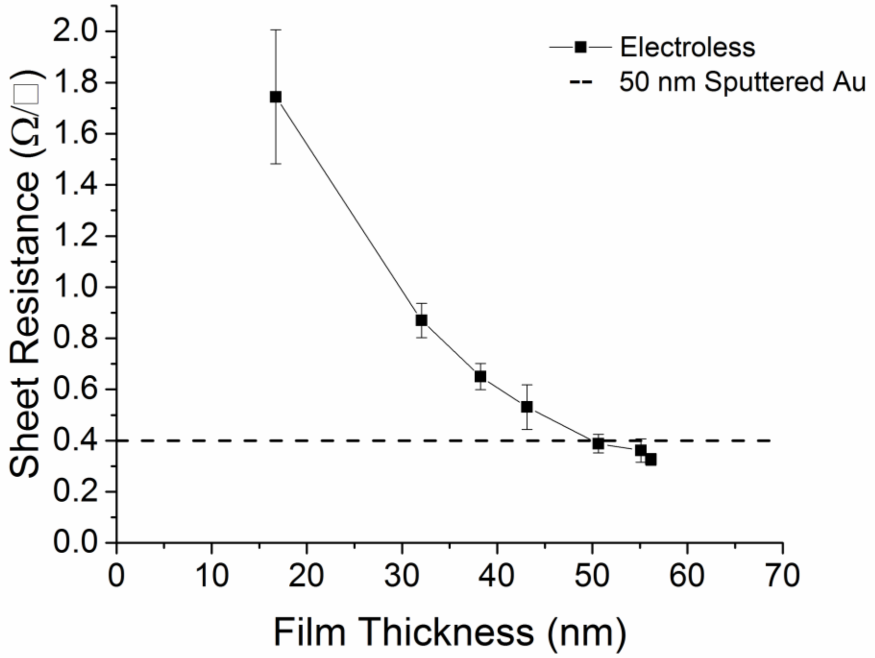

Supplementary Figure 6.4 Sheet resistance measurements of electroless deposited films with respect to film thickness compared to 50 nm sputtered Au film.

# Chapter 7 Programmable Wrinkling of Self-Assembled Nanoparticle Films on Shape Memory Polymers

## Chapter Introduction (Objectives B, C, and D)

The direct wrinkling of nanomaterials to produce functional structured surfaces may hold the key to producing and tuning unique structures/ features not seen with continuous thin film wrinkling on shape memory polymer substrates. This chapter expands on the all-solution processing method presented in Chapter 6, to deposit metallic thin films on pre-stressed polymer substrates for wrinkled multi-scale structure fabrication. Rather than utilizing electroless deposition to grow a connecting layer of gold, the gold nanoparticles are directly wrinkled after self-assembly on the substrate to engineer wrinkled metallic surfaces. An investigation into tuning the wrinkled structure is undertaken and parameters, such as the number of strained axes, the diameter of the gold nanoparticles, the number of nanoparticle layers, and the density of nanoparticles on the surface of the substrate, are used to control the resulting structures. An in-depth study of the various wrinkled structures is performed using scanning electron microscopy and transmission electron microscopy, and the characteristic periodicity of the structures is extracted for the various diameters of nanoparticles and the multi-layer devices to gain a deeper understanding of the mechanical properties of these films. We observe wavelengths that span sub-100 nm, some of the lowest reported in the literature, to several hundred nm. It is found that changing the parameters of the nanoparticles alters not only the wrinkle structures, but also the intra-wrinkle structuring. The structural tuning of these structures translated to functional tuning as they are applied as substrates for the SERS detection of a chemical analyte.

**Authors:** Christine Gabardo, Jie Yang, Nathaniel Smith, Robert Chris Adams-McGavin, and Leyla Soleymani

**Publication:** Submitted to ACS Nano July 2016

### 7.1 Abstract

Hierarchically structured materials, inspired by sophisticated structures found in nature, are finding increasing applications in a variety of fields. Here we describe the fabrication of wrinkled gold nanoparticle films, which leverage the structural tunability of gold nanoparticles to program the wavelength and amplitude of gold wrinkles. We have carefully examined the structural evolution and tuning of these wrinkled surfaces through varying nanoparticle parameters (diameter, number of layers, density) and substrate parameters (number of axes constrained during wrinkling) through scanning electron microscopy and cross-sectional transmission electron microscopy. It is found that nanoparticle layers of sufficient density are required to obtain periodical wrinkled structures. It was also found that tuning the nanoparticle diameter and number of layers can be used to program the wrinkle wavelength and amplitude by changing the film thickness and mechanical properties. This dual degree of tunability, not previously seen with continuous films, allows us to develop one of the smallest wrinkles developed to date with tunability in the sub-100 nm regime. The effect of the induced structural tunability on the enhancement of the intensity of the 4-mercaptopyridine Raman spectra is also studied through the application of these devices as substrates for surface-enhanced Raman spectroscopy (SERS), where wrinkling proves to be an effective method for

enhancing the SERS signal in cases where there is an inherently low density of gold nanoparticles.

### 7.2 Introduction

Multiscale materials that combine building blocks in a wide range of length-scales for addressing specific functional demands occur naturally in countless places in our environment.[259] Inspired by nature, materials scientists and engineers have created hierarchically-organized and multi-scale materials for use in applications ranging from energy[260], [261] to therapeutics.[262], [263] Integrating a range of materials with different dimensionality, morphology and length-scale into three-dimensional architectures is often a complex and multi-step process. The complexity in fabricating multi-scale and hierarchical materials is related to the fact that the widely used top-down and bottom-up fabrication techniques belonging to the broad categories of machining, lithography, printing, and self-assembly are often optimal for creating structures over a narrow length-scale and they become slow, expensive, complex, inefficient or ineffective over other length-scales.[264] Given the better understanding of the correlation between the structural and functional parameters of materials over the past few decades, there is a growing interest in simple, rapid, and inexpensive methods for creating multi-scale materials with high degree of structural tunability. The ability to rapidly and easily create multi-scale materials will enable scientists to further improve the understanding between materials structure and function, and will allow engineers to rapidly prototype application-specific devices based on these materials.

Wrinkling of thin films has emerged as a facile method for creating materials with features tunable in the micro/nanoscale, without the need for lithography.[116] Wrinkling occurs when stiff films or sheets, coupled to compliant substrates, are compressed in the direction parallel to the surface and buckle in the direction normal to the surface relieving the mechanical stress.[265] The resulting wrinkle amplitude and wavelength is dependent on the mechanical properties of the film and the substrate, the thickness of the film, and the amount of induced strain.[116], [119], [121], [124] By exploring this parameter space, the structure and feature sizes of these wrinkled films are precisely tuned and optimized for integration into functional devices.[128], [199]

The majority of the previously reported wrinkled structures have been fabricated through the deposition of thin films, by physical vapour deposition, onto pre-stressed shape memory thermoplastic substrates. Shape memory polymers are able to recover their original shape after an external stimulus, such as heat or chemicals, is applied and offer an advantage in surface patterning, in particular wrinkling, due to the flexibility and convenience of these substrates.[266], [267] Upon heating these systems over the glass transition temperature of the biaxially strained thermoplastic, the shape memory substrates shrink in their lateral dimensions, reducing their effective footprint and compressing the thin film on the surface. The compressive force exerted on the thin film during the shrinking process results in buckling of the film and the production of micro/nanoscale wrinkles. This shrinking process has been also combined with other patterning methods to integrate micro/nanoscale wrinkles into devices having micro/millimeter scale patterns.[221]–[223] The structures fabricated using these methods have been the subject of intense investigations[128], [199] and have been applied to various areas including biological sample processing;[222], [223] electrochemical,[221] fluorescence,[139], [140] and surface enhanced Raman spectroscopy-based sensing;[49] fabricating superhydrophobic surfaces;[147] and photovoltaic devices.[268]

One drawback of the existing methods for creating multi-length-scale wrinkled materials is that while these methods – based on physical vapour deposition and patterning – are suitable for engineering hierarchical materials with minimum feature sizes in the hundreds of nanometer length-scale, they are not suitable for creating materials architectures controllable in the sub-100 nm range. To overcome this issue, we sought to investigate the effect of wrinkling on self-assembled nanoparticles deposited on shape memory polymers. We hypothesized that (1) self-assembled nanoparticles of sufficient surface density would wrinkle similar to continuous films as previously demonstrated using nanoparticles embedded into polymer substrates using spray coating[248]; and, (2) the nanoparticle size would play a dual role in tuning the materials structure: it can be used to tune both the wrinkle size and the intra-wrinkle structure. To validate this hypothesis and to create functional wrinkled structures using self-assembled nanoparticles, we studied the structural evolution of wrinkles created using nanoparticles of varying sizes, densities, and number of layers and investigated their applicability to surface-enhanced Raman spectroscopy.

## 7.3 Experimental

### 7.3.1 Reagents

(3-Aminopropyl)triethoxysilane ($H_2N(CH_2)_3Si(OC_2H_5)_3$), trisodium citrate dihydrate ($HOC(COONa)(CH_2COONa)_2 \cdot 2H_2O$), hydrogen tetrachloroaurate(III) trihydrate ($HAuCl_4 \cdot 3H2O$, > 99.9%), 4-mercatopyridine ($C_5H_5NS$, 95%) were purchased from Sigma-Aldrich (St. Louis, Missouri). All reagents were of analytical grade and were used without further purification. Milli-Q grade water (18.2 M Ω) was used to prepare all solutions.

### 7.3.2 Gold Nanoparticle Synthesis

Au NPs were synthesized according to a protocol described by Grabar et al.[250] Briefly, 1 mM $HAuCl_4$ was brought to a rolling boil with vigorous stirring, then 38.8 mM trisodium citrate (one tenth of the $HAuCl_4$ volume) was added. Boiling was continued for 10 min with stirring, and then the stirring was continued for an additional 15 minutes without heat at room temperature. We also observed that resulting solution of colloidal nanoparticles had an absorption maximum at 520 nm and were approximately 12 nm in diameter.

To produce the larger diameter Au NPs, the ~12 nm particles were used as seeds in a seeded growth synthesis.[269] Additional gold precursor was added to the colloidal solution heated to 90°C as additional growth steps. After these growth steps, the solution was diluted and additional trisodium citrate was added to produce the next size generation of Au NPs. The generations that were used for fabricating wrinkled surfaces were the seeds (g0) (~12 nm), g1+ 2ml ($HAuCl_4$) (~18 nm), and g2+2ml (~36 nm).[269]

Transmission electron microscopy (TEM) was used to assess the size of the nanoparticle diameters (n>50) in all cases.

### 7.3.3 Wrinkled Device Fabrication

Pre-stressed polystyrene (PS) substrates (Graphix Shrink Film, Graphix, Maple Heights, Ohio) were cleaned with isopropanol, DI water, and then dried with air. The substrates were treated with air plasma in an Expanded Plasma Cleaner (Harrick Plasma) on HIGH RF power setting for 60 seconds. Then, the substrates were immersed in a 10% APTES solution for 16 hours with agitation at 120 rpm and at room temperature. Following silanization, the substrates were sonicated in DI water for 10 minutes, rinsed and dried. These substrates could be stored at room temperature for several weeks without loss of activity. The silanized substrates were immersed in a colloidal solution of Au NPs overnight to form the skin layer. Heat treatment and shrinking of the devices was performed by placing the devices in an oven (Model: 664, Fisher Scientific, Marietta, OH) at 160˚C to shrink for 3 minutes. To create uniaxially aligned wrinkles, the device was constrained on opposite sides onto a glass slide using binder clips. Biaxial wrinkles were created by heating the device on a glass slide without any physical constraint.

In the case of the multilayer Au NP devices, after the formation of the first layer of Au NPs, the substrates were incubated in a 10% APTES aqueous solution for 12 hours. This was followed by the immersion in a colloidal solution of Au NPs for another 12 hours to form the next layer. This layer-by-layer process was repeated until the desired number of layers was achieved. These devices were wrinkled the same manner as the single layer devices.

### 7.3.4 Wrinkled Surface Characterization

The wrinkled surfaces were characterized using SEM, AFM, and TEM. SEM images of the gold films before and after shrinking were obtained using a JEOL JSM-7000S scanning electron microscope with an accelerating voltage of 2 kV, working distance of 6 mm, and low probe current. Wavelength data was extracted using Image J. TEM imaging was performed on cross-sections of the wrinkled devices using the JEOL 2010F. These devices were embedded and sectioned by microtome prior to imaging.

### 7.3.5 Surface Enhanced Raman Spectroscopy (SERS):

SERS data was obtained with a Renishaw inVia Raman Microscope (Renishaw, UK) using 632.8 nm HeNe laser excitation source (500 mW). The Au NP substrates with different wrinkle morphologies were washed with DI water and then incubated in a 4 mM aqueous 4-mercaptopyridine (Sigma-Aldrich, St. Louis, Missouri) solution for 1 h. The incubated substrates were rinsed with DI water, and dried with a stream of air. Spectra were collected using 5% power, 10 s exposures, 5 accumulations, and using the 50x objective. The enhancement factor (EF) of films was calculated with respect to the sputtered 100 nm Au planar films using Equation 1:

$$EF= [(I_{\text{Au NP film}})(C_{\text{Sputtered}})]/ [(I_{\text{Au NP film}})(C_{\text{Sputtered}})] \qquad \text{(Equation 1)}$$

Where $I$ is the intensity of the 1090 $cm^{-1}$ peak, which is associated with ring stretching/ breathing and C-S stretching, and $C$ is the concentration of 4Mpy.

## 7.4 Results and Discussion

In order to create wrinkled gold nanoparticle layers, we developed a strategy for the layer-by-layer assembly of gold nanoparticles onto shape memory polymers. This process involved activating the shape memory polystyrene (PS) substrate by plasma treatment, depositing an amino silane molecular linker layer, and layer-by-layer assembly of gold nanoparticles (Au NPs) (Figure 7.1 (a)). The amino silane ((3-Aminopropyl)triethoxysilane (APTES)) was used to link the substrate to Au NPs through the chemical reaction between its silane terminus and the hydroxyl groups on the plasma treated substrate, and the electrostatic interactions between its amine terminus and citrate-stabilized Au NPs.[270] The PS substrate was heated over its glass transition temperature (Tg≈103°C, as previously determined by differential scanning calorimetry of shape memory PS substrates of the same commercially available brand[271]) at 160°C for 3 min to cause it to shrink and induce a mechanical compression on the Au NP film, due to the thermal expansion mismatch between the soft polymer substrate and the stiffer Au NP film layer. We expected this mechanical compression to be relieved through the buckling of the film and result in a wrinkled Au NP surface. The commercially available PS substrate used here shrinks in two dimensions (with a strain of 40%) and it expands in one dimension. Throughout this paper, we study the structural evolution of uniaxial and biaxial wrinkles. To examine the uniaxial wrinkling process, we physically constrained the PS substrate to shrink in a single direction, and to obtain biaxial wrinkling we left both lateral axes unconstrained (Figure 7.1 (b)).

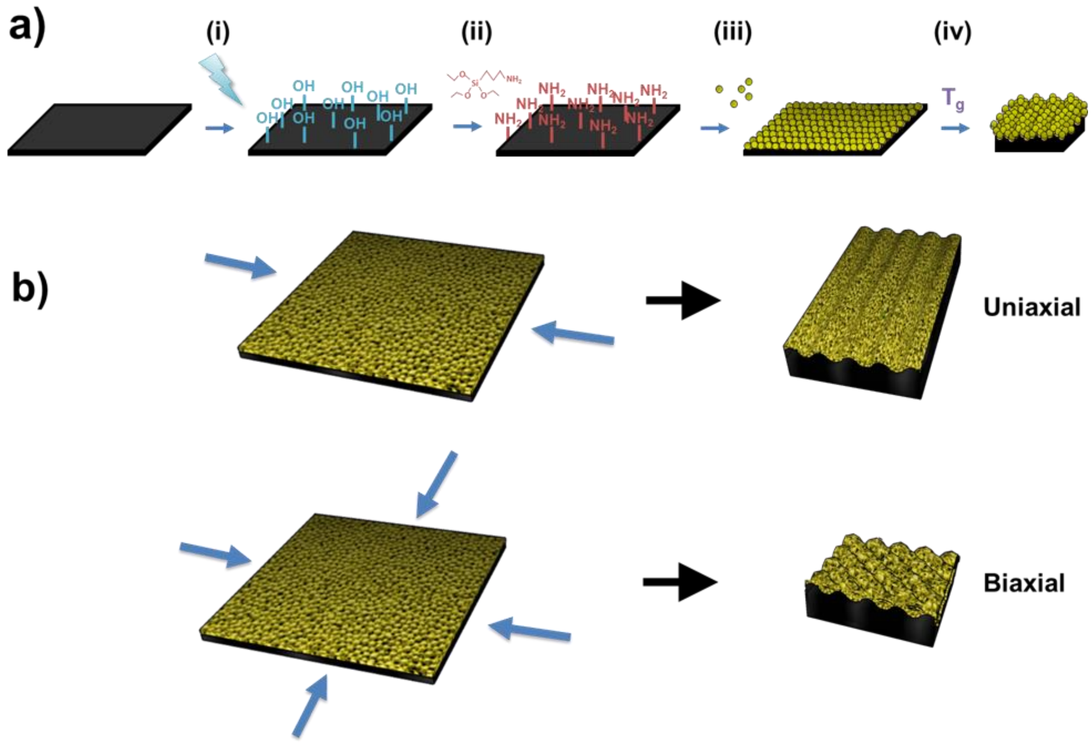

Figure 7.1 Schematics of the wrinkled Au NP device fabrication process (a) Fabrication steps: (i) PS is treated with air plasma, (ii) activated PS is silanized with APTES, (iii) Au NPs are immobilized onto the silanized PS, (iv) the device is heated to over the glass transition temperature (Tg) of polystyrene to induce shrinking and wrinkling. (b) Schematics of uniaxial (top) and biaxial (bottom) wrinkling given physical constraints during shrinking.

To explore the wrinkling behaviour of self-assembled Au NP (~36 nm in diameter) layers deposited on PS substrates, we investigated their surface structure before and after biaxial shrinking using scanning electron microscopy (SEM) (Figure 7.2 (a) and (b)). Various incubation times (0 min, 0.5 min, 3 min, 30 min, 60 min, and 960 min) were studied to determine the effect of Au NP surface density on the morphology of the resulting wrinkled layer when subjected to biaxial shrinking. It was observed in the before shrinking SEM images that the fraction of the PS surface covered in Au NPs increased with increasing the incubation time, with both the density increasing (percentage displayed in Figure 7.2 (a)) and the inter-particle separation decreasing. Evaluation of the SEM images after shrinking indicates (Figure 7.2 (b)) that two classes of wrinkles are present on PS substrates: at low Au NP densities, uniaxially-aligned wrinkles are observed, and at higher Au NP densities, there is a shift in the morphology of these APTES/Au NP composite wrinkles from uniaxial towards biaxial wrinkles. Interestingly, it is evident that the wrinkle morphology after biaxial shrinking is greatly influenced by the wrinkling of the underlying APTES layer on the surface at low Au NP densities (0-30 min), and the observed uniaxial wrinkling can be attributed to the wrinkling of the APTES layer. Fully-evolved biaxial wrinkles occur when the Au NP surface coverage of the APTES-treated PS reaches a sufficient value (between 13-22% or 30-60 min). While the minimum feature sizes of the wrinkles appear to be similar between 60 min and 960 min incubation times, the morphology of the 960 min wrinkles appear to be more distinct, likely due to the larger variations in the wrinkle heights or amplitudes.[272] We hypothesize that increasing the deposition time, and consequently increasing the Au NP density across the PS, between 60 to 960 min increases the elastic modulus of the film and lowers the resulting critical strain needed to induce wrinkling.[127] A lower critical strain leads to larger amplitude wrinkles, as the amplitude is related to the difference between the applied strain and the critical strain.[127] Comparing the wrinkled nanoparticle and sputtered gold films (Figure 7.2 (c)), it is clear that nanoparticles films of sufficient surface density will wrinkle with a morphology similar to continuous sputtered thin films. However, the wrinkled nanoparticle films offer an additional level of structural hierarchy due to the presence of their nanoparticle building blocks. It should be noted that although Au NPs were employed as the film layer in this system, wrinkling of other types of nanomaterial film layers, such as carbon nanotubes[273], [274] have been previously demonstrated. We suspect that the fabrication method presented here can be extended to other nanomaterials systems, provided that the nanomaterial film has sufficient coverage of and adhesion to the shape memory substrate (chemical linker may have to be altered), has the appropriate mechanical stiffness, and has a melting temperature above the Tg of the shape memory polymer substrate.

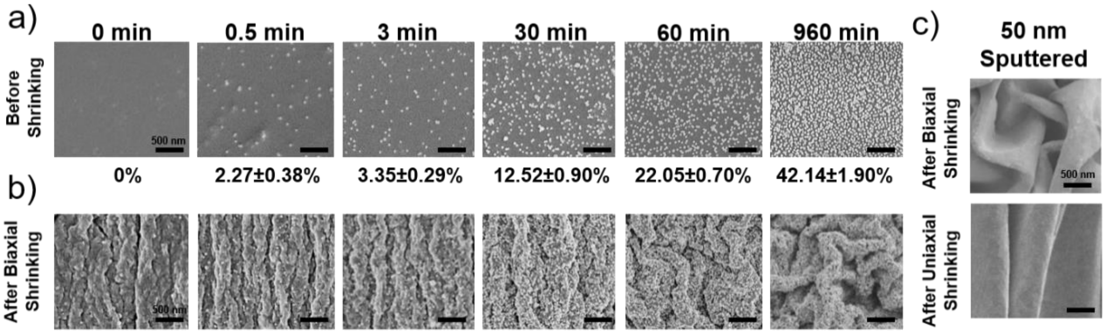

Figure 7.2 The effect of Au NP incubation duration on biaxial wrinkle evolution. a) SEM images of structures created by varying the incubation time of ~36 nm diameter Au NPs before shrinking. The Au NP surface coverage of the PS substrate for various incubation durations before shrinking are displayed below each image. b) The corresponding SEM images of structures after biaxial shrinking. c) SEM image of a structure created from 50 nm sputtered Au after biaxial shrinking. All scale bars represent 500 nm.

When designing functional materials architectures, it becomes essential to tune the structure and organization of the materials building blocks especially at critical interfaces. We sought to create wrinkled nanoparticle layers that were tunable in terms of wrinkle wavelength and amplitude. For this purpose, we investigated whether tuning the size and organization of the primary building blocks (Au NPs) can be used to program the secondary wrinkled structures. First, we varied the size of the Au NPs that formed the film layer, using Au NPs with ~12 nm, ~18 nm, and ~36 nm diameters. All three sizes of Au NPs were used to fabricate uniaxially and biaxially wrinkled surfaces, as seen in Figure 7.3 (a). In both the uniaxial and biaxial wrinkling cases, periodic wrinkled structures, with sub-micron wavelengths, appear across the entire surface of the devices. The TEM cross-sections revealed a sharp wrinkled boundary at the interface of the Au NP film and polystyrene substrates, suggesting that the polystyrene is unable to flow past the self-assembled Au NP layer when it is heated to 160°C and it remains conformal to the wrinkled Au NP film, forming wrinkled structures itself. Furthermore, uniaxially-aligned wrinkles demonstrate significantly smaller amplitudes compared to biaxial wrinkles, which could be attributed to the stacking of multiple Au NP layers during the biaxial wrinkling process, which is observed in the high resolution TEM cross-sections of these samples (Figure 7.3 (c)). In addition, individual distinct nanoparticles were observed in the high resolution TEM cross-sections of the samples in Figure 3 (c), suggesting that the nanoparticle layer does not melt to form a continuous film during the heat-induced wrinkling step of the fabrication process. It was observed that as the size of Au NPs increased, the wavelength (seen in the SEM images and cross-sectional TEM) and the amplitude (seen in the cross-sectional TEM) of the resulting wrinkles also increased. The wavelengths of the uniaxial wrinkles were extracted and plotted in Figure 7.3 (e), where increasing wavelengths were observed for increasing Au NP diameters. The wavelength was 75.4 ±15.2 nm for the ~12nm Au NPs and it was increased to 136.9±30.7 nm and 427.2±94.9 nm for the ~18 nm and ~36 nm Au NPs, respectively. The finding that nanoparticle size can be used to program the size of the induced wrinkles results from the observation that the effective thickness of the Au NP layer is directly related to, and approximately equal to, the Au NPs diameter (Figure 7.3 (d)). As the diameter of the Au NPs increases, the effective film layer thickness increases, which results in larger wrinkles. This height-dependent observation is in excellent agreement with previously developed theoretical models and observations based on continuous sputtered Au films.[119], [121], [128], [199]

A second method for increasing the effective thickness of the Au NP film and tuning the wrinkle sizes was explored through the creation of multilayer Au NP films. We created a layer-by-layer structure by depositing multiple layers of ~12 nm Au NPs using the molecular linker, APTES, to connect one layer to another (an analogous process using a mercaptosilane linker was described previously[275]). We deposited the Au NPs, as one to six layers on the PS substrates, then proceeded to induce uniaxial or biaxial shrinking and wrinkling. It was observed that by increasing the number of Au NP layers the size of the wrinkles is increased as well, for both the uniaxial and biaxial wrinkling cases (Figure 7.3 (b)). This is due to the observation that the effective thickness of the film layer increases with each Au NP layer that is added to the surface, the values of which are displayed in Figure 7.3 (d). The average thickness of each added layer is in line with the diameter of the Au NP building blocks (~12 nm). The wavelengths of the resulting wrinkles followed a linear trend (Figure 7.3 (e)) with respect to the effective thickness, increasing with each additional layer from 89.0±20.0 nm for 2 layer films to 246.1±58.0 nm for 6 layer films. As a result, changing the number of Au NP layers presents another approach for programming the wavelength of the induced wrinkles. The wrinkle wavelengths observed here, using the layer-by-layer assembly of Au NP, are some of the lowest reported for wrinkled films, likely due to the presence of inter-particle voids between Au NPs, which leads to nano-porous films with unique mechanical properties.[128], [248], [276] A comparison between the wrinkle wavelengths for single layer Au NP films of varying diameters, layer-by-layer Au NP films and sputtered Au films with respect to effective film thickness is presented in Figure 7.3 (e). The theoretically predicted linear trend between the effective film thickness ($h_f$) and wrinkle wavelength ($\lambda$), given by the following equation, is observed for every data set.[124]

$$\lambda = 2\pi h_f \left( \frac{(1 - v_s^2)E_f}{3(1 - v_f^2)E_s} \right)^{1/3}$$

Where $E_f$ and $E_s$ are the elastic moduli of the thin film and the substrate, respectively, and $v_f$ and $v_s$ are the Poisson's ratio of the film and the substrate, respectively. However, the slope of these linear trends are very different, suggesting that the various film types have differing effective elastic moduli.[124], [277] For the films investigated here, the sputtered films have the steepest slope, which corresponds to the film of the highest stiffness. This is expected since sputtered films are continuous with less defects and variations over the surface than the Au NP films. The single-layer Au NP films had the next steepest slope, and finally, the layer-by-layer Au NP films had the lowest slope. This indicates that the layer-by-layer Au NP films have the least stiffness amongst the films investigated here. This can be attributed to the presence of nanoscale gaps within the initial non-wrinkled layer, which is expected to occur at a higher frequency compared to single layer NP films of similar effective thickness.

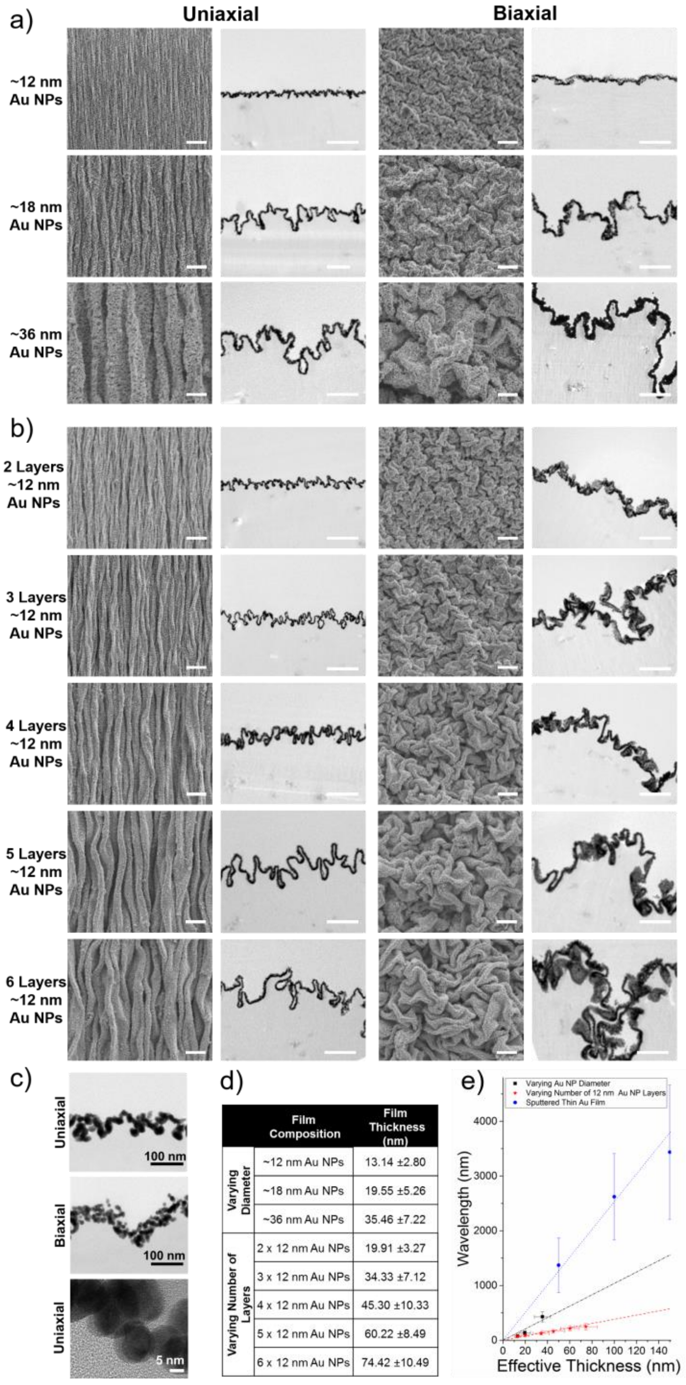

| | Film Composition | Film Thickness (nm) |
|---|---|---|
| Varying Diameter | ~12 nm Au NPs | 13.14 ±2.80 |
| | ~18 nm Au NPs | 19.55 ±5.26 |
| | ~36 nm Au NPs | 35.46 ±7.22 |
| Varying Number of Layers | 2 x 12 nm Au NPs | 19.91 ±3.27 |
| | 3 x 12 nm Au NPs | 34.33 ±7.12 |
| | 4 x 12 nm Au NPs | 45.30 ±10.33 |
| | 5 x 12 nm Au NPs | 60.22 ±8.49 |
| | 6 x 12 nm Au NPs | 74.42 ±10.49 |

Figure 7.3 Tunability of the wrinkled nanoparticle films a) SEM images (left column) and cross-sectional TEM images (right column) of the Au NPs uniaxial and biaxial wrinkles at different Au NP diameters. White scale bars in electron microscopy images represent 500 nm. b) SEM images (left column) and cross-sectional TEM images (right column) of the Au NPs uniaxial and biaxial wrinkles at varying numbers of 12 nm Au NP layers.

White scale bars in electron microscopy images represent 500 nm. c) High magnification cross sectional TEM images of one layer ~12 nm Au NPs wrinkled uniaxially and biaxially. d) Table with the effective film thickness before shrinking for the various films. e) The uniaxial wrinkled wavelength versus effective Au film thickness for varying Au NP diameters, varying number of 12 nm Au NP layers, and a sputtered continuous Au film. Error bars indicate standard deviation, trendlines are linear fits with $R^2>0.95$. White scale bars in electron microscopy images represent 500 nm and black scale bars represent 100 nm.

Although both the Au NP diameter and number of layers can be used to program the wavelength and amplitude of the wrinkles by altering the effective thickness of the initial film layer, each method produces films with differing mechanical properties and differing inter-wrinkle nanostructure morphology. By combining the diameter of Au NPs, number of layers of Au NPs, and the physical constraints during shrinking, the wrinkled nanostructured surfaces can be precisely tuned.

Nanostructured gold surfaces have been used as substrates for surface enhanced Raman scattering (SERS) to significantly increase the intensity of Raman signals from analytes. Simple fabrication procedures to create structurally-tunable nanostructured gold films are highly sought after to reduce the cost of SERS substrates and to better understand the correlation between structure and mechanism of SERS enhancement. We performed a preliminary investigation to determine whether the structural tunability of the wrinkled Au NP films could be translated to designing optimal SERS-active substrates. The SEM images of single-layer 36 nm Au NP films seeded at various densities by controlling the Au NP deposition time (0.5 min, 3 min, 960 min) is displayed in Figure 7.4. These structures were further incubated with 100 μM 4-mercaptopyridine (4Mpy) before and after shrinking and were used in SERS measurements. The spectra obtained show well-resolved peaks before and after wrinkling the films, with the peak intensity increasing with increasing Au NP deposition times. The enhancement in the intensities of the 1090 $cm^{-1}$ peak of the 4Mpy signals from the various density Au NP films were compared, before and after shrinking biaxially, to signals obtained from a sputtered planar Au film incubated with 10 mM 4Mpy (calculation in Experimental section and values displayed in Figure 7.4). The wrinkling process provides a significant enhancement in the intensity of the SERS spectra, up to an order of magnitude greater than the before shrinking films, especially at the low Au NP deposition times (0.5 min and 3 min). This is likely due to the shrinking process bringing deposited Au NPs closer together to enhance the inter-particle electromagnetic coupling,[270] as well as the concentrating effect (6.25 times) of the footprint of the film being reduced to a fraction of its before shrinking size.

The biaxially wrinkled substrate created from the self-assembled Au NP film of the highest density (960 min.) had the highest enhancement of all the films ($5\times10^4$ enhancement over the sputtered Au film). Interestingly, the observed enhancement was only slightly larger than the 960 min film before shrinking ($4.4\times10^4$ enhancement over the sputtered Au film). This less significant increase due to the shrinking process at increased incubation times can be attributed to the local electromagnetic field and the SERS enhancement factor reaching a limit due to the shrinking process forcing some nanoparticles to come in contact and allowing direct electron transfer rather than electromagnetic coupling.[278] These results indicate that shrinking is an effective method for enhancing the SERS signal when the system under investigation suffers from an inherently low density of signal enhancing particles, such as those encountered in biosensing systems.[48]

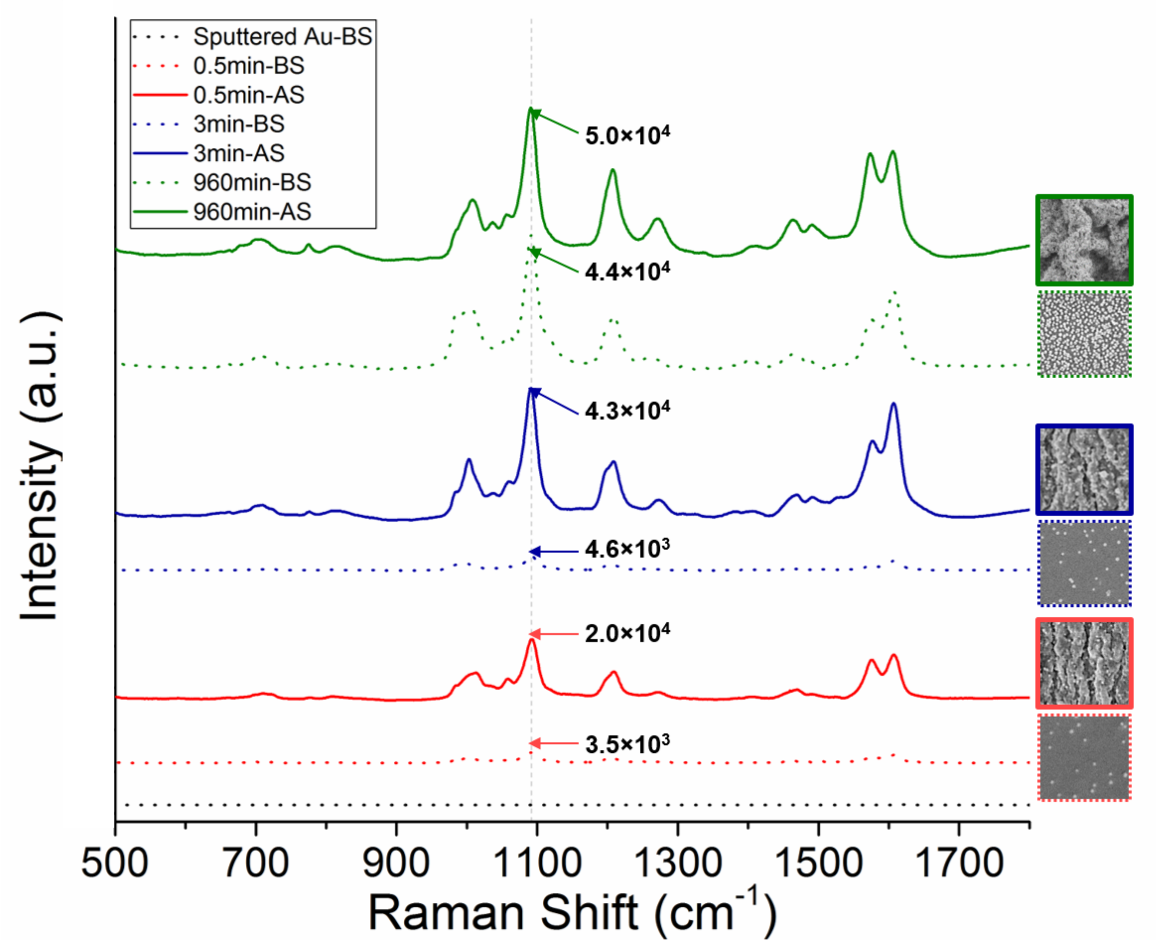

Figure 7.4 Application of ~36 nm Au NP films at various incubation times before shrinking (BS) and after biaxial shrinking (AS) as surface enhanced Raman spectroscopy substrates used for the detection of 100 μM mercaptopyridine (4Mpy). The enhancement factor of each substrate compared to flat 100 nm sputtered Au is labelled for the 1090 $cm^{-1}$ peak (highlighted with grey dashed line).

## 7.5 Conclusions

In summary, we have reported a benchtop method for creating size-tunable wrinkled structures based on all-solution-processing. Wrinkled structures were obtained by depositing a layer of gold nanoparticles on shrinkable polystyrene substrates using self-assembly and heating the substrate over its glass transition temperature for shrinking the substrate and exerting a compressive force on the gold layer. By using physical constraints, we were able to produce both uniaxial and biaxial wrinkles using this method, as observed through SEM, AFM, and TEM characterization. Furthermore, we have demonstrated that the size and wavelength of the wrinkles, can be precisely tuned by the altering the diameter of the Au NPs and the number of layers deposited. Varying the diameter and/or the number of layers of Au NPs could be used to tune the structure of these wrinkled surfaces for use in functional devices. Moreover, the density of the Au NPs can be tuned through the incubation time on the APTES-treated substrate and can be used to change the morphology of the wrinkled structures. We have shown a preliminary application of these wrinkled films as SERS- active substrates for the molecular detection of analytes. These wrinkled metal nanoparticle and polymer composites could be applied to a number of applications including chemical sensors, biosensors, and optoelectronics.

## 7.6 Acknowledgements

The financial support for this work was provided by the Natural Sciences and Engineering Research Council of Canada (NSERC). The EM research described in this paper was performed at the Canadian Centre for Electron Microscopy at McMaster University, which is supported by NSERC and other government agencies. We would like to thank Eric Mahoney and Qiyin Fang for their help with acquiring the SERS data.

# Chapter 8 Summary and Conclusions, Limitations and Future Work, and References

In this concluding chapter, the findings of this thesis work are briefly summarized and the impact they will have on the rapid prototyping of multi-scale materials for integration in lab-on-a-chip devices are discussed. Finally, the limitations of the current work and proposed future work that builds on these findings are discussed.

## 8.1 Thesis Summary

The objective of this work was to develop a benchtop rapid prototyping approach to create tunable multi-scale electrodes, to design these hierarchically structured electrodes and demonstrate their applicability to important lab-on-a-chip (LOC) for point-of-care (POC) diagnostic applications, and to integrate these functional electrodes into contained microfluidic devices.

Benchtop fabrication was carried out through: 1) conductor deposition, initially though sputtering, then through all-solution processed methods; and 2) multi-scale patterning, through a combination of controlled thin film wrinkling using pre-stressed polymer substrates and xurography, as well as additional tuning through electrodeposition, electroless deposition, and/or layer-by-layer assembly of nanoparticles. Characterization of the hierarchical structures was performed through scanning electron microscopy (SEM), transmission electron microscopy (TEM), atomic force microscopy (AFM), white light interferometry, four-point probe measurements, and electrochemical measurements. Application of the multi-scale electrodes was demonstrated through low voltage bacterial cell lysis devices, as well as for electrochemical sensing and surface enhanced Raman spectroscopy (SERS) sensing. Furthermore, we have successfully integrated these three-dimensional, multi-scale wrinkled electrodes into microfluidic devices to create functional electro-fluidic devices.

We have demonstrated that high quality, hierarchically-structured electrodes, with features tuned on the nano-, micro-, and macroscales, and with functional tunability, can be produced from design to integrated device in a matter of a few hours and at a low cost, completely on the laboratory benchtop.

### 8.2 Thesis Conclusions

1) In order to produce functional multi-scale three-dimensional electrode devices, it is possible to pattern hierarchically structured robust electrodes in specific configurations, with tunable features spanning the nanometer to millimeter scales, through the inexpensive, easy to implement and rapid benchtop techniques of xurography and thin film wrinkling on pre-stressed polystyrene (PS), in timeframes of minutes to hours.
2) The size of the topographical features and surface roughness of the wrinkled electrodes can be tailored from the micrometer to the nanometer scale by adjusting the thickness of the gold film deposited through sputtering, electroless deposition, or the layer-by-layer assembly of gold nanoparticles. Increasing film thickness increases the wrinkle/ feature sizes and surface roughness.
3) The multi-scale wrinkled electrodes exhibit significantly enhanced electroactive surface areas per geometric area (665% for sputtered and 730% for 2 min electroless) compared to flat electrodes. Further enhancement in the surface area

can be achieved through additional electrodeposition of nanostructures on the wrinkled metallic surfaces. Moreover, the gold nanostructuring that is produced on the wrinkled electrodes through the tuned electrodeposition was shown to grow at a more rapid rate compared to flat electrodes, likely due to the electric field enhancement offered by the sharp edges of the structured surface.

4) This rapid prototyping technique can be used to create robust interdigitated nanostructured microelectrodes for practical LOC applications, like electrical cell lysis, where voltages are applied to generate strong electric fields. The lysis efficiency of the interdigitated devices can be controlled by changing the applied voltage and the electrode structure. Through numerical modelling, we demonstrated that the temperature increase due to Joule heating is minimal, confirming that electrical lysis is achieved here. It is evident from this work that tuning the electrode structure to be three-dimensional, tall, and with sharp nanostructures decreases the required voltage and increases the lysis efficiency of on-chip lysis devices.
5) Using structurally-optimized electrodes created through xurography, wrinkling, and electrodeposition, we achieved a lysis efficiency higher than 95% at an applied potential of 4 V for *E. coli* cells, making them a potential candidate for integration in portable LOC systems.
6) We investigated the underlying reason for poor bonding between substrates with three-dimensional electrodes and microfluidics after observing leaks at the interfaces. We determined that tall electrodes form microscale voids between tall

electrodes, substrates, and microfluidics materials, through an investigation of the interface using electron microscopy. However, the hierarchically structured, three-dimensional wrinkled electrodes on polystyrene substrates can be successfully incorporated into integrated devices, through the bonding with partially cured PDMS microfluidics and surface treated PS substrates. The method based on bonding partially cured PDMS with APTES treated PS substrates significantly outperformed the other six techniques evaluated in terms of maximum achievable flow rate (maximum flow rate: 27 mL $min^{-1}$, maximum pressure: 130 kPa)

7) Inexpensive (<$1 per device) and disposable integrated microfluidic electrochemical cells featuring four high surface area gold electrodes (2 working, 1 counter, 1 pseudo-reference) can be fabricated rapidly and on the benchtop using the optimized bonding technique that overcomes the microscale voids. The stable and reproducible voltammetric detection of electro-active analytes can be performed with these devices under flow and stagnant conditions without the need for any off-chip electrodes.
8) All-solution processed films can be deposited on PS substrates with speed, ease, and low cost per surface area (<$ 0.03/$cm^2$), using gold nanoparticle (Au NP) self-assembly and electroless deposition. These all-solution processed films wrinkle in a similar manner as sputter-deposited films and are also compatible with xurography-produced masks for defining specific electrode configurations. Moreover, the tunability of the resulting Au film in terms of porosity,

topography and morphology can be controlled through the electroless deposition parameter manipulation and shrink-induced wrinkling.

9) All-solution processed wrinkled films produced through electroless deposition demonstrate conductance comparable to sputter produced films (<1 Ω/□ sheet resistance) and sufficient adhesion (no peeling with tape test) to the underlying PS substrate due to the integration of film into the substrate through the wrinkling process, as evidenced by cross-sectional transmission electron microscopy images of wrinkled electroless deposited films. The structural control of the all-solution processed wrinkled surfaces was translated to functional optimization of substrates for surface enhanced Raman spectroscopy, with large spectral intensity enhancements ($\geq 10^4$) with these rapidly prototyped devices.

10) We determined that tunable wrinkles, similar to those produced with continuous thin films, could be formed through the compression of self-assembled Au NP layers on shape memory polymers. A sufficient density (>~20%) of Au NPs was required to produce typical biaxial morphology wrinkles. Moreover, through the use of physical constraints, as well as altering the size and arrangement of Au NPs, both uniaxial and biaxial wrinkles with tunable wavelengths and amplitudes could be precisely formed, as studied through electron microscopy (SEM and TEM). We have reported some of the smallest wrinkle wavelengths reported to date (~75 nm), and have demonstrated the ability to tune mechanical properties and thicknesses of

the films to develop wrinkles spanning the sub-hundred nanometers to several hundred nanometer range.

### 8.3 Contribution to the Field

The work described in this thesis led to the following contributions to the field:

<u>Rapid, simple, robust fabrication method to create 3D multi-scale electrodes</u>

The development of the fabrication processes described here, which combine xurography and thin film wrinkling on shape memory polymer substrates, will allow for the rapid prototyping of electrodes for LOC devices, as well as other devices that benefit from multi-scale, three-dimensional structures, at high speed and ease on the benchtop. This will expedite the research and development phase for several devices that rely on patterned micro/nanostructured electrodes. It will allow researchers to iterate through device designs rapidly and inexpensively as they selectively tune the structures to obtain specific functional characteristics for performing application-driven functions.

<u>High quality all-solution processed multi-scale materials compatible with thin film wrinkling and xurography</u>

This work was among some of the first examples of using all-solution processed benchtop techniques, like electroless deposition and self-assembly, to create functional and patterned wrinkled materials without the need for vacuum-based deposition methods. We demonstrate that the conductivity and adhesion of the electroless films are similar to that of sputtered films with similar thicknesses. We provide methods to tune the electrode structure through the manipulation of the deposition parameters and characterized the structures through a variety of techniques. These techniques will give researchers more accessible routes to the production of functional and tunable electrodes or interfaces, without the need for specialized, expensive equipment. In addition, while the ability to produce wrinkled structures that can be manipulated on both the nanoscale and the microscale is advantageous for designing electrodes for LOC applications, there are many other applications that can benefit from the enhanced surface functionality these wrinkled structures offer.[145] These applications include technological platforms like flexible electronics, photovoltaics, cell biophysics platforms, etc. An interesting application that would benefit from nanoscale and microscale structural control is employing these wrinkled surfaces as identifying tags, similar to fingerprints, where information about an object can be encoded through the hierarchical structure of the surface.[279] Moreover, these systems can be employed to perform fundamental surface metrology studies for novel nanomaterials to determine mechanical properties that are difficult to measure with other techniques at the sub-100 nm length-scale. This fabrication method is not limited to gold, or even metallic materials, and can be extended to semiconductors, oxides, polymers, etc. to broaden the potential applications of these structures.

### Low voltage cell lysis

While employing the multi-scale electrode fabrication methods to create functional electrical cell lysis devices, it was determined that the increase in voltage increased the lysis efficiency. The voltage that we determined to be effective at lysing (>95% efficiency) the bacteria using the structurally optimized electrodes was 4 V, which is significantly lower than previous electroporation studies with *E.Coli* (40V[39], 500V[187]) and lower than a previous electrochemical lysis study (5V[280]). This investigation into the structural optimization of the electrodes could benefit other lysing or LOC devices that depend on the application of large voltages to generate high strength electric fields.

Integrating tall electrodes

In this work, we have investigated the source of leaks when integrating tall electrodes or features into microfluidics, and developed a method to overcome these limitations to create void-free interfaces and contained device. The bonding method to integrate the multi-scale wrinkled electrodes into contained devices with polystyrene substrates and PDMS microfluidics can be extended to other devices where tall electrodes form voids at the interface between the substrate, microfluidics, and electrode. With the increasing amount of research determining that three-dimensional structures are beneficial for device function, there will be an increased demand for these unique bonding methods to create fully integrated devices.

## 8.4 Future Work

This sections addresses some of the remaining challenges and possible future directions of this work in terms of applications, fundamental studies, and theoretical models for the wrinkling process. These possible directions involve defining research problems that will encompass many fields including materials engineering, electrical engineering, microfabrication, nanotechnology, chemistry, and biochemistry.

## 1. Applications

### a. Automated and integrated sample preparation

The development of very low voltage bacterial cell lysis devices on polymer substrates has been presented in Chapter 4. While the lysis and release of nucleic acids from *E.coli* samples at low voltages was demonstrated with these interdigitated multi-scale electrode devices, there are some studies that are recommended as a future work for the development of this platform, so that it can be applied to an integrated LOC device:

1) A more in-depth study of other gram negative bacteria, as well as gram positive bacteria, mycobacteria, mammalian cells, etc. samples could be performed to determine how robust these devices are and their applicability to other cell types.
2) Moreover, while the electrical cell lysis work was being conducted, an interesting observation was noted. With no applied potential, lysed cells were observed at the sharp features of the electrodes, suggesting that the cells may be mechanically punctured. The lysing effects of the sharp nanostructures produced through electrodeposition could be investigated to determine if they could be used to extract cellular materials without additional power. Preliminary data, conducted in collaboration with researchers from Fraunhofer IZI, suggests that the electrodeposited nanospikes are capable of disrupting the outer cell structure of *M. Smegmatis* (Figure 8.1).

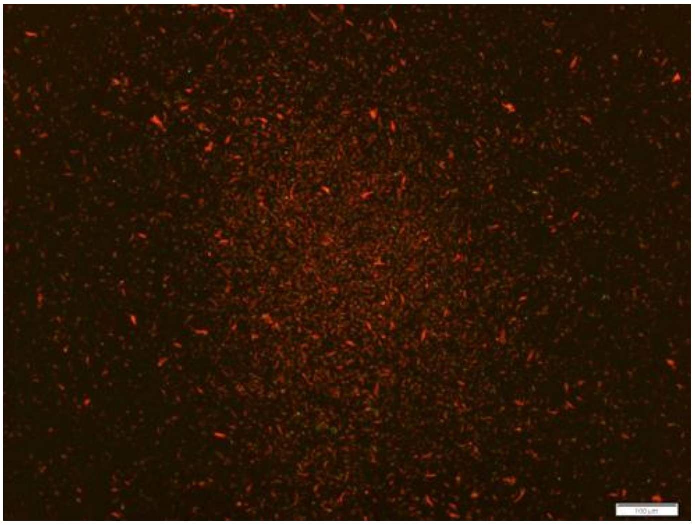

Figure 8.1. *M. smegmatis* stained with Baclight Live/Dead kit (green stain indicates Syto 9 (live), red indicates propidium iodide stain (dead)) after 5 min incubation on electrodeposited wrinkled devices.

3) The cell lysis interdigitated electrodes were demonstrated operating as standalone devices, but the ultimate goal is to integrate it with other sample preparation and detection platforms to create a complete POC system. Integration with microfluidics will be critical to achieve this. A method to incorporate tall, multi-scale electrodes into microfluidic devices was presented in Chapter 5 and could be applied to the lysis electrode devices. In order to achieve faster bioprocessing and detection times, active transport through the LOC device of the samples and molecules to be analysed can be employed by generating flow through electro- and magneto-kinetic methods or mechanical displacement[281]. The microfluidic networks and additional transducing electrodes to control flow and mixing of the samples will need to be developed and integrated with the existing lysis and sensing electrodes, as well as any additional sample preparation modules. Challenges, such as optimizing flow conditions for efficient lysis, minimizing

power requirements, and non-specific adsorption, will be some of the fabrication, integration, and materials challenges that can be addressed in future work.

4) After the lysis has been optimized with the microfluidics, other platforms will be incorporated to make a preliminary LOC device for bacterial detection. A colleague in our research group is developing an electrochemical nucleic acid detection system with the wrinkled structured electrodes. The detection device and the lysis device will be united into a single system using the microfluidics to carry the lysate produced to the electrochemical sensor for nucleic acid detection. Other sample preparation platforms, such as biofiltration and concentration, can also be integrated with the cell lysis and biosensor units. The objective of this work is to demonstrate the rapid and inexpensive fabrication of a functional bacterial detection chip for POC applications using only benchtop techniques. These devices will have applications not only in pathogen detection, but could also be extended to DNA sequencing devices or other biomolecule detection systems.

### b. Application of the multi-length-scale electrodes to various biosensing applications

While the primary focus of this thesis was on fabrication method development, multi-length-scale material characterization and integration, and preliminary bioprocessing and chemical sensing applications, there are several potential biosensing applications of the research that are worthy of further investigation:

1) First, enzyme-free glucose monitoring devices, in contrast to the commonly available systems based on enzyme electrodes, are critical for developing sensing systems that offer sufficient stability for in-vivo applications. Given that glucose oxidation is a kinetically-controlled process, it is very sensitive to the nano/micro structure and surface area of the sensing electrodes. As a result, several new nanomaterials – nanowires,[282] nanoporous structures,[283]–[287] nanoparticles and nanotubes[288] – have been developed for catalytic electro-oxidation of glucose without the use of enzymatic mediators.[289] We hypothesize the nanoporous and high surface area gold electrodes fabricated through the all-solution processing methods described in Chapter 6 could be applied to produce an effective electrochemical platform for catalytic oxidation of glucose. Preliminary experiments conducted in collaboration with other researchers in our research group have indicated that the 2 min electroless wrinkled devices are capable of detecting various concentrations of glucose covering the physiological range and show higher sensitivities compared to other wrinkled and planar devices (Figure 8.2). Further experiments to determine the selectivity, detection limits, and performance with interfering species (i.e. $Cl^-$ ions, ascorbic acid, etc.) should be explored.

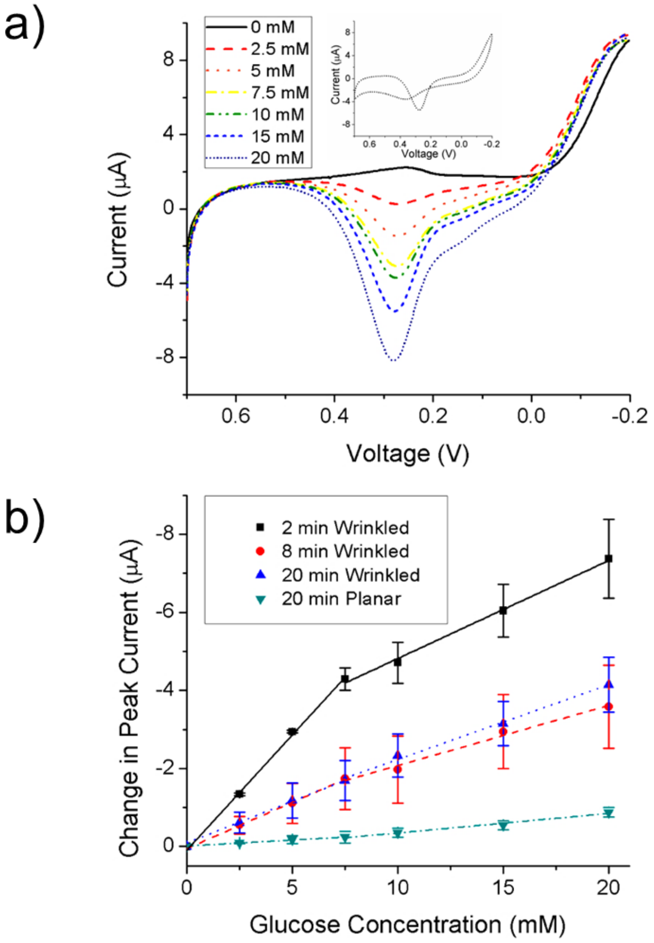

Figure 8.2. Glucose sensing with all-solution-processed wrinkled electrodes. a) Overlay of the reverse (negative) scan portion of cyclic voltammograms (CV) at different concentrations of glucose in 0.1 M PBS using 2 min wrinkled device. The inset is a complete CV of the forward and reverse scan. b) Analysis of CVs for each electrode type for the different concentrations of glucose assessed. The plots demonstrate the peak current at ~0.27 V.

2) Next, the affinity-based detection of nucleic acids, such as DNA and RNA, has many applications in disease management, health monitoring, forensics, and environmental monitoring.[8] It has been shown by other researchers in our group that the wrinkled gold electrodes fabricated through the methods described in Chapter 3, can be employed as electrochemical DNA biosensors and that the unique structure is beneficial for precisely tuning the ssDNA probe monolayer.[221] The applicability of the all-solution-processed wrinkled electrodes described in Chapter 6 to these applications, has started to be investigated by other researchers in our group. These electrodes have been coupled with biorecognition layers, ssDNA probes, for sequence-specific nucleic acid capture and integrated with an electrochemical readout method for translating nucleic acid hybridization to an electrochemical current[290]. Preliminary hybridization experiments with complementary and non-complementary 20 nucleotide long ssDNA targets in solutions containing a previously-developed electrocatalytic reporter system to test the selectivity of our wrinkled electrodes in detecting DNA binding events (Figure 8.3).[31], [291] While both the sputtered and all-solution processed electrodes present as interesting platforms for DNA detection, a thorough study of these systems’ limit-of-detections, dynamic ranges, and abilities in distinguishing single base pair mismatches would be important as future work for assessing them as practical sensors.

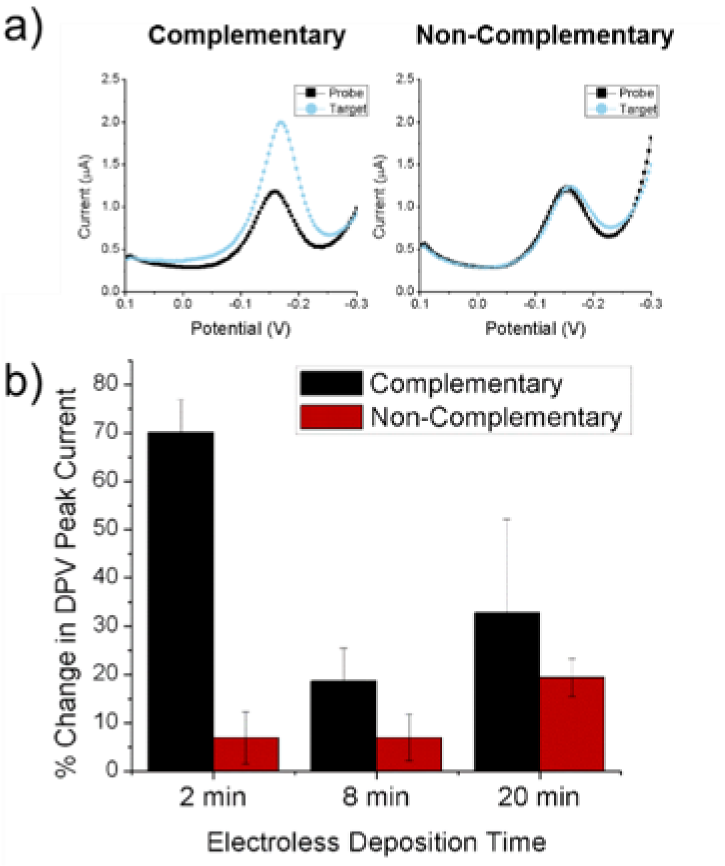

Figure 8.3. DNA hybridization detection with all-solution-processed wrinkled electrodes. a) Typical differential pulse voltammograms (DPV) for before hybridization (ssDNA Probe scan) and after hybridization with complementary (C) and non-complementary (NC) ssDNA targets (1 µM) for 2 min wrinkled electrodes. b) Analysis of DPVs for each wrinkled electrode type for hybridization with complementary and non-complementary targets (1 µM). Error bars indicate standard error over 3 devices.

3) In addition to electrochemical biosensing, further testing of the porous all-solution-processed films and nanoparticle films as SERS-based sensors can be performed in future work. In addition to determining the detection limit of these sensors, it is recommended that testing of these substrates is performed with biologically relevant analytes at physiological concentrations, as well as in buffer and complex media. The electrodes developed in this thesis have several potential sensing applications that benefit from high surface areas and multi-length-scale features.

2. <u>Fundamental Studies</u>

While the number of potential applications of the rapid fabrication method and resulting structures is great, in order to apply them effectively further investigation into the understanding specific aspects of the structuring process and mechanisms of functional enhancements should be conducted through fundamental studies. These include:

1) Investigating various portions of the all-solution processed/ nanoparticle based wrinkled surfaces to optimize and control these processes. First, the self-assembly process of nanoparticles on polymer substrates should be studied more in-depth. If this process is better understood, more control of the resulting electroless deposited devices or directly wrinkled devices can be achieved. Next, the nanoparticle parameters (diameter, materials, etc.) and the electroless deposition parameters (materials, concentrations, etc.) can be varied to determine the effect on structure. Moreover, exploring the limits of this wrinkling process, for

example, in terms of how small the particle sizes or film thickness can be to still obtain wrinkled structures would be another interesting aspect to explore.

2) Studying the functional parameters of the structures and the mechanisms of enhancements for specific applications to design efficient and optimized devices. For example, for the use of these electrodes as electrochemical sensors the sensing mechanisms and parameters should be explored to better understand the effect of the structure on the system. This would include studying electrochemical signal transduction on these surfaces, 2D surface transport, and structure-induced catalytic effects, as well as application-specific parameters, such as probe density and hybridization efficiency of DNA electrochemical sensors.

### 3. Theoretical Models for Wrinkling Process

Another recommended area of future research is the development of more comprehensive theoretical models to describe the wrinkling structure, which will allow researchers to better predict and design wrinkled surfaces using materials systems that are not completely described by current models. Specifically, the following systems:

1) Nanomaterial films, non-continuous film layers made from individual nanoscale building blocks, are treated as an effective continuous film in current bilayer models for wrinkling. While this does help predict the bulk behaviour of these “effective films”, the properties of the individual nanomaterials are difficult to decouple from other possible contributors to the effective films, such as substrate interactions, molecular linkers, air gaps, etc. A model that can isolate the

properties of the individual nanoparticles, as well as predict additional contributions would be beneficial designing structures with these materials systems.

2) Multi-layers are also not fully described by the conventional bilayer model of thin film wrinkling. As more layer-by-layer assembled or composite materials are utilized as film layers in wrinkled systems, newer models are needed to take into account interfacial regions between the layers. These interfacial regions may have altered properties compared to each individual layer, and must be accounted for in order to better predict the resulting morphology.[276]

### 8.5 References

[1] C. M. Gabardo and L. Soleymani, “Deposition, patterning, and utility of conductive materials for the rapid prototyping of chemical and bioanalytical devices,” *Analyst*, no. 141, pp. 3511–3525, 2016.

[2] C. M. Gabardo, A. Hosseini, and L. Soleymani, “A New Wrinkle in Biosensors,” *IEEE Nanotechnology Magazine*, no. June, pp. 6–18, 2016.

[3] World Health Organization, “The World Health Report 2004 Statistical Annex,” 2004.

[4] “Tuberculosis Fact Sheet,” *World Health Organization*, 2016. [Online]. Available: http://www.who.int/mediacentre/factsheets/fs104/en/#.

[5] World Health Organization, “Tuberculosis,” *Fact Sheet No 104*, 2012. [Online]. Available: http://www.who.int/mediacentre/factsheets/fs104/en/#.

[6] P. Yager, G. J. Domingo, and J. Gerdes, “Point-of-care diagnostics for global health.,” *Annu. Rev. Biomed. Eng.*, vol. 10, pp. 107–144, Jan. 2008.

[7] W. G. Lee, Y.-G. Kim, B. G. Chung, U. Demirci, and A. Khademhosseini, “Nano/microfluidics for diagnosis of infectious diseases in developing countries,” *Adv. Drug Deliv. Rev.*, vol. 62, no. 4–5, pp. 449–457, 2011.

[8] A. P. F. Turner, “Biosensors-Sense and Sensitivity,” *Science (80-. ).*, vol. 290, no. 5495, pp. 1315–1317, 2000.

[9] J. Wang, “From DNA biosensors to gene chips.,” *Nucleic Acids Res.*, vol. 28, no. 16, pp. 3011–3016, Aug. 2000.

[10] P. A. Piunno, U. J. Krull, R. H. Hudson, M. J. Damha, and H. Cohen, “Fiber-optic DNA sensor for fluorometric nucleic acid determination.,” *Anal. Chem.*, vol. 67, no. 15, pp. 2635–2643, Aug. 1995.

[11] F. Uslu, S. Ingebrandt, D. Mayer, S. Böcker-Meffert, M. Odenthal, and A. Offenhäusser, “Labelfree fully electronic nucleic acid detection system based on a field-effect transistor device.,” *Biosens. Bioelectron.*, vol. 19, no. 12, pp. 1723–1731, Jul. 2004.

[12] M. Calleja, M. Nordström, M. Álvarez, J. Tamayo, L. M. Lechuga, and A. Boisen, “Highly sensitive polymer-based cantilever-sensors for DNA detection,” *Ultramicroscopy*, vol. 105, no. 1–4, pp. 215–222, 2005.

[13] Y. Huang, E. Mather, J. Bell, and M. Madou, “MEMS-based sample preparation for molecular diagnostics,” *Anal. Bioanal. …*, no. 372, pp. 49–65, 2002.

[14] X. Chen and D.-F. Cui, “Microfluidic devices for sample pretreatment and

applications," *Microsyst. Technol.*, no. 15, pp. 667–676, 2009.

[15] J. Kim, M. Johnson, P. Hill, and B. K. Gale, "Microfluidic sample preparation: cell lysis and nucleic acid purification.," *Integr. Biol. (Camb).*, vol. 1, no. 10, pp. 574–586, Oct. 2009.

[16] Y. Chen, X. Wang, H. Ren, H. Yin, and S. Jia, "Hierarchical Dragonfly Wing: Microstructure-Biomechanical Behavior Relations," *J. Bionic Eng.*, vol. 9, no. 2, pp. 185–191, 2012.

[17] H. Gao, X. Wang, H. Yao, S. Gorb, and E. Arzt, "Mechanics of hierarchical adhesion structures of geckos," *Mech. Mater.*, vol. 37, no. 2–3 SPEC. ISS., pp. 275–285, 2005.

[18] K. Koch, B. Bhushan, Y. C. Jung, and W. Barthlott, "Fabrication of artificial Lotus leaves and significance of hierarchical structure for superhydrophobicity and low adhesion," *Soft Matter*, vol. 5, no. 7, pp. 1386–1393, 2009.

[19] P. Fratzl and R. Weinkamer, "Nature's hierarchical materials," *Prog. Mater. Sci.*, vol. 52, no. 8, pp. 1263–1334, Nov. 2007.

[20] R. Lakes, "Materials with structural hierarchy," *Nature*, vol. 361, pp. 511–515, 1993.

[21] L. Tsakalakos, J. Balch, J. Fronheiser, B. A. Korevaar, O. Sulima, and J. Rand, "Silicon nanowire solar cells," *Appl. Phys. Lett.*, vol. 91, no. 23, p. 233117, 2007.

[22] M. J. Bierman and S. Jin, "Potential applications of hierarchical branching nanowires in solar energy conversion," *Energy Environ. Sci.*, vol. 2, no. 10, pp. 1050–1059, 2009.

[23] A. Chen, D. K. Lieu, L. Freschauf, V. Lew, H. Sharma, J. Wang, D. Nguyen, I. Karakikes, R. J. Hajjar, A. Gopinathan, E. Botvinick, C. C. Fowlkes, R. A. Li, and M. Khine, "Shrink-film configurable multiscale wrinkles for functional alignment of human embryonic stem cells and their cardiac derivatives.," *Adv. Mater.*, vol. 23, no. 48, pp. 5785–5791, Dec. 2011.

[24] M. J. Dalby, N. Gadegaard, R. Tare, A. Andar, M. O. Riehle, P. Herzyk, C. D. W. Wilkinson, and R. O. C. Oreffo, "The control of human mesenchymal cell differentiation using nanoscale symmetry and disorder.," *Nat. Mater.*, vol. 6, no. 12, pp. 997–1003, Dec. 2007.

[25] M. M. Stevens and J. H. George, "Exploring and engineering the cell surface interface.," *Science*, vol. 310, no. 5751, pp. 1135–1138, Nov. 2005.

[26] M. Goldberg, R. Langer, and X. Jia, "Nanostructured materials for applications in drug delivery and tissue engineering," *J. Biomater. Sci. Polym. Ed.*, vol. 18, no. 3,

pp. 241–268, 2007.

[27] J. M. J. Frechet, "Dendrimers and other dendritic macromolecules: From building blocks to functional assemblies in nanoscience and nanotechnology," *J. Polym. Sci. Part A Polym. Chem.*, vol. 41, no. 23, pp. 3713–3725, 2003.

[28] Y. Sun, X. Hu, W. Luo, and Y. Huang, "Self-Assembled Hierarchical MoO 2 /Graphene Nanoarchitectures and Their Application as a High-Performance Anode Material for Lithium-Ion Batteries," *ACS Nano*, vol. 5, no. 9, pp. 7100–7107, 2011.

[29] D. W. Wang, F. Li, M. Liu, G. Q. Lu, and H. M. Cheng, "3D aperiodic hierarchical porous graphitic carbon material for high-rate electrochemical capacitive energy storage," *Angew. Chemie - Int. Ed.*, vol. 47, no. 2, pp. 373–376, 2008.

[30] L. Soleymani, Z. Fang, B. Lam, X. Bin, E. Vasilyeva, A. J. Ross, E. H. Sargent, and S. O. Kelley, "Hierarchical nanotextured microelectrodes overcome the molecular transport barrier to achieve rapid, direct bacterial detection.," *ACS Nano*, vol. 5, no. 4, pp. 3360–3366, Apr. 2011.

[31] L. Soleymani, Z. C. Fang, E. H. Sargent, and S. O. Kelley, "Programming the detection limits of biosensors through controlled nanostructuring.," *Nat. Nanotechnol.*, vol. 4, no. 12, pp. 844–848, Dec. 2009.

[32] X. Lu, Y. Xiao, Z. Lei, and J. Chen, "Graphitized macroporous carbon microarray with hierarchical mesopores as host for the fabrication of electrochemical biosensor.," *Biosens. Bioelectron.*, vol. 25, no. 1, pp. 244–247, Sep. 2009.

[33] S. O. Kelley, C. A. Mirkin, D. R. Walt, R. F. Ismagilov, M. Toner, and E. H. Sargent, "Advancing the speed, sensitivity and accuracy of biomolecular detection using multi-length-scale engineering," *Nat. Nanotechnol.*, vol. 9, no. 12, pp. 969–980, 2014.

[34] C. Bréchignac, P. Houdy, and M. Lahmani, *Nanomaterials and nanochemistry*. Springer Berlin Heidelberg, 2007.

[35] K. K. Nanda, A. Maisels, F. E. Kruis, H. Fissan, and S. Stappert, "Higher Surface Energy of Free Nanoparticles," *Phys. Rev. Lett.*, vol. 90, no. 10, p. 106102, 2003.

[36] A. Pratt, L. Lari, O. Hovorka, A. Shah, C. Woffinden, S. P. Tear, C. Binns, and R. Kröger, "Enhanced oxidation of nanoparticles through strain-mediated ionic transport.," *Nat. Mater.*, vol. 13, no. 1, pp. 26–30, 2014.

[37] A. Nel, T. Xia, L. Mädler, and N. Li, "Toxic potential of materials at the nanolevel.," *Science*, vol. 311, no. 2006, pp. 622–627, 2006.

[38] F. Li, X. Han, and S. Liu, "Development of an electrochemical DNA biosensor with a high sensitivity of fM by dendritic gold nanostructure modified electrode.,"

*Biosens. Bioelectron.*, vol. 26, no. 5, pp. 2619–2625, Jan. 2011.

[39] M. Shahini and J. T. W. Yeow, "Carbon nanotubes for voltage reduction and throughput enhancement of electrical cell lysis on a lab-on-a-chip.," *Nanotechnology*, vol. 22, no. 32, p. 325705 (1–6), Aug. 2011.

[40] M. Shahini and J. T. W. Yeow, "Cell electroporation by CNT-featured microfluidic chip.," *Lab Chip*, pp. 2585–2590, Mar. 2013.

[41] D. W. Inglis, R. Riehn, R. H. Austin, and J. C. Sturm, "Continuous microfluidic immunomagnetic cell separation," *Appl. Phys. Lett.*, vol. 85, no. 21, pp. 5093–5096, 2004.

[42] D. W. Inglis, R. Riehn, J. C. Sturm, and R. H. Austin, "Microfluidic high gradient magnetic cell separation," *J. Appl. Phys.*, vol. 99, no. 8, pp. 99–101, 2006.

[43] D. Nawarathna, N. Norouzi, J. McLane, H. Sharma, N. Sharac, T. Grant, A. Chen, S. Strayer, R. Ragan, and M. Khine, "Shrink-induced sorting using integrated nanoscale magnetic traps," *Appl. Phys. Lett.*, vol. 102, no. 6, p. 063504, 2013.

[44] J. Hahm and C. M. Lieber, "Direct ultrasensitive electrical detection of DNA and DNA sequence variations using nanowire nanosensors," *Nano Lett.*, vol. 4, no. 1, pp. 51–54, 2004.

[45] O. R. Bolduc and J. F. Masson, "Advances in surface plasmon resonance sensing with nanoparticles and thin films: Nanomaterials, surface chemistry, and hybrid plasmonic techniques," *Anal. Chem.*, vol. 83, pp. 8057–8062, 2011.

[46] E. Smith and G. Dent, *Modern Raman Spectroscopy – A Practical Approach*. England: John Wiley & Son, Inc., 2005.

[47] X. Chen, C. Jiang, and S. Yu, "Nanostructured materials for applications in surface-enhanced Raman scattering," *CrystEngComm*, vol. 16, pp. 9959–9973, 2014.

[48] Y. C. Cao, R. Jin, and C. A. Mirkin, "Nanoparticles with Raman spectroscopic fingerprints for DNA and RNA detection.," *Science*, vol. 297, no. 2002, pp. 1536–1540, 2002.

[49] H. Liu, L. Zhang, X. Lang, Y. Yamaguchi, H. Iwasaki, Y. Inouye, Q. Xue, and M. Chen, "Single molecule detection from a large-scale SERS-active Au79Ag21 substrate," *Sci. Rep.*, vol. 1, no. 112, pp. 1–5, 2011.

[50] P. E. Sheehan, L. J. Whitman, C. Di V, and V. Na, "Detection Limits for Nanoscale Biosensors," *Nano Lett.*, vol. 5, no. 4, pp. 803–807, 2005.

[51] P. R. Nair and M. A. Alam, "Performance limits of nanobiosensors," *Appl. Phys. Lett.*, vol. 88, p. 233120, 2006.

[52] T. M. Squires, R. J. Messinger, and S. R. Manalis, “Making it stick: convection, reaction and diffusion in surface-based biosensors.,” *Nat. Biotechnol.*, vol. 26, no. 4, pp. 417–426, 2008.

[53] J. S. Shim, M. J. Rust, and C. H. Ahn, “A large area nano-gap interdigitated electrode array on a polymer substrate as a disposable nano-biosensor,” *J. Micromechanics Microengineering*, vol. 23, no. 3, p. 035002, 2013.

[54] A. Ebrahimi, P. Dak, E. Salm, S. Dash, S. V Garimella, R. Bashir, and M. A. Alam, “Nanotextured superhydrophobic electrodes enable detection of attomolar-scale DNA concentration within a droplet by non-faradaic impedance spectroscopy,” *Lab Chip*, vol. 13, no. 21, pp. 4248–4256, 2013.

[55] M. Poudineh, R. M. Mohamadi, A. Sage, L. Mahmoudian, E. H. Sargent, and S. O. Kelley, “Three-dimensional, sharp-tipped electrodes concentrate applied fields to enable direct electrical release of intact biomarkers from cells.,” *Lab Chip*, vol. 14, no. 10, pp. 1785–1790, May 2014.

[56] J.-M. Nam, C. S. Thaxton, and C. A. Mirkin, “Nanoparticle-based bio-bar codes for the ultrasensitive detection of proteins.,” *Science*, vol. 301, no. 5641, pp. 1884–1886, 2003.

[57] D. Whang, S. Jin, Y. Wu, and C. M. Lieber, “Large-Scale Hierarchical Organization of Nanowire Arrays for Integrated Nanosystems,” *Nano Lett.*, vol. 3, no. 9, pp. 1255–1259, Sep. 2003.

[58] A. Hierlemann, O. Brand, C. Hagleitner, and H. Baltes, “Microfabrication techniques for chemical/biosensors,” *Proc. IEEE*, vol. 91, no. 6, pp. 839–863, Jun. 2003.

[59] D. Qin, Y. N. Xia, J. A. Rogers, R. J. Jackman, X. M. Zhao, and G. M. Whitesides, “Microfabrication, microstructures and microsystems,” *Microsyst. Technol. Chem. Life Sci.*, vol. 194, pp. 1–20, 1998.

[60] S. C. Terry, J. H. Jerman, and J. B. Angell, “A gas chromatographic air analyzer fabricated on a silicon wafer,” *IEEE Trans. Electron Devices*, vol. 26, no. 12, pp. 1880–1886, 1979.

[61] G. M. Whitesides, “The origins and the future of microfluidics.,” *Nature*, vol. 442, no. 7101, pp. 368–373, 2006.

[62] A. Manz, D. J. Harrison, E. M. J. Verpoorte, J. C. Fettinger, A. Paulus, H. Lüdi, and H. M. Widmer, “Planar chips technology for miniaturization and integration of separation techniques into monitoring systems Capillary electrophoresis on a chip,” *J. Chromatogr. A*, vol. 593, no. 1–2, pp. 253–258, 1992.

[63] D. J. Harrison, K. Fluri, K. Seiler, Z. Fan, C. S. Effenhauser, and A. Manz,

"Micromachining a Miniaturized Capillary Electrophoresis-Based Chemical Analysis System on a Chip," *Science (80-. ).*, vol. 261, no. 5123, pp. 895–897, 1993.

[64] H. Becker and C. Gärtner, "Polymer microfabrication technologies for microfluidic systems.," *Anal. Bioanal. Chem.*, vol. 390, no. 1, pp. 89–111, 2008.

[65] H. Becker and L. E. Locascio, "Polymer microfluidic devices," *Talanta*, vol. 56, no. 2, pp. 267–287, 2002.

[66] A. de Mello, "Plastic fantastic?," *Lab Chip*, vol. 2, no. 2, p. 31N–36N, May 2002.

[67] C. H. Ahn, J. W. Choi, G. Beaucage, J. H. Nevin, J. B. Lee, A. Puntambekar, and J. Y. Lee, "Disposable smart lab on a chip for point-of-care clinical diagnostics," *Proc. IEEE*, vol. 92, no. 1, pp. 154–173, 2004.

[68] A. Waldbaur, H. Rapp, K. Länge, and B. E. Rapp, "Let there be chip—towards rapid prototyping of microfluidic devices: one-step manufacturing processes," *Anal. Methods*, vol. 3, no. 12, pp. 2681–2716, 2011.

[69] C.-W. Tsao and D. L. DeVoe, "Bonding of thermoplastic polymer microfluidics," *Microfluid. Nanofluidics*, vol. 6, no. 1, pp. 1–16, Nov. 2008.

[70] D. C. Duffy, J. C. McDonald, O. J. Schueller, and G. M. Whitesides, "Rapid Prototyping of Microfluidic Systems in Poly(dimethylsiloxane).," *Anal. Chem.*, vol. 70, no. 23, pp. 4974–4984, Dec. 1998.

[71] C. S. Effenhauser, G. J. Bruin, A. Paulus, and M. Ehrat, "Integrated capillary electrophoresis on flexible silicone microdevices: analysis of DNA restriction fragments and detection of single DNA molecules on microchips.," *Anal. Chem.*, vol. 69, no. 17, pp. 3451–3457, Sep. 1997.

[72] J. C. Mcdonald, D. C. Duffy, J. R. Anderson, and D. T. Chiu, "Review - Fabrication of microfluidic systems in poly (dimethylsiloxane)," *Electrophoresis*, vol. 21, pp. 27–40, 2000.

[73] J. Kim, A. J. DeMello, S.-I. Chang, J. Hong, and D. O'Hare, "Thermoset polyester droplet-based microfluidic devices for high frequency generation," *Lab Chip*, vol. 11, no. 23, pp. 4108–4112, 2011.

[74] G. S. Fiorini, R. M. Lorenz, J. Kuo, and D. T. Chiu, "Rapid prototyping of thermoset polyester microfluidic devices," *Anal. Chem.*, vol. 76, no. 16, pp. 4697–4704, 2004.

[75] A. W. Browne, M. J. Rust, W. Jung, S. H. Lee, and C. H. Ahn, "A rapid prototyping method for polymer microfluidics with fixed aspect ratio and 3D tapered channels," *Lab Chip*, vol. 9, no. 20, pp. 2941–2946, 2009.

[76] C. D. Chin, V. Linder, and S. K. Sia, “Commercialization of microfluidic point-of-care diagnostic devices,” *Lab Chip*, vol. 12, no. 12, pp. 2118–2134, 2012.

[77] P. S. Nunes, P. D. Ohlsson, O. Ordeig, and J. P. Kutter, “Cyclic olefin polymers: emerging materials for lab-on-a-chip applications,” *Microfluid. Nanofluidics*, vol. 9, no. 2–3, pp. 145–161, 2010.

[78] U. M. Attia, S. Marson, and J. R. Alcock, “Micro-injection moulding of polymer microfluidic devices,” *Microfluid. Nanofluidics*, vol. 7, no. 1, pp. 1–28, 2009.

[79] E. Sollier, C. Murray, P. Maoddi, and D. Di Carlo, “Rapid prototyping polymers for microfluidic devices and high pressure injections,” *Lab Chip*, vol. 11, pp. 3752–3765, 2011.

[80] B. Ziaie, A. Baldi, M. Lei, Y. Gu, and R. A. Siegel, “Hard and soft micromachining for BioMEMS: Review of techniques and examples of applications in microfluidics and drug delivery,” *Adv. Drug Deliv. Rev.*, vol. 56, no. 2, pp. 145–172, 2004.

[81] S. S. Djoki and P. L. Cavallotti, “Electroless Deposition: Theory and Applications,” in *Electrodeposition: Theory and Applications*, vol. 48, Springer-Verlag New York, 2010, pp. 251–289.

[82] R. J. Waltman and J. Bargon, “Electrically conducting polymers: a review of the electropolymerization reaction, of the effects of chemical structure on polymer film properties, and of applications towards technology,” *Can. J. Chem.*, vol. 64, no. 1, pp. 76–95, 1986.

[83] G. Cummins, “Inkjet printing of conductive materials: a review,” *Circuit World*, vol. 38, no. 4, pp. 193–213, 2012.

[84] N. Dossi, F. Terzi, E. Piccin, R. Toniolo, and G. Bontempelli, “Rapid Prototyping of Sensors and Conductive Elements by Day-to-Day Writing Tools and Emerging Manufacturing Technologies,” *Electroanalysis*, vol. 27, pp. 1–16, 2015.

[85] C. Ladd, J. H. So, J. Muth, and M. D. Dickey, “3D printing of free standing liquid metal microstructures,” *Adv. Mater.*, vol. 25, no. 36, pp. 5081–5085, 2013.

[86] O. D. Renedo, M. A. Alonso-Lomillo, and M. J. A. Martínez, “Recent developments in the field of screen-printed electrodes and their related applications,” *Talanta*, vol. 73, no. 2, pp. 202–219, 2007.

[87] J. Kim, K. Wubs, B.-S. Bae, and W. Soo Kim, “Direct stamping of silver nanoparticles toward residue-free thick electrode,” *Sci. Technol. Adv. Mater.*, vol. 13, no. 3, p. 035004, 2012.

[88] J. Olkkonen, K. Lehtinen, and T. Erho, “Flexographically printed fluidic structures

in paper," *Anal. Chem.*, vol. 82, no. 24, pp. 10246–10250, 2010.

[89] I. Hod, W. Bury, D. M. Karlin, P. Deria, C.-W. Kung, M. J. Katz, M. So, B. Klahr, D. Jin, Y.-W. Chung, T. W. Odom, O. K. Farha, and J. T. Hupp, "Directed Growth of Electroactive Metal-Organic Framework Thin Films Using Electrophoretic Deposition," *Adv. Mater.*, vol. 26, no. 36, pp. 6295–6300, 2014.

[90] I. Grunwald, E. Groth, I. Wirth, J. Schumacher, M. Maiwald, V. Zoellmer, and M. Busse, "Surface biofunctionalization and production of miniaturized sensor structures using aerosol printing technologies.," *Biofabrication*, vol. 2, no. 1, p. 014106, 2010.

[91] K. An, S. Hong, S. Han, H. Lee, J. Yeo, and S. H. Ko, "Selective sintering of metal nanoparticle ink for maskless fabrication of an electrode micropattern using a spatially modulated laser beam by a digital micromirror device.," *ACS Appl. Mater. Interfaces*, vol. 6, no. 4, pp. 2786–2790, 2014.

[92] B. H. Lee, S. H. Park, H. Back, and K. Lee, "Novel film-casting method for high-performance flexible polymer electrodes," *Adv. Funct. Mater.*, vol. 21, pp. 487–493, 2011.

[93] B. Guo, L. Glavas, and A.-C. Albertsson, "Biodegradable and electrically conducting polymers for biomedical applications," *Prog. Polym. Sci.*, vol. 38, no. 9, pp. 1263–1286, 2013.

[94] Q. Guo, J. P. Mather, P. Yang, M. Boden, and P. T. Mather, "Fabrication of Polymeric Coatings with Controlled Microtopographies Using an Electrospraying Technique," *PLoS One*, vol. 10, no. 6, p. e0129960, 2015.

[95] N. Dossi, R. Toniolo, F. Impellizzieri, and G. Bontempelli, "Doped pencil leads for drawing modified electrodes on paper-based electrochemical devices," *J. Electroanal. Chem.*, vol. 722–723, pp. 90–94, 2014.

[96] X. Z. Niu, S. L. Peng, L. Y. Liu, W. J. Wen, and P. Sheng, "Characterizing and Patterning of PDMS-Based Conducting Composites," *Adv. Mater.*, vol. 19, no. 18, pp. 2682–2686, 2007.

[97] S. H. Ko, H. Pan, C. P. Grigoropoulos, C. K. Luscombe, J. M. J. Fréchet, and D. Poulikakos, "All-inkjet-printed flexible electronics fabrication on a polymer substrate by low-temperature high-resolution selective laser sintering of metal nanoparticles," *Nanotechnology*, vol. 18, no. 34, p. 345202, 2007.

[98] D. A. Bartholomeusz, R. W. Boutté, and J. D. Andrade, "Xurography: Rapid prototyping of microstructures using a cutting plotter," *J. Microelectromechanical Syst.*, vol. 14, no. 6, pp. 1364–1374, 2005.

[99] W. Wang, M. R. Holl, and D. T. Schwartz, "Rapid Prototyping of Masks for

Through-Mask Electrodeposition of Thick Metallic Components," *J. Electrochem. Soc.*, vol. 148, no. 5, pp. C363–C368, 2001.

[100] L. Wang, R. Kodzius, X. Yi, S. Li, Y. S. Hui, and W. Wen, "Prototyping chips in minutes: Direct Laser Plotting (DLP) of functional microfluidic structures," *Sensors Actuators B Chem.*, vol. 168, pp. 214–222, 2012.

[101] D. P. Manica and A. G. Ewing, "Prototyping disposable electrophoresis microchips with electrochemical detection using rapid marker masking and laminar flow etching," *Electrophoresis*, vol. 23, pp. 3735–3743, 2002.

[102] M. Abdelgawad and A. R. Wheeler, "Low-cost, rapid-prototyping of digital microfluidics devices," *Microfluid. Nanofluidics*, vol. 4, no. 4, pp. 349–355, 2008.

[103] W. K. Tomazelli Coltro, J. A. Fracassi da Silva, and E. Carrilho, "Rapid prototyping of polymeric electrophoresis microchips with integrated copper electrodes for contactless conductivity detection," *Anal. Methods*, vol. 3, no. 1, pp. 168–172, 2011.

[104] M. Vazquez, C. Frankenfeld, W. K. Coltro, E. Carrilho, D. Diamond, and S. M. Lunte, "Dual contactless conductivity and amperometric detection on hybrid PDMS/glass electrophoresis microchips," *Analyst*, vol. 135, no. 1, pp. 96–103, 2010.

[105] W. K. T. Coltro, D. P. De Jesus, J. A. F. Da Silva, C. L. Do Lago, and E. Carrilho, "Toner and paper-based fabrication techniques for microfluidic applications," *Electrophoresis*, vol. 31, no. 15, pp. 2487–2498, 2010.

[106] X. Liu, B. Choi, N. Gozubenli, and P. Jiang, "Periodic arrays of metal nanorings and nanocrescents fabricated by a scalable colloidal templating approach," *J. Colloid Interface Sci.*, vol. 409, no. C, pp. 52–58, 2013.

[107] A. M. Md Jani, D. Losic, and N. H. Voelcker, "Nanoporous anodic aluminium oxide: Advances in surface engineering and emerging applications," *Prog. Mater. Sci.*, vol. 58, no. 5, pp. 636–704, 2013.

[108] N. Kurra and G. U. Kulkarni, "Pencil-on-paper: electronic devices.," *Lab Chip*, vol. 13, no. 15, pp. 2866–2873, 2013.

[109] B. J. L. Wilbur, A. Kumar, E. Kim, and G. M. Whitesides, "Microfabrication by Microcontact Printing of Self-Assembled Monolayers," *Adv. Mater.*, vol. 6, no. 7 8, pp. 600–604, 1994.

[110] M. H. Lee, J. Y. Lin, and T. W. Odom, "Large-Area Nanocontact Printing with Metallic Nanostencil Masks," *Angew. Chemie*, vol. 122, no. 17, pp. 3121–3124, 2010.

[111] A. Kamyshny and S. Magdassi, “Conductive Nanomaterials for Printed Electronics,” *Small*, vol. 10, no. 17, pp. 3515–3535, 2014.

[112] A. Toossi, M. Daneshmand, and D. Sameoto, “A low-cost rapid prototyping method for metal electrode fabrication using a CO 2 laser cutter,” *J. Micromechanics Microengineering*, vol. 23, no. 4, p. 047001, 2013.

[113] K. K. B. Hon, L. Li, and I. M. Hutchings, “Direct writing technology—Advances and developments,” *CIRP Ann. - Manuf. Technol.*, vol. 57, no. 2, pp. 601–620, 2008.

[114] A. Singh, N. J. English, and K. M. Ryan, “Highly ordered nanorod assemblies extending over device scale areas and in controlled multilayers by electrophoretic deposition,” *J. Phys. Chem. B*, vol. 117, no. 6, pp. 1608–1615, 2013.

[115] L. P. Bicelli, B. Bozzini, C. Mele, and L. D. Urzo, “A Review of Nanostructural Aspects of Metal Electrodeposition,” *Int. J. Electrochem. Sci.*, vol. 3, pp. 356–408, 2008.

[116] A. Schweikart, A. Horn, A. Böker, and A. Fery, “Controlled wrinkling as a novel method for the fabrication of patterned surfaces,” *Adv. Polym. Sci.*, vol. 227, no. 1, pp. 75–99, 2010.

[117] G. C. Martin, T. T. Su, I. H. Loh, E. Balizer, S. T. Kowel, and P. Kornreich, “The metallization of silicone polymers in the rubbery and the glassy state,” *J. Appl. Phys.*, vol. 53, no. 1, pp. 797–799, 1982.

[118] N. Bowden, S. Brittain, and A. Evans, “Spontaneous formation of ordered structures in thin films of metals supported on an elastomeric polymer,” *Nature*, vol. 393, no. May, pp. 146–149, 1998.

[119] J. Groenewold, “Wrinkling of plates coupled with soft elastic media,” *Phys. A Stat. Mech. its Appl.*, vol. 298, no. 1–2, pp. 32–45, Sep. 2001.

[120] W. T. S. Huck, N. Bowden, P. Onck, T. Pardoen, J. W. Hutchinson, and G. M. Whitesides, “Ordering of spontaneously formed buckles on planar surfaces,” *Langmuir*, vol. 16, no. 7, pp. 3497–3501, 2000.

[121] J. Genzer and J. Groenewold, “Soft matter with hard skin: From skin wrinkles to templating and material characterization,” *Soft Matter*, vol. 2, no. 4, pp. 310–323, 2006.

[122] K. Efimenko, M. Rackaitis, E. Manias, A. Vaziri, L. Mahadevan, and J. Genzer, “Nested self-similar wrinkling patterns in skins.,” *Nat. Mater.*, vol. 4, no. 4, pp. 293–297, Apr. 2005.

[123] E. Cerda, K. Ravi-Chandar, and L. Mahadevan, “Thin films. Wrinkling of an

elastic sheet under tension.," *Nature*, vol. 419, no. 6907, pp. 579–580, 2002.

[124] A. L. Volynskii, S. Bazhenov, O. V. Lebedeva, and N. F. Bakeev, "Mechanical buckling instability of thin coatings deposited on soft polymer substrates," *J. Mater. Sci.*, vol. 35, no. 3, pp. 547–554, 2000.

[125] S. Timoshenko, *Theory of Elastic Stability*. New York: McGraw-Hill, 1988.

[126] M. A. Biot, "Folding Instability of a Layered Viscoelastic Medium under Compression," *Proc. R. Soc. A Math. Phys. Eng. Sci.*, vol. 242, no. 1231, pp. 444–454, 1957.

[127] J. Y. Chung, A. J. Nolte, and C. M. Stafford, "Surface wrinkling: a versatile platform for measuring thin-film properties.," *Adv. Mater.*, vol. 23, no. 3, pp. 349–368, Jan. 2011.

[128] C.-C. C. Fu, A. Grimes, M. Long, C. G. L. Ferri, B. D. Rich, S. S. Ghosh, S. S. Ghosh, L. P. Lee, A. Gopinathan, and M. Khine, "Tunable Nanowrinkles on Shape Memory Polymer Sheets," *Adv. Mater.*, vol. 21, no. 44, pp. 4472–4476, Nov. 2009.

[129] P. Kim, M. Abkarian, and H. A. Stone, "Hierarchical folding of elastic membranes under biaxial compressive stress," *Nat. Mater.*, vol. 10, no. 12, pp. 952–957, 2011.

[130] A. Verma, A. Sharma, and G. U. Kulkarni, "Ultrafast large-area micropattern generation in nonabsorbing polymer thin films by pulsed laser diffraction," *Small*, vol. 7, no. 6, pp. 758–765, 2011.

[131] M. Guvendiren, J. A. Burdick, and S. Yang, "Solvent induced transition from wrinkles to creases in thin film gels with depth-wise crosslinking gradients," *Soft Matter*, vol. 6, pp. 5795–5801, 2010.

[132] M. Watanabe, "Striped-pattern formation of a thin gold film deposited onto a stretched elastic silicone substrate," *J. Polym. Sci. Part B Polym. Phys.*, vol. 43, no. 12, pp. 1532–1537, 2005.

[133] S. P. Lacour, S. Wagner, Z. Huang, and Z. Suo, "Stretchable gold conductors on elastomeric substrates," *Appl. Phys. Lett.*, vol. 82, no. 15, p. 2404, 2003.

[134] S. P. Lacour, J. Jones, Z. Suo, and S. Wagner, "Design and performance of thin metal film interconnects for skin-like electronic circuits," *IEEE Electron Device Lett.*, vol. 25, no. 4, pp. 179–181, 2004.

[135] N. Bowden, S. Brittain, and A. Evans, "Spontaneous formation of ordered structures in thin films of metals supported on an elastomeric polymer," *Nature*, vol. 393, no. May, pp. 146–149, 1998.

[136] M. Watanabe and T. Hirai, "Polypyrrole film with striped pattern," *J. Polym. Sci. Part B Polym. Phys.*, vol. 42, no. 13, pp. 2460–2466, 2004.

[137] S. Lin, E. K. Lee, and M. Khine, "Thermally-induced miniaturization for micro- and nanofabrication: progress and updates," *Lab Chip*, vol. 14, pp. 3475–3488, 2014.

[138] D. Nguyen, D. Taylor, K. Qian, N. Norouzi, J. Rasmussen, S. Botzet, M. Lehmann, K. Halverson, and M. Khine, "Better shrinkage than Shrinky-Dinks.," *Lab Chip*, vol. 10, no. 12, pp. 1623–1626, Jun. 2010.

[139] C.-C. Fu, G. Ossato, M. Long, M. A. Digman, A. Gopinathan, L. P. Lee, E. Gratton, and M. Khine, "Bimetallic nanopetals for thousand-fold fluorescence enhancements," *Appl. Phys. Lett.*, vol. 97, no. 20, p. 203101, 2010.

[140] H. Sharma, M. A. Digman, N. Felsinger, E. Gratton, and M. Khine, "Enhanced emission of fluorophores on shrink-induced wrinkled composite structures," *Opt. Mater. Express*, vol. 4, no. 4, pp. 753–763, 2014.

[141] L. Zhang, X. Lang, A. Hirata, and M. Chen, "Wrinkled nanoporous gold films with ultrahigh surface-enhanced raman scattering enhancement," *ACS Nano*, vol. 5, no. 6, pp. 4407–4413, 2011.

[142] S.-J. Park, J. Kim, M. Chu, and M. Khine, "Highly Flexible Wrinkled Carbon Nanotube Thin Film Strain Sensor to Monitor Human Movement," *Adv. Mater. Technol.*, vol. 1600053, 2016.

[143] M. R. Aufan, Y. Sumi, S. Kim, and J. Y. Lee, "Facile Synthesis of Conductive Polypyrrole Wrinkle Topographies on Polydimethylsiloxane via a Swelling-Deswelling Process and Their Potential Uses in Tissue Engineering," *ACS Appl. Mater. Interfaces*, vol. 7, no. 42, pp. 23454–23463, 2015.

[144] J. I. Luna, J. Ciriza, M. E. Garcia-Ojeda, M. Kong, A. Herren, D. K. Lieu, R. a Li, C. C. Fowlkes, M. Khine, and K. E. McCloskey, "Multiscale biomimetic topography for the alignment of neonatal and embryonic stem cell-derived heart cells.," *Tissue Eng. Part C. Methods*, vol. 17, no. 5, pp. 579–588, 2011.

[145] M. Li, N. Hakimi, R. Perez, S. Waldman, J. A. Kozinski, and D. K. Hwang, "Microarchitecture for a Three-Dimensional Wrinkled Surface Platform," *Adv. Mater.*, vol. 27, no. 11, pp. 1880–1886, 2015.

[146] L. R. J. Scarratt, B. S. Hoatson, E. S. Wood, B. S. Hawkett, and C. Neto, "Durable Superhydrophobic Surfaces via Spontaneous Wrinkling of Teflon AF," *ACS Appl. Mater. Interfaces*, vol. 8, pp. 6743–6750, 2016.

[147] L. R. Freschauf, J. McLane, H. Sharma, and M. Khine, "Shrink-induced superhydrophobic and antibacterial surfaces in consumer plastics," *PLoS One*, vol. 7, no. 8, pp. 1–7, 2012.

[148] K. Burton, J. H. Park, and D. L. Taylor, "Keratocytes generate traction forces in

two phases.," *Mol. Biol. Cell*, vol. 10, no. 11, pp. 3745–3769, 1999.

[149] Z. Wen, S. Ci, and J. Li, "Pt Nanoparticles Inserting in Carbon Nanotube Arrays: Nanocomposites for Glucose Biosensors," *J. Phys. Chem. C*, vol. 113, no. 31, pp. 13482–13487, Aug. 2009.

[150] Y. Luo and V. Misra, "Large-area long-range ordered anisotropic magnetic nanostructure fabrication by photolithography," *Nanotechnology*, vol. 17, no. 19, pp. 4909–4911, Oct. 2006.

[151] H. Duan, J. Zhao, Y. Zhang, E. Xie, and L. Han, "Preparing patterned carbonaceous nanostructures directly by overexposure of PMMA using electron-beam lithography.," *Nanotechnology*, vol. 20, no. 13, p. 135306, Apr. 2009.

[152] R. Inguanta, S. Piazza, and C. Sunseri, "Template electrosynthesis of CeO 2 nanotubes," *Nanotechnology*, vol. 18, no. 48, p. 485605, Dec. 2007.

[153] Y. Xia and G. M. Whitesides, "Soft Lithography," *Annu. Rev. Mater. Sci.*, vol. 28, no. 1, pp. 153–184, 1998.

[154] A. Grimes, D. N. Breslauer, M. Long, J. Pegan, L. P. Lee, and M. Khine, "Shrinky-Dink microfluidics: rapid generation of deep and rounded patterns.," *Lab Chip*, vol. 8, no. 1, pp. 170–172, Jan. 2008.

[155] W. M. Haynes, *CRC Handbook of chemistry and physics*. Boca Raton, FL, Fla.; London: Taylor & Francis, 2011.

[156] Y. Shao and M. A. Brook, "Structured metal films on silicone elastomers," *J. Mater. Chem.*, vol. 20, no. 39, pp. 8548–8556, 2010.

[157] C. M. Stafford, C. Harrison, K. L. Beers, A. Karim, E. J. Amis, M. R. VanLandingham, H.-C. Kim, W. Volksen, R. D. Miller, and E. E. Simonyi, "A buckling-based metrology for measuring the elastic moduli of polymeric thin films.," *Nat. Mater.*, vol. 3, no. 8, pp. 545–550, Aug. 2004.

[158] P. Yoo and H. Lee, "Evolution of a Stress-Driven Pattern in Thin Bilayer Films: Spinodal Wrinkling," *Phys. Rev. Lett.*, vol. 91, no. 15, pp. 8–11, Oct. 2003.

[159] P. Yoo, K. Suh, H. Kang, and H. Lee, "Polymer Elasticity-Driven Wrinkling and Coarsening in High Temperature Buckling of Metal-Capped Polymer Thin Films," *Phys. Rev. Lett.*, vol. 93, no. 3, pp. 1–4, Jul. 2004.

[160] J. S. Sharp, D. Vader, J. A. Forrest, M. I. Smith, M. Khomenko, and K. Dalnoki-Veress, "Spinodal wrinkling in thin-film poly(ethylene oxide)/polystyrene bilayers.," *Eur. Phys. J. E. Soft Matter*, vol. 19, no. 4, pp. 423–432, Apr. 2006.

[161] Z. Huang, W. Hong, and Z. Suo, "Evolution of wrinkles in hard films on soft substrates," *Phys. Rev. E*, vol. 70, no. 3, pp. 3–6, Sep. 2004.

[162] A. Shahraz, A. Borhan, and K. A. Fichthorn, “A theory for the morphological dependence of wetting on a physically patterned solid surface.,” *Langmuir*, vol. 28, no. 40, pp. 14227–14237, Oct. 2012.

[163] M. C. Choi, Y. Kim, and C. S. Ha, “Polymers for flexible displays: From material selection to device applications,” *Progress in Polymer Science (Oxford),* vol. 33, no. 6. pp. 581–630, 2008.

[164] M. C. McAlpine, H. Ahmad, D. Wang, and J. R. Heath, “Highly ordered nanowire arrays on plastic substrates for ultrasensitive flexible chemical sensors.,” *Nat. Mater.*, vol. 6, no. 5, pp. 379–384, May 2007.

[165] T. Soderstrom, F. J. Haug, V. Terrazzoni-Daudrix, and C. Ballif, “Optimization of amorphous silicon thin film solar cells for flexible photovoltaics,” *J. Appl. Phys.*, vol. 103, no. 11, p. 114509, 2008.

[166] H. K. Chae, D. Y. Siberio-Pérez, J. Kim, Y. Go, M. Eddaoudi, A. J. Matzger, M. O’Keeffe, and O. M. Yaghi, “A route to high surface area, porosity and inclusion of large molecules in crystals.,” *Nature*, vol. 427, no. February, pp. 523–527, 2004.

[167] Y. Li, Z.-Y. Fu, and B.-L. Su, “Hierarchically Structured Porous Materials for Energy Conversion and Storage,” *Adv. Funct. Mater.*, vol. 22, no. 22, pp. 4634–4667, 2012.

[168] A. J. Bard and L. R. Faulkner, *Electrochemical methods: fundamentals and applications*, 2nd ed. New York: John Wiley & Son, Inc., 2001.

[169] W. R. Osório, L. C. Peixoto, M. V. Canté, and A. Garcia, “Electrochemical corrosion characterization of Al-Ni alloys in a dilute sodium chloride solution,” *Electrochim. Acta*, vol. 55, no. 13, pp. 4078–4085, 2010.

[170] S. Sriram, M. Bhaskaran, R. Ahluwalia, T. G. Nguyen, N. Ng, D. J. Srolovitz, K. Kalantar-Zadeh, and A. Mitchell, “Surface morphology induced localized electric field and piezoresponse enhancement in nanostructured thin films.,” *ACS Nano*, vol. 5, no. 2, pp. 1067–1072, Feb. 2011.

[171] H.-Y. Gu, A.-M. Yu, and H.-Y. Chen, “Direct electron transfer and characterization of hemoglobin immobilized on a Au colloid–cysteamine-modified gold electrode,” *J. Electroanal. Chem.*, vol. 516, no. 1–2, pp. 119–126, Dec. 2001.

[172] S. Bharathi, M. Nogami, and S. Ikeda, “Novel Electrochemical Interfaces with a Tunable Kinetic Barrier by Self-Assembling Organically Modified Silica Gel and Gold Nanoparticles,” *Langmuir*, vol. 17, no. 1, pp. 1–4, Jan. 2001.

[173] S. Yang and R. E. R. Rothman, “Review PCR-based diagnostics for infectious diseases : uses , limitations , and future applications in acute-care settings,” *Lancet Infect. Dis.*, vol. 4, pp. 337–348, 2004.

[174] T. S. Hauck, S. Giri, Y. Gao, and W. C. W. Chan, “Nanotechnology diagnostics for infectious diseases prevalent in developing countries.,” *Adv. Drug Deliv. Rev.*, vol. 62, no. 4–5, pp. 438–448, Mar. 2010.

[175] C. D. Chin, V. Linder, and S. K. Sia, “Lab-on-a-chip devices for global health: past studies and future opportunities.,” *Lab Chip*, vol. 7, no. 1, pp. 41–57, Jan. 2007.

[176] J. El-Ali, P. K. Sorger, and K. F. Jensen, “Cells on chips.,” *Nature*, vol. 442, no. 7101, pp. 403–411, Jul. 2006.

[177] S. Choi, M. Goryll, L. Y. M. Sin, P. K. Wong, and J. Chae, “Microfluidic-based biosensors toward point-of-care detection of nucleic acids and proteins,” *Microfluid. Nanofluidics*, vol. 10, no. 2, pp. 231–247, Jun. 2010.

[178] L. Nan, Z. Jiang, and X. Wei, “Emerging microfluidic devices for cell lysis: A review,” *Lab Chip*, vol. 14, no. 6, pp. 1060–1073, 2014.

[179] D. Irimia, R. G. Tompkins, and M. Toner, “Single-cell chemical lysis in picoliter-scale closed volumes using a microfabricated device.,” *Anal. Chem.*, vol. 76, no. 20, pp. 6137–6143, Oct. 2004.

[180] E. A. Schilling, A. E. Kamholz, and P. Yager, “Cell lysis and protein extraction in a microfluidic device with detection by a fluorogenic enzyme assay.,” *Anal. Chem.*, vol. 74, no. 8, pp. 1798–1804, Apr. 2002.

[181] T. Niwa, Y. Kawamura, Y. Katagiri, and T. Ezaki, “Lytic enzyme, labiase for a broad range of Gram-positive bacteria and its application to analyze functional DNA/RNA.,” *J. Microbiol. Methods*, vol. 61, no. 2, pp. 251–260, May 2005.

[182] H. Kido, M. Micic, D. Smith, J. Zoval, J. Norton, and M. Madou, “A novel, compact disk-like centrifugal microfluidics system for cell lysis and sample homogenization.,” *Colloids Surf. B. Biointerfaces*, vol. 58, no. 1, pp. 44–51, Jul. 2007.

[183] J. Kim, S. H. Jang, G. Jia, J. V Zoval, N. A. Da Silva, and M. J. Madou, “Cell lysis on a microfluidic CD (compact disc).,” *Lab Chip*, vol. 4, no. 5, pp. 516–522, Oct. 2004.

[184] C.-Y. Lee, G.-B. Lee, J.-L. Lin, F.-C. Huang, and C.-S. Liao, “Integrated microfluidic systems for cell lysis, mixing/pumping and DNA amplification,” *J. Micromechanics Microengineering*, vol. 15, no. 6, pp. 1215–1223, Jun. 2005.

[185] R. H. Liu, J. Yang, R. Lenigk, J. Bonanno, and P. Grodzinski, “Self-contained, fully integrated biochip for sample preparation, polymerase chain reaction amplification, and DNA microarray detection.,” *Anal. Chem.*, vol. 76, no. 7, pp. 1824–1831, Apr. 2004.

[186] N. Bao and C. Lu, “A microfluidic device for physical trapping and electrical lysis of bacterial cells,” *Appl. Phys. Lett.*, vol. 92, no. 21, pp. 214103(1–3), 2008.

[187] J. Cheng, E. L. Sheldon, L. Wu, A. Uribe, L. O. Gerrue, J. Carrino, M. J. Heller, and J. P. O’Connell, “Preparation and hybridization analysis of DNA/RNA from E.Coli on microfabricated bioelectronic chips,” *Nat. Biotechnol.*, vol. 16, pp. 541–546, 1998.

[188] S. Lee and Y. Tai, “A micro cell lysis device,” *Sensors Actuators A Phys.*, vol. 73, pp. 74–79, 1999.

[189] Q. Ramadan, V. Samper, D. Poenar, Z. Liang, C. Yu, and T. M. Lim, “Simultaneous cell lysis and bead trapping in a continuous flow microfluidic device,” *Sensors Actuators B Chem.*, vol. 113, no. 2, pp. 944–955, Feb. 2006.

[190] T. Geng and C. Lu, “Microfluidic electroporation for cellular analysis and delivery.,” *Lab Chip*, vol. 13, no. 19, pp. 3803–3821, Oct. 2013.

[191] H. Lu, M. A. Schmidt, and K. F. Jensen, “A microfluidic electroporation device for cell lysis.,” *Lab Chip*, vol. 5, no. 1, pp. 23–29, Jan. 2005.

[192] H.-Y. Wang and C. Lu, “Microfluidic electroporation for delivery of small molecules and genes into cells using a common DC power supply.,” *Biotechnol. Bioeng.*, vol. 100, no. 3, pp. 579–586, Jun. 2008.

[193] D. W. Lee and Y.-H. Cho, “A continuous electrical cell lysis device using a low dc voltage for a cell transport and rupture,” *Sensors Actuators B Chem.*, vol. 124, no. 1, pp. 84–89, Jun. 2007.

[194] M. Mishra, A. Krishna, A. Chandra, B. M. Shenoy, G. M. Hegde, and D. R. Mahapatra, “Charge injection through nanocomposite electrode in microfluidic channel for electrical lysis of biological cells,” in *Proceedings of SPIE*, 2013, vol. 8570, no. ii, p. 85700R (1–8).

[195] K.-Y. Lu, A. M. Wo, Y.-J. Lo, K.-C. Chen, C.-M. Lin, and C.-R. Yang, “Three dimensional electrode array for cell lysis via electroporation.,” *Biosens. Bioelectron.*, vol. 22, no. 4, pp. 568–574, Oct. 2006.

[196] J. V Barth, G. Costantini, and K. Kern, “Engineering atomic and molecular nanostructures at surfaces.,” *Nature*, vol. 437, no. 7059, pp. 671–679, Sep. 2005.

[197] V. Ananthakrishnan, R. Sarma, and G. K. Ananthasuresh, “Systematic mask synthesis for surface micromachined microelectromechanical systems,” *J. Micromechanics Microengineering*, vol. 13, no. 6, pp. 927–941, Nov. 2003.

[198] J. Lu, C. Perng, and S. Lee, “Use of PCR with Universal Primers and Restriction Endonuclease Digestions for Detection and Identification of Common Bacterial

Pathogens in Cerebrospinal Fluid Use of PCR with Universal Primers and Restriction Endonuclease Digestions for Detection and Ide,” *J. Clin. Microbiol.*, vol. 38, no. 6, pp. 2076–2080, 2000.

[199] C. M. Gabardo, Y. Zhu, L. Soleymani, and J. M. Moran-Mirabal, “Bench-top fabrication of hierarchically structured high-surface-area electrodes,” *Adv. Funct. Mater.*, vol. 23, no. 24, pp. 3030–3039, Jan. 2013.

[200] D. Di Carlo, C. Ionescu-Zanetti, Y. Zhang, P. Hung, and L. P. Lee, “On-chip cell lysis by local hydroxide generation.,” *Lab Chip*, vol. 5, no. 2, pp. 171–178, Feb. 2005.

[201] “LIVE / DEAD ® BacLight Bacterial Viability Kits Product Information,” 2004.

[202] D. Di Carlo, K.-H. Jeong, and L. P. Lee, “Reagentless mechanical cell lysis by nanoscale barbs in microchannels for sample preparation.,” *Lab Chip*, vol. 3, no. 4, pp. 287–291, Nov. 2003.

[203] M. Packard, E. Wheeler, E. Alocilja, and M. Shusteff, “Performance Evaluation of Fast Microfluidic Thermal Lysis of Bacteria for Diagnostic Sample Preparation,” *Diagnostics*, vol. 3, no. 1, pp. 105–116, Jan. 2013.

[204] A. F. Mendonca, T. L. Amoroso, and S. J. Knabel, “Destruction of Gram-Negative Food-Borne Pathogens by High pH Involves Disruption of the Cytoplasmic Membrane,” vol. 60, no. 11, pp. 4009–4014, 1994.

[205] H.-Y. Wang, A. K. Bhunia, and C. Lu, “A microfluidic flow-through device for high throughput electrical lysis of bacterial cells based on continuous dc voltage.,” *Biosens. Bioelectron.*, vol. 22, no. 5, pp. 582–588, Dec. 2006.

[206] P. S. Dittrich and A. Manz, “Lab-on-a-chip: microfluidics in drug discovery.,” *Nat. Rev. Drug Discov.*, vol. 5, no. 3, pp. 210–218, Mar. 2006.

[207] P. Neuži, S. Giselbrecht, K. Länge, T. J. Huang, and A. Manz, “Revisiting lab-on-a-chip technology for drug discovery,” *Nat. Rev. Drug Discov.*, vol. 11, no. August, pp. 620–632, 2012.

[208] J. Mairhofer, K. Roppert, and P. Ertl, “Microfluidic systems for pathogen sensing: A review,” *Sensors*, vol. 9, pp. 4804–4823, 2009.

[209] J. C. Jokerst, J. M. Emory, and C. S. Henry, “Advances in microfluidics for environmental analysis,” *Analyst*, vol. 137, pp. 24–34, 2012.

[210] Á. Ríos, M. Zougagh, and M. Avila, “Miniaturization through lab-on-a-chip: Utopia or reality for routine laboratories? A review,” *Anal. Chim. Acta*, vol. 740, pp. 1–11, 2012.

[211] N. Y. Lee and B. H. Chung, “Novel poly(dimethylsiloxane) bonding strategy via

room temperature ‘chemical gluing,’” *Langmuir*, vol. 25, no. 16, pp. 3861–3866, 2009.

[212] M. A. Eddings, M. A. Johnson, and B. K. Gale, “Determining the optimal PDMS–PDMS bonding technique for microfluidic devices,” *J. Micromechanics Microengineering*, vol. 18, no. 6, p. 067001, Jun. 2008.

[213] W. W. Y. Chow, K. F. Lei, G. Shi, W. J. Li, and Q. Huang, “Microfluidic channel fabrication by PDMS-interface bonding,” *Smart Mater. Struct.*, vol. 15, pp. S112–S116, 2005.

[214] F. Darain, K. L. Gan, and S. C. Tjin, “Antibody immobilization on to polystyrene substrate--on-chip immunoassay for horse IgG based on fluorescence.,” *Biomed. Microdevices*, vol. 11, no. 3, pp. 653–661, Jun. 2009.

[215] A. Bubendorfer, X. Liu, and A. V Ellis, “Microfabrication of PDMS microchannels using SU-8/PMMA moldings and their sealing to polystyrene substrates,” *Smart Mater. Struct.*, vol. 16, no. 2, pp. 367–371, Apr. 2007.

[216] L. Tang and N. Y. Lee, “A facile route for irreversible bonding of plastic-PDMS hybrid microdevices at room temperature.,” *Lab Chip*, vol. 10, pp. 1274–1280, 2010.

[217] V. Sunkara, D.-K. Park, H. Hwang, R. Chantiwas, S. a Soper, and Y.-K. Cho, “Simple room temperature bonding of thermoplastics and poly(dimethylsiloxane).,” *Lab Chip*, vol. 11, no. 5, pp. 962–965, Mar. 2011.

[218] M.-E. Vlachopoulou, a Tserepi, P. Pavli, P. Argitis, M. Sanopoulou, and K. Misiakos, “A low temperature surface modification assisted method for bonding plastic substrates,” *J. Micromechanics Microengineering*, vol. 19, no. 1, p. 015007, Jan. 2009.

[219] S. Sonney, N. Shek, and J. M. Moran-Mirabal, “Rapid bench-top fabrication of poly(dimethylsiloxane)/polystyrene microfluidic devices incorporating high-surface-area sensing electrodes,” *Biomicrofluidics*, no. 9, p. 026501, 2015.

[220] X. Li, N. Wu, Y. Rojanasakul, and Y. Liu, “Selective stamp bonding of PDMS microfluidic devices to polymer substrates for biological applications,” *Sensors Actuators, A Phys.*, vol. 193, pp. 186–192, 2013.

[221] S. M. Woo, C. M. Gabardo, and L. Soleymani, “Prototyping of Wrinkled Nano-/Microstructured Electrodes for Electrochemical DNA Detection.,” *Anal. Chem.*, vol. 86, pp. 12341–12347, Nov. 2014.

[222] C. M. Gabardo, A. M. Kwong, and L. Soleymani, “Rapidly prototyped multi-scale electrodes to minimize the voltage requirements for bacterial cell lysis,” *Analyst*, vol. 140, no. 5, pp. 1599–1608, 2015.

[223] A. Hosseini and L. Soleymani, “Benchtop fabrication of multi-scale micro-electromagnets for capturing magnetic particles,” *Appl. Phys. Lett.*, vol. 105, no. 7, p. 074102, Aug. 2014.

[224] J. D. Pegan, A. Y. Ho, M. Bachman, and M. Khine, “Flexible shrink-induced high surface area electrodes for electrochemiluminescent sensing.,” *Lab Chip*, vol. 13, no. 21, pp. 4205–4209, 2013.

[225] H. Sharma, J. B. Wood, S. Lin, R. M. Corn, and M. Khine, “Shrink-Induced Silica Multiscale Structures for Enhanced Fluorescence from DNA Microarrays,” *Langmuir*, vol. 30, pp. 10979–10983, 2014.

[226] B. G. Subramani and P. R. Selvaganapathy, “Surface micromachined PDMS microfluidic devices fabricated using a sacrificial photoresist,” *J. Micromechanics Microengineering*, vol. 19, p. 015013, 2008.

[227] M. L. Kovarik, N. J. Torrence, D. M. Spence, and R. S. Martin, “Fabrication of carbon microelectrodes with a micromolding technique and their use in microchip-based flow analyses.,” *Analyst*, vol. 129, no. January, pp. 400–405, 2004.

[228] J. T. Borenstein, M. M. Tupper, P. J. Mack, E. J. Weinberg, A. S. Khalil, J. Hsiao, and G. García-Cardeña, “Functional endothelialized microvascular networks with circular cross-sections in a tissue culture substrate.,” *Biomed. Microdevices*, vol. 12, no. 1, pp. 71–79, Feb. 2010.

[229] P. Rezai, P. R. Selvaganapathy, and G. R. Wohl, “Plasma enhanced bonding of polydimethylsiloxane with parylene and its optimization,” *J. Micromechanics Microengineering*, vol. 21, no. 6, p. 065024, Jun. 2011.

[230] S. Varma and J. Voldman, “A cell-based sensor of fluid shear stress for microfluidics,” *Lab Chip*, vol. 15, pp. 1563–1573, 2015.

[231] H. Hillborg, J. F. Ankner, U. W. Gedde, G. D. Smith, H. K. Yasuda, and K. Wikstro, “Crosslinked polydimethylsiloxane exposed to oxygen plasma studied by neutron reflectometry and other surface specific techniques,” *Polymer (Guildf).*, vol. 41, pp. 6851–6863, 2000.

[232] N.-T. Nguyen, X. Huang, and T. K. Chuan, “MEMS-Micropumps: A Review,” *J. Fluids Eng.*, vol. 124, no. June 2002, pp. 384–392, 2002.

[233] F. Chen, X. Li, J. Hihath, Z. Huang, and N. Tao, “Effect of anchoring groups on single-molecule conductance: Comparative study of thiol-, amine-, and carboxylic-acid-terminated molecules,” *J. Am. Chem. Soc.*, vol. 128, no. 18, pp. 15874–15881, 2006.

[234] V. Sunkara and Y. Cho, “Investigation on the Mechanism of Aminosilane-Mediated Bonding of Thermoplastics and Poly(dimethylsiloxane),” *ACS Appl.*

*Mater. Interfaces*, vol. 4, pp. 6537–6544, 2012.

[235] A. T. Ciftlik and M. A. M. Gijs, “A low-temperature parylene-to-silicon dioxide bonding technique for high-pressure microfluidics,” *J. Micromechanics Microengineering*, vol. 21, p. 035011, 2011.

[236] F. J. del Campo, “Miniaturization of electrochemical flow devices,” *Electrochem. commun.*, vol. 45, pp. 91–94, Aug. 2014.

[237] L. Soleymani, Z. C. Fang, E. H. Sargent, and S. O. Kelley, “Programming the detection limits of biosensors through controlled nanostructuring,” *Nat. Nanotechnol.*, vol. 4, no. 12, pp. 844–848, 2009.

[238] V. Gau, S. Ma, H. Wang, J. Tsukuda, J. Kibler, and D. Haake, “Electrochemical molecular analysis without nucleic acid amplification,” *Methods*, vol. 37, no. 1, pp. 73–83, 2005.

[239] N. Stevens and A. Fisher, “Finite element simulations in electrochemistry. 2. Hydrodynamic voltammetry,” *J. Phys. Chem. B*, vol. 5647, no. 1, pp. 8259–8263, 1997.

[240] N. Manaresi, A. Romani, G. Medoro, L. Altomare, A. Leonardi, M. Tartagni, and R. Guerrieri, “A CMOS Chip for Individual Cell Manipulation and Detection,” *IEEE J. Solid-State Circuits*, vol. 38, no. 12, pp. 2297–2305, 2003.

[241] T. A. Nguyen, T. I. Yin, D. Reyes, and G. A. Urban, “Microfluidic chip with integrated electrical cell-impedance sensing for monitoring single cancer cell migration in three-dimensional matrixes,” *Anal. Chem.*, vol. 85, no. 22, pp. 11068–11076, 2013.

[242] D. Quinton, A. Girard, L. T. Thi Kim, V. Raimbault, L. Griscom, F. Razan, S. Griveau, and F. Bedioui, “On-chip multi-electrochemical sensor array platform for simultaneous screening of nitric oxide and peroxynitrite.,” *Lab Chip*, vol. 11, no. 7, pp. 1342–1350, 2011.

[243] C.-H. Chuang, T.-F. Wu, C.-H. Chen, K.-C. Chang, J.-W. Ju, and Y.-W. Huang, “Lab on a chip for multiplexed immunoassays to detect bladder cancer using multifunctional dielectrophoretic manipulations,” *Lab Chip*, vol. 15, pp. 3056–3064, 2015.

[244] D. P. Dowling, K. Donnelly, M. L. McConnell, R. Eloy, and M. N. Arnaud, “Deposition of anti-bacterial silver coatings on polymeric substrates,” *Thin Solid Films*, vol. 398–399, no. October, pp. 602–606, 2001.

[245] K. Ueno, H. B. Kim, and N. Kitamura, “Characteristic electrochemical responses of polymer microchannel-microelectrode chips,” *Anal. Chem.*, vol. 75, no. 9, pp. 2086–2091, 2003.

[246] J. Wang, “Glucose biosensors: 40 Years of advances and challenges,” *Electroanalysis*, vol. 13, no. 12, pp. 983–988, 2001.

[247] F. Muench, A. Eils, M. E. Toimil-Molares, U. H. Hossain, A. Radetinac, C. Stegmann, U. Kunz, S. Lauterbach, H. J. Kleebe, and W. Ensinger, “Polymer activation by reducing agent absorption as a flexible tool for the creation of metal films and nanostructures by electroless plating,” *Surf. Coatings Technol.*, vol. 242, pp. 100–108, 2014.

[248] F. Greco, A. Bellacicca, M. Gemmi, V. Cappello, V. Mattoli, and P. Milani, “Conducting Shrinkable Nanocomposite Based on Au-Nanoparticle Implanted Plastic Sheet: Tunable Thermally Induced Surface Wrinkling,” *ACS Appl. Mater. Interfaces*, vol. 7, p. 7060−7065, 2015.

[249] M. Leser, J. Pegan, M. El Makkaoui, J. C. Schlatterer, M. Khine, M. Law, and M. Brenowitz, “Protein Footprinting by Pyrite Shrink-Wrap Laminate,” *Lab Chip*, vol. 15, pp. 1381–1388, 2015.

[250] K. C. Grabar, R. G. Freeman, M. B. Hommer, and M. J. Natan, “Preparation and Characterization of Au Colloid Monolayers,” *Anal. Chem.*, vol. 67, no. 4, pp. 735–743, 1995.

[251] J. C. Love, L. A. Estroff, J. K. Kriebel, R. G. Nuzzo, and G. M. Whitesides, “Self-assembled monolayers of thiolates on metals as a form of nanotechnology.,” *Chem. Rev.*, vol. 105, no. 4, pp. 1103–1169, Apr. 2005.

[252] J. C. Love, D. B. Wolfe, R. Haasch, M. L. Chabinyc, K. E. Paul, G. M. Whitesides, and R. G. Nuzzo, “Formation and structure of self-assembled monolayers of alkanethiolates on palladium.,” *J. Am. Chem. Soc.*, vol. 125, no. 9, pp. 2597–2609, Mar. 2003.

[253] J. Hu, W. Li, J. Chen, X. Zhang, and X. Zhao, “Novel plating solution for electroless deposition of gold film onto glass surface,” *Surf. Coatings Technol.*, vol. 202, no. 13, pp. 2922–2926, Mar. 2008.

[254] P. Daggumati, Z. Matharu, and E. Seker, “Effect of Nanoporous Gold Thin Film Morphology on Electrochemical DNA Sensing,” *Anal. Chem.*, vol. 87, no. 16, pp. 8149–8156, 2015.

[255] A. S. Aricò, P. Bruce, B. Scrosati, J. Tarascon, W. V. A. N. Schalkwijk, U. De Picardie, J. Verne, and C. Umr-, “Nanostructured materials for advanced energy conversion and storage devices,” *Nat. Mater.*, vol. 4, pp. 366–377, 2005.

[256] M. Fan, G. F. S. Andrade, and A. G. Brolo, “A review on the fabrication of substrates for surface enhanced Raman spectroscopy and their applications in analytical chemistry,” *Anal. Chim. Acta*, vol. 693, no. 1–2, pp. 7–25, 2011.

[257] R. A. Tripp, R. A. Dluhy, and Y. Zhao, "Novel nanostructures for SERS biosensing," *Nano Today*, vol. 3, no. 3–4, pp. 31–37, 2008.

[258] B. Sharma, R. R. Frontiera, A.-I. Henry, E. Ringe, and R. P. Van Duyne, "SERS: Materials, applications, and the future," *Mater. Today*, vol. 15, no. 1–2, pp. 16–25, 2012.

[259] F. Xia and L. Jiang, "Bio-inspired, smart, multiscale interfacial materials," *Adv. Mater.*, vol. 20, no. 15, pp. 2842–2858, 2008.

[260] H. Zhou, X. Li, T. Fan, F. E. Osterloh, J. Ding, E. M. Sabio, D. Zhang, and Q. Guo, "Artificial inorganic leafs for efficient photochemical hydrogen production inspired by natural photosynthesis," *Adv. Mater.*, vol. 22, pp. 951–956, 2010.

[261] D.-W. Wang, F. Li, M. Liu, G. Q. Lu, and H.-M. Cheng, "3D Aperiodic Hierarchical Porous Graphitic Carbon for High Rate," *Angew. Chemie*, vol. 47, pp. 373–376, 2008.

[262] C. Zhang, C. Li, S. Huang, Z. Hou, Z. Cheng, P. Yang, C. Peng, and J. Lin, "Self-activated luminescent and mesoporous strontium hydroxyapatite nanorods for drug delivery," *Biomaterials*, vol. 31, no. 12, pp. 3374–3383, 2010.

[263] W. Wei, G. H. Ma, G. Hu, D. Yu, T. Mcleish, Z. G. Su, and Z. Y. Shen, "Preparation of Hierarchical Hollow CaCO3 Particles and the Application as Anticancer Drug Carrier," *J. Am. Chem. Soc.*, vol. 130, no. 47, pp. 15808–15810, 2008.

[264] H. Sharma, D. Nguyen, A. Chen, V. Lew, and M. Khine, "Unconventional low-cost fabrication and patterning techniques for point of care diagnostics," *Ann. Biomed. Eng.*, vol. 39, pp. 1313–1327, 2011.

[265] Y. Mei, S. Kiravittaya, S. Harazim, and O. G. Schmidt, "Principles and applications of micro and nanoscale wrinkles," *Mater. Sci. Eng. R Reports*, vol. 70, no. 3–6, pp. 209–224, 2010.

[266] Y. Zhao, W. M. Huang, and Y. Q. Fu, "Formation of micro/nano-scale wrinkling patterns atop shape memory polymers," *J. Micromechanics Microengineering*, vol. 21, no. 6, p. 067007, 2011.

[267] Y. Zhao, W. M. . Huang, and C. C. Wang, "Thermo/chemo-responsive shape memory effect for micro/nano patterning atop polymers," *Nanosci. Nanotechnol. Lett.*, vol. 4, no. 9, pp. 862–878, 2012.

[268] B. Zhang, M. Zhang, K. Song, Q. Li, and T. Cui, "Shrink induced nanostructures for energy conversion efficiency enhancement in photovoltaic devices," *Appl. Phys. Lett.*, vol. 103, no. 2, p. 023104, 2013.

[269] N. G. Bastús, J. Comenge, and V. Puntes, “Kinetically controlled seeded growth synthesis of citrate-stabilized gold nanoparticles of up to 200 nm: Size focusing versus ostwald ripening,” *Langmuir*, vol. 27, no. 17, pp. 11098–11105, 2011.

[270] Z. Zihua, Z. Tao, and L. Zhongfan, “Raman scattering enhancement contributed from individual gold nanoparticles and interparticle coupling,” *Nanotechnology*, vol. 15, no. 3, pp. 357–364, 2004.

[271] Y. Liu, J. K. Boyles, J. Genzer, and M. D. Dickey, “Self-folding of polymer sheets using local light absorption,” *Soft Matter*, vol. 8, no. 6, pp. 1703–2044, 2012.

[272] X. Xie, W. Zhao, H. R. Lee, C. Liu, M. Ye, W. Xie, B. Cui, C. S. Criddle, and Y. Cui, “Enhancing the nanomaterial bio-interface by addition of mesoscale secondary features: Crinkling of carbon nanotube films to create subcellular ridges,” *ACS Nano*, vol. 8, no. 12, pp. 11958–11965, 2014.

[273] J. Xiao, H. Jiang, D. Y. Khang, J. Wu, Y. Huang, and J. A. Rogers, “Mechanics of buckled carbon nanotubes on elastomeric substrates,” *J. Appl. Phys.*, vol. 104, no. 3, p. 033543, 2008.

[274] D. Khang, J. Xiao, C. Kocabas, and S. Maclaren, “Molecular Scale Buckling Mechanics in Individual Aligned Single-Wall Carbon Nanotubes on Elastomeric Substrates,” *Nano Lett.*, vol. 8, no. 1, pp. 124–130, 2008.

[275] M. Fan and A. G. Brolo, “Silver nanoparticles self assembly as SERS substrates with near single molecule detection limit.,” *Phys. Chem. Chem. Phys.*, vol. 11, no. 34, pp. 7381–7389, 2009.

[276] E. Lejeune, A. Javili, and C. Linder, “Understanding geometric instabilities in thin films via a multi-layer model,” *Soft Matter*, vol. 12, pp. 806–816, 2016.

[277] A. J. Nolte, N. D. Treat, R. E. Cohen, and M. F. Rubner, “Effect of relative humidity on the Young’s modulus of polyelectrolyte multilayer films and related nonionic polymers,” *Macromolecules*, vol. 41, no. 15, pp. 5793–5798, 2008.

[278] S.-Y. Ding, J. Yi, J.-F. Li, B. Ren, D.-Y. Wu, R. Panneerselvam, and Z.-Q. Tian, “Nanostructure-based plasmon-enhanced Raman spectroscopy for surface analysis of materials,” *Nat. Rev. Mater.*, p. 16021 (1–16), 2016.

[279] J. Yin and M. C. Boyce, “Materials science: Unique wrinkles as identity tags,” *Nature*, vol. 520, pp. 164–165, 2015.

[280] H. J. Lee, J.-H. Kim, H. K. Lim, E. C. Cho, N. Huh, C. Ko, J. C. Park, J.-W. Choi, and S. S. Lee, “Electrochemical cell lysis device for DNA extraction.,” *Lab Chip*, vol. 10, no. 5, pp. 626–633, Mar. 2010.

[281] B. D. Iverson and S. V. Garimella, “Recent advances in microscale pumping

technologies: A review and evaluation," *Microfluid. Nanofluidics*, vol. 5, no. 2, pp. 145–174, 2008.

[282] Y. Zhang, L. Su, D. Manuzzi, H. V. E. de los Monteros, W. Jia, D. Huo, C. Hou, and Y. Lei, "Ultrasensitive and selective non-enzymatic glucose detection using copper nanowires," *Biosens. Bioelectron.*, vol. 31, no. 1, pp. 426–432, 2012.

[283] S. Park, T. D. Chung, and H. C. Kim, "Nonenzymatic glucose detection using mesoporous platinum," *Anal. Chem.*, vol. 75, no. 13, pp. 3046–3049, 2003.

[284] H. Boo, S. Park, B. Ku, Y. Kim, J. H. Park, H. C. Kim, and T. D. Chung, "Ionic Strength-Controlled Virtual Area of Mesoporous Platinum Electrode," *J. Am. Chem. Soc.*, vol. 126, no. 14, pp. 4524–4525, 2004.

[285] Y. Li, Y. Y. Song, C. Yang, and X. H. Xia, "Hydrogen bubble dynamic template synthesis of porous gold for nonenzymatic electrochemical detection of glucose," *Electrochem. commun.*, vol. 9, pp. 981–988, 2007.

[286] L. Y. Chen, X. Y. Lang, T. Fujita, and M. W. Chen, "Nanoporous gold for enzyme-free electrochemical glucose sensors," *Scr. Mater.*, vol. 65, no. 1, pp. 17–20, 2011.

[287] Y. Xia, W. Huang, J. Zheng, Z. Niu, and Z. Li, "Nonenzymatic amperometric response of glucose on a nanoporous gold film electrode fabricated by a rapid and simple electrochemical method," *Biosens. Bioelectron.*, vol. 26, no. 8, pp. 3555–3561, 2011.

[288] K. B. Male, S. Hrapovic, Y. Liu, D. Wang, and J. H. T. Luong, "Electrochemical detection of carbohydrates using copper nanoparticles and carbon nanotubes," *Anal. Chim. Acta*, vol. 516, no. 1–2, pp. 35–41, 2004.

[289] S. Park, H. Boo, and T. D. Chung, "Electrochemical non-enzymatic glucose sensors," *Anal. Chim. Acta*, vol. 556, no. 1, pp. 46–57, 2006.

[290] T. G. Drummond, M. G. Hill, and J. K. Barton, "Electrochemical DNA sensors.," *Nat. Biotechnol.*, vol. 21, no. 10, pp. 1192–1199, Oct. 2003.

[291] M. A. Lapierre, M. O'Keefe, B. J. Taft, and S. O. Kelley, "Electrocatalytic Detection of Pathogenic DNA Sequences and Antibiotic Resistance Markers," *Anal. Chem.*, vol. 75, pp. 6327–6333, 2003.

## Appendix: Measured Current During Cell Lysis Experiments

| **Voltage (V)** | **Current (mA)** |
|---|---|
| 2 | 0.13±0.02 |
| 4 | 9.69±1.16 |
| 6 | 37.77±5.00 |
| 8 | 70.61±8.88 |
| 10 | 88.00±8.11 |

Appendix Table 1. 1 Measured current during voltage pulses with Electrodeposited cell lysis electrode devices.